CONTROLLED SELF-ASSEMBLY OF ITO NANOPARTICLES INTO AGGREGATE WIRE STRUCTURES IN PMMA-ITO NANOCOMPOSITES

A Dissertation
Presented to
The Academic Faculty

By

Charles J. Capozzi

In Partial Fulfillment
Of the Requirements for the Degree
Doctor of Philosophy in Materials Science and Engineering

Georgia Institute of Technology

May 2009

CONTROLLED SELF-ASSEMBLY OF ITO NANOPARTICLES INTO AGGREGATE WIRE STRUCTURES IN PMMA-ITO NANOCOMPOSITES

Approved by:

Dr. Rosario A. Gerhardt, Advisor
School of Materials Science and Engineering
Georgia Institute of Technology

Dr. Arun M. Gokhale
School of Materials Science and Engineering
Georgia Institute of Technology

Dr. Preet Singh
School of Materials Science and Engineering
Georgia Institute of Technology

Dr. Mohan Srinivasarao
School of Polymer, Textile and Fiber Engineering
Georgia Institute of Technology

Dr. Meisha Shofner
School of Materials Science and Engineering/Polymer, Textile and Fiber Engineering
Georgia Institute of Technology

Date Approved: March 31, 2009

ACKNOWLEDGEMENTS

I would like to express my appreciation to Dr. Rosario A. Gerhardt for her guidance and support during the course of my graduate studies. Dr. Gerhardt's invaluable input was equally matched by her compassion towards my goals, which undoubtedly lead me to thrive as a researcher and an individual. I would like to acknowledge the funding for this research from the Institute of Paper Science and Technology (IPST) at Georgia Tech and to the National Science Foundation (DMR-0642144). I am thankful to the committee members- Dr. Arun Gokhale, Dr. Preet Singh, Dr. Mohan Srinivasarao and Dr. Meisha Shofner for serving on my committee. I would like to acknowledge Zhi Li for the complex refractive index measurements of my specimens. Thanks to Dr. Ilia Ivanov at the Center for Nanophase Materials Sciences at Oak Ridge National Laboratory for access to his laboratory and taking photoluminescence measurements of my synthesized materials. I appreciate the assistance provided by Lex Nunnery and Dr. Tannenbaum's research group for frequent access to their equipment and general helpful discussion. I would like to thank Dr. Arun Gokhale for always making time to answer my questions related to the calculations and stereology contained in this work. Special thanks to Dr. V. Siva Kumar G. Kelekanjeri for obtaining the initial SEM images of my specimens in addition to his unconditional assistance in the lab. Thanks to Todd Walters for help and advice with the operation of the SEM. Thanks to Yolande Berta and Salil Joshi for taking TEM images of my composite fillers. Thanks to Dr. Yong Ding and Ben Weintraub for frequent access to their research group's spectrophotometer. Thanks to Richard Gilstrap for assistance with the materials synthesis. Thanks to Phil Graham and Dr. Jung-il Hong for advice with the operation of the XRD. Thanks to Ricky Whelchel for advice and

assistance with the analysis of the data obtained by USAXS measurements. Thanks to Dr. Albina Borisevich at Oak Ridge National Laboratory for taking STEM images of my synthesized materials.

I would like to express my appreciation for many past and present members of Professor Gerhardt's research group, for their assistance and friendship, and making work enjoyable to come to each day. I would like to acknowledge the late Dr. Jun John Xu and Dr. Gaurav Jain from Rutgers University, who provided me with the undergraduate research opportunities that initially propelled me towards my scholarly goals.

Finally, I am grateful to my mother, for her unconditional love and unwavering support throughout my time away from home.

TABLE OF CONTENTS

CHAPTER

LIST OF TABLES

LIST OF FIGURES

SUMMARY

In this research, polymer-matrix nanocomposites were fabricated with the objective of designing and characterizing materials that have unique phase-segregated microstructures. Indium tin oxide (ITO) nanoparticles were embedded in poly(methylmethacrylate) (PMMA) to form the nanocomposites which are the subject of this research. ITO is a degenerate semiconductor primarily used as a transparent conducting electrode in electronic devices. Since the ITO nanoparticles had an electrical conductivity several orders of magnitude higher than the PMMA, the PMMA-ITO nanocomposites could be characterized using non-destructive electrical measurements. In turn, correlations were made between the electrical properties and features in the microstructures of the nanocomposites.

Compression molding ITO-coated PMMA particles at ~157°C resulted in a transition in the morphology of the PMMA particles from spherical to polyhedral shapes in the specimens. Consequentially, the microstructure of the PMMA-ITO nanocomposites resembled a Voronoi arrangement. It was also observed under these conditions that the ITO nanoparticles on the surfaces of the PMMA particles experienced significant displacement during compression molding, as a function of their concentration. When the ITO concentration was near or below the percolation threshold for the PMMA-ITO nanocomposites, the ITO nanoparticles accumulated along the edges of the polyhedral-shaped PMMA particles and self-assembled into aggregate structures resembling nano- or microwires. These aggregate wire structures were responsible for 3-dimensional percolation in the PMMA-ITO nanocomposites, which occurred between 0.33-0.50 vol.% ITO. The ITO nanoparticles began to form conducting sheets across the flat faces of the polyhedral PMMA particles only after the percolation threshold concentration was exceeded.

The specimens with controlled microstructures were investigated using ac impedance spectroscopy, transmission optical and scanning electron microscopy (SEM), UV-Vis-IR transmission spectroscopy, internal reflection intensity analysis (IRIA), ultra-small angle x-ray scattering (USAXS), and stereological measurements. A geometrical model based on the volume-to-surface area ratios of the PMMA and ITO particles was also derived in order to predict the percolation threshold in the specimens. The model accounted for the polyhedral morphology of the PMMA particles in the microstructure. USAXS and stereological measurements were also used to characterize the dimensions of the self-assembled ITO aggregates in order calculate the amount of ITO nanoparticles that would be expected for percolation to occur in the PMMA-ITO nanocomposites. The experimental-based calculations showed reasonable agreement with the percolation threshold values detected by electrical measurements of the specimens.

CHAPTER 1

INTRODUCTION

Polymer-matrix composites (PMCs) are an important class of materials that are useful for various applications. Depending on the type of polymer matrix and filler materials used, the advantages of PMCs typically include good mechanical properties, semi-conducting electrical properties, and ease of production in terms of cost and processing. These properties are also highly dependent on the microstructure of the composites. For example, PMCs may be rendered electrically conducting only if the microstructure permits percolation of the filler through the matrix and the filler possesses good electrical conductivity.

The microstructures of PMCs may vary depending on the fabrication conditions used. As an example, when PMCs are formed using injection molding or extrusion processes, this tends to promote high degrees of dispersion of the filler in the matrix. In the case of PMCs that have a matrix composed of two immiscible polymers, the filler may be confined to the more viscous of the two polymer phases, which limits the distribution of the filler in the composite. It is therefore important to consider the fabrication method and microstructure of PMCs when attempting to establish correlations to other properties.

Conventional microscopy techniques are indispensable in acquiring detailed structure-property information. However, sometimes these methods of microstructural characterization can be destructive and time-consuming. Non-destructive evaluation (NDE) techniques provide an alternative approach to microscopy in the characterization of materials. NDE techniques can be useful in determining the local concentration of different phases in a given microstructure. Therefore, it is desirable to correlate information obtained by NDE techniques to microscopy data in order to obtain a comprehensive understanding of the structure of a material system. Once correlations between the NDE parameter(s) and the microstructure are developed, the NDE techniques may then be used for routine analysis in predicting the behavior of a given material.

It is known that the electrical properties of PMCs are sensitive to the local concentration of the filler in the matrix, which is often difficult to predict because of the random arrangement of the filler distribution. For PMCs having phase-segregated microstructures, better prediction of the properties is possible since enhanced control over the distribution of the filler in the matrix can be achieved. In this research, PMMA-ITO nanocomposites were chosen as the composite system in which to explore alternative microstructures, specifically highly phase-segregated microstructures. The microstructures were primarily controlled by varying the ITO particle size and concentration, and the fabrication parameters used to form the nanocomposites. The motivation for this research was to develop correlations between the microstructure and non-destructive measurements in order to improve the predictability of properties in percolating PMCs. As a result of this work, a novel phase-segregated microstructure was discovered where ITO aggregate-wire structures self-assembled during the composite forming process, and a model was proposed to predict percolation in these types of nanocomposites.

A detailed description of the processing parameters is given in section 3.2. Structural analysis of the specimens was conducted primarily using transmission optical microscopy and scanning electron microscopy (SEM). Impedance spectroscopy and optical spectroscopy were the primary NDE characterization tools used for analyzing the variations among the specimens. The results of the characterization are described in detail in Chapter 4. In addition, ultra-small angle x-ray scattering (USAXS) and stereological techniques were also used to describe the dimensions of the ITO aggregate-wire structures that self-assembled in the PMMA-ITO nanocomposites. These results were compared with a theoretical geometrical model (Chapter 5) that was used to attempt to predict the percolation behavior of the ITO nanoparticles in these types of nanocomposites.

CHAPTER 2

LITERATURE SURVEY

2.1 Microstructures in Polymer-matrix Composites

The filler in polymer-matrix composites may be “organized” in many different ways. These arrangements may be classified as two different types of microstructures: (i) random, (ii) or phase-segregated. Polymer matrix composites, as films or bulk materials, conventionally possess microstructures where the filler is randomly dispersed throughout the matrix. However, phase-segregation between the filler and matrix in polymer-matrix composites can be achieved by utilizing the molecular structure properties,[1, 2] the thermodynamic properties,[3, 4] or the physical properties (i.e., viscosity) of the polymer matrix.[5-23] The main advantage of phase-segregation in polymer-matrix composites is that percolation of the filler can be attained in the matrix with less than 0.01 vol.% filler.[16, 24] An overview of the different microstructures reported for polymer-matrix composites will be described in Section 2.1.1.

2.1.1 Polymer-matrix Composites with Random Microstructures

For polymer-matrix composites with random microstructures, the goal is for the filler to be uniformly dispersed across the entire matrix. Random microstructures are usually developed by distributing the filler in the polymer when it exists as a melt or dissolved-solution state. Figure 2.1 illustrates a poly(α-methylstyrene)-gold nanocomposite possessing a conventional microstructure, where the gold particles (dark in the TEM image) are randomly spread across the polymer matrix.[25]

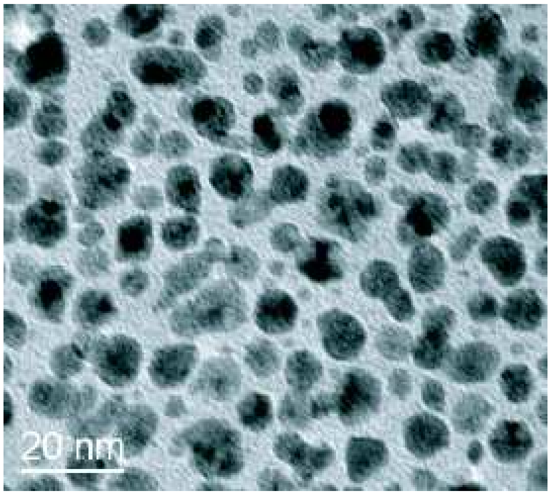

Figure 2.1. TEM image of a poly(α-methylstyrene)/gold nanocomposite with a conventional random microstructure.[25]

Achieving uniform or random dispersion can be heavily dependent on the mixing method. For making bulk composites, extrusion or injection molding is often employed for distributing the filler when the polymer is in the melted state. When the filler is added via dissolution of the polymer, bulk composites are typically formed by casting the suspension into a mold, grinding the dried films, and compression molding the filled polymer powders.[5, 24, 26]

Adding the filler to the polymer in the melted state, referred to as melt mixing, is often desirable because the process is free of solvents and contaminants.[27] Thermoplastic polymers are preferable in melt mixing because they do not undergo changes in their chemical properties during heating and cooling. Uniformly distributing the filler is also highly dependent upon the rheological properties of the polymer. High-shear mixing for long times is favorable in enhancing the dispersion of the filler and overcoming the high viscosities of filled polymer-melts. Anisotropic fillers further raise the viscosity due to their higher aspect ratio, which has a lower packing fraction and larger effective hydrodynamic volume.[28, 29]

Percolation is the term used to describe when the filler forms a continuous network through the matrix. Figure 2.2 illustrates percolation in a two-phase system where the dark particles represent the filler phase. The amount of filler necessary for percolation of the filler in the matrix is generally high due to the random filler distribution in the composite. It has been shown that three-dimensional percolation in an amorphous polymer matrix can require up to 33% volume fraction of monosize filler particles.[30, 31] However, the percolation threshold can be reduced if the surface area of the fillers is increased, or anisotropic fillers are used.[32, 33]

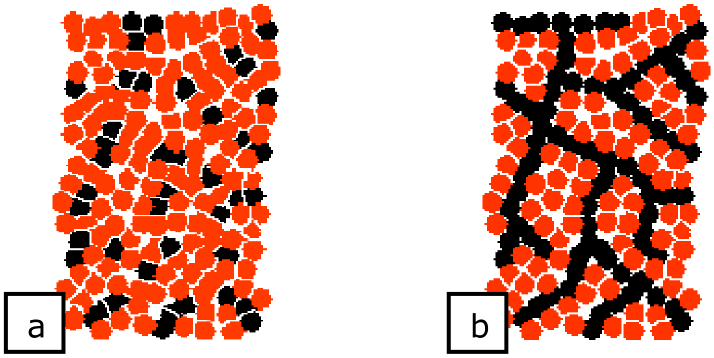

Figure 2.2. Schematic of the development of percolation in a two-phase composite by increasing the amount of filler: (a) low content; (b) high content.[15]

Figure 2.3 shows the electrical resistivity of PMMA nanocomposites filled with carbon black (CB) that have random microstructures and phase-segregated microstructures.[5] When the filler is electrically conducting, the electrical resistivity of the composite can be decreased by several orders of magnitude due to percolation of the filler. Figure 2.3 also demonstrates that higher filler concentrations are necessary to achieve percolation in the nanocomposites that contain random microstructures compared to the nanocomposites that have phase-segregated microstructures.

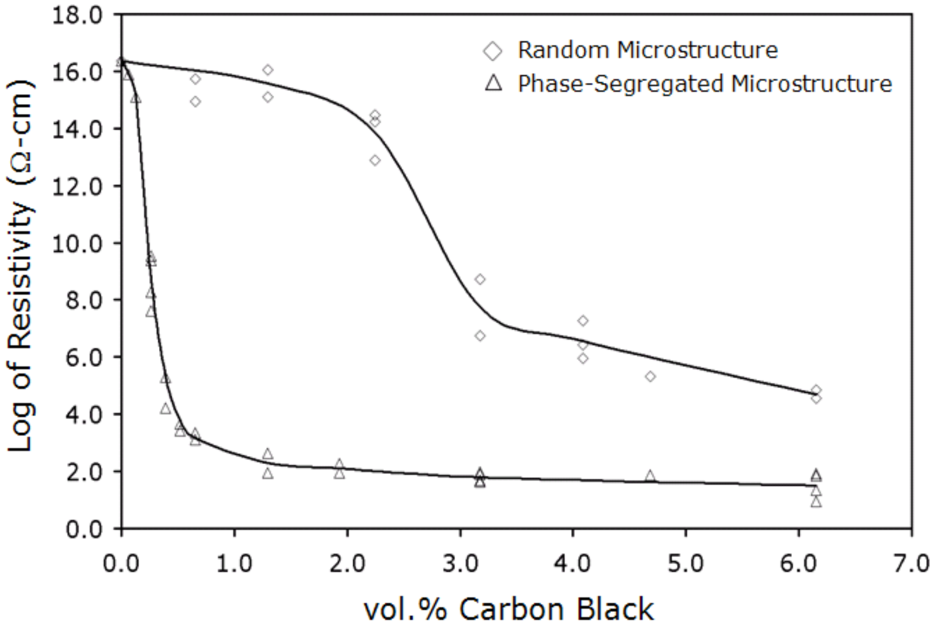

Figure 2.3. Electrical resistivity of PMMA-CB composites as a function of CB content that have different microstructures. (modified).[5]

2.1.2. Polymer-matrix Composites with Phase-Segregated Microstructures

The degree of crystallinity of the polymer matrix can be used to control the distribution of the filler in the composite. The filler is forced into the amorphous regions of the polymer matrix upon the formation of crystalline regions. As a result of the segregation that occurs between the filler and the crystallites, the percolation threshold is reduced in the polymer matrix.[2] Figure 2.4 illustrates the effect of crystallites on the distribution of the filler in the polymer matrix, where the filler is represented by the dark circles.

Several factors contribute to the degree of crystallinity in the polymer matrix. Crystallization may be hindered by atactic configuration, bulky side groups, and chain branch properties since they make packing of the polymer chains more difficult in the molecular structure.[34] Cross-linking and high molecular weight also cause similar issues with regard to polymer crystallization. Slow cooling rates may be employed to overcome these obstacles and promote more crystallinity in the polymer matrix.

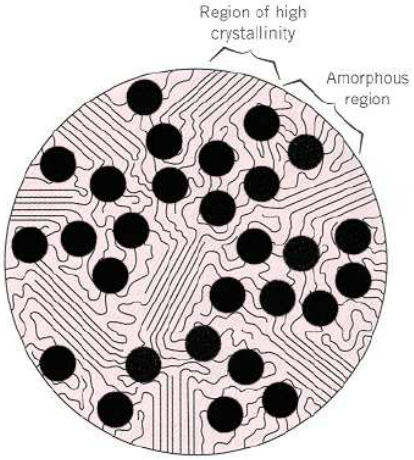

Figure 2.4. Schematic of the distribution of the filler (dark circles) in a semi-crystalline polymer when the crystallites force the filler into the amorphous zones of the matrix (Modified).[35]

Figure 2.5 shows the effect of the polymer crystallinity on the percolation threshold and electrical conductivity in polymer-matrix composites. Figure 2.5a displays that the percolation threshold is reduced in polyethylene (PE)-carbon black composites when the degree of crystallinity is enhanced in the polyethylene matrix.[2] Figure 2.5b shows the effect of slower cooling on the electrical resistivity of polyvinylidene fluoride (PVDF)-carbon black composites after hot compression molding.[1] The data indicates that the slower cooling rate results in lower resistivity of the composites due to the higher crystallinity of the PVDF matrix.

Using a polymer matrix composed of two thermodynamically incompatible polymers may also be used to increase segregation between the matrix and the filler phases.[3, 4] By adding an unfilled immiscible polymer to the matrix, the volume occupied by the filled polymer in the composite is smaller, which raises the density of the conducting particles in the filled polymer. For this case, the filler is first dispersed in one of the polymers usually via melt mixing. Subsequently, the unfilled immiscible polymer is added to the melt suspension. In order to prevent the filler from migrating into the unfilled polymer during mixing, it is important for the unfilled polymer to have a higher viscosity than the filled polymer.[36]

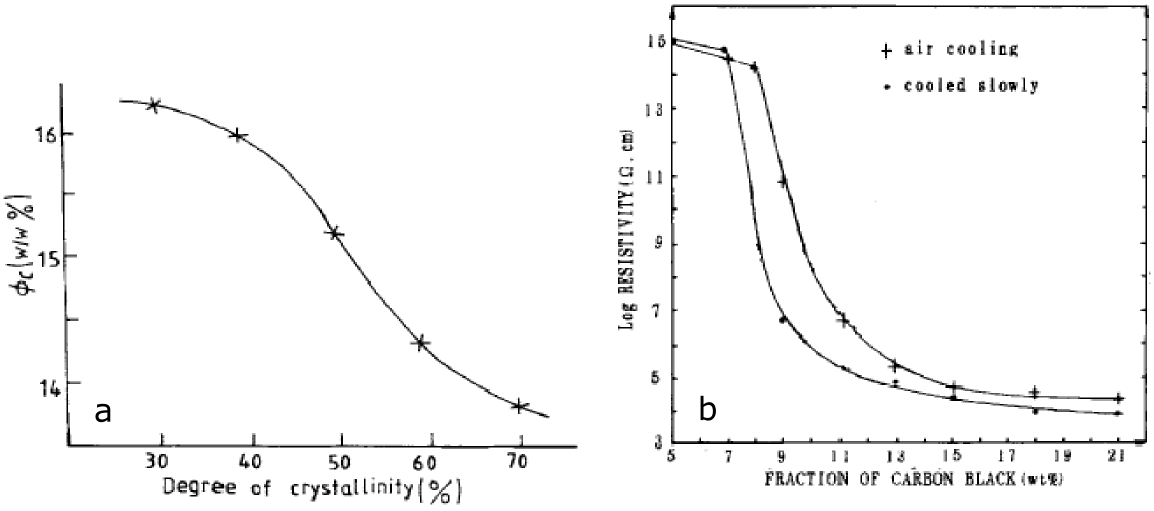

Figure 2.5. Effect of crystallinity on the percolation threshold and electrical conductivity of polymer-matrix composites. (a) Effect of higher crystallinity in polyethylene on the percolation threshold in polyethylene/carbon black composites;[2] (b) Effect of cooling rate on the electrical resistivity of carbon black/PVDF composites (Modified).[1]

The filler may also be localized at the interfaces between the immiscible polymer blends if there is low wettability by the filler on both of the polymers. For these conditions, it is preferable to melt mix the two unfilled immiscible polymers prior to adding the filler. Figure 2.6a shows the distribution of the filler in a polyethylene-polystyrene (PS)-carbon black composite;[3] and Figure 2.6b illustrates the resultant microstructure of a polystyrene-polymethylmethacrylate-carbon black composite formed after the addition of carbon black to a melt-blend of unfilled PS and polymethylmethacrylate (PMMA).[4] It has been demonstrated, however, that the filler tends to penetrate the less viscous polymer when the interface between the two polymers becomes over-saturated.[3]

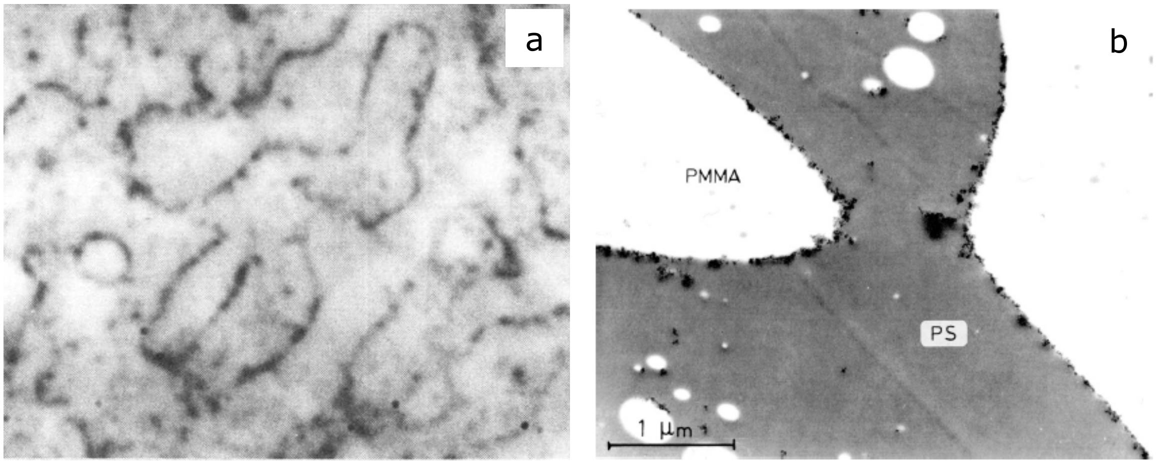

Figure 2.6. (a) Optical micrograph of a 45/55 PE/PS blend filled with 1 wt.% carbon black;[4] (b) TEM micrograph of a 50/50 PS/PMMA composite filled with 2 wt.% carbon black.[3]

The phase-segregated microstructures that offer the most segregation between the filler and matrix phases were originally referred to as “segregated network microstructures” by Turner.[6] These microstructures are typically formed by hot pressing or compression molding polymer particles coated with smaller ceramic or metallic particles. The stages in the forming process are similar to compression molding neat polymer powders: (1) particle rearrangement, (2) elastic deformation at contact points, (3) plastic deformation at contact points or coalescence.[37] However, when the polymer powders are coated with the ceramic or metallic particles, the coalescence stage is impeded and homogenization of the polymer matrix is prevented.[38] This can result in confinement of the ceramic or metallic particles around the polymer particles and a high degree of segregation between the two phases.[5-23]

Turner and co-workers were the first to report polymer-matrix composites with segregated network microstructures in the 1970s.[6-8] They proposed that the position of the filler remained unchanged once it was deposited onto the surface of the polymer particles due to their viscosity. As a result, a segregated network of the filler across the surfaces of the polymer particles was preserved throughout the matrix after the composite was formed. Figure 2.7 illustrates the concept behind segregated network microstructures as described by Turner and co-workers.

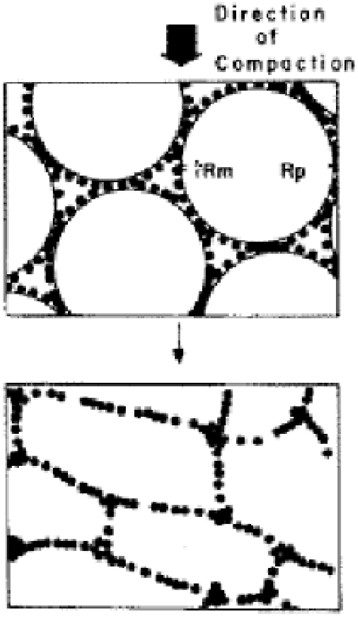

Figure 2.7**.** The concept of a segregated network microstructure. Schematic of polymeric powders compacted around filler to form segregated networks of the filler particles.[6]

Figure 2.8 displays the resultant distribution of the filler in two different polymer-matrix composites having segregated network microstructures. Figure 2.8a shows a photomicrograph of a polyvinylchloride (PVC) matrix filled with 7 vol.% Ni;[6] and Figure 2.8b presents an optical micrograph of an UHMWPE-carbon black composite.[12]

An advantage of the segregated network microstructure over the immiscible polymer blends is that filler penetration of the polymer phase is more easily controlled by the hot pressing parameters (temperature, pressure, etc.). Therefore, segregation can be preserved more readily and there is a higher percolation probability of the filler in the matrix.

Despite their advantages, phase-segregated microstructures in polymer-matrix composites have been the subject of relatively few studies since the reports submitted by Turner and co-workers in the 1970s. Table 2.1 summarizes some of the composite systems that have been investigated and the processing parameters that were used in making the composites.[6-13]

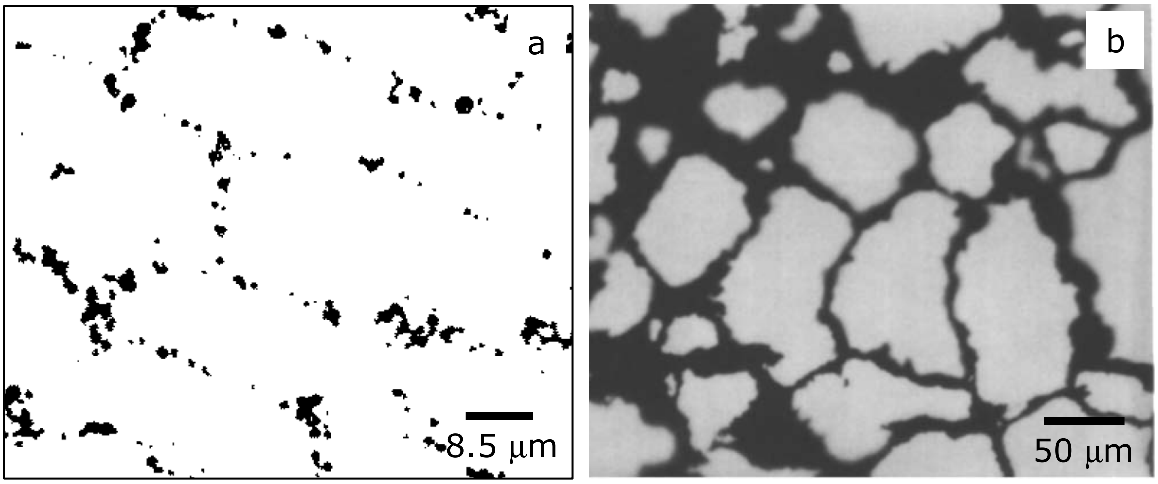

Figure 2.8. (a) Photomicrograph of PVC filled with 7 vol.% nickel. (modified);[6] (b) Optical micrograph of UHMWPE filled with 6 wt.% carbon black.[12]

Several important processing parameters as they relate to segregated network microstructures have received little attention. With regard to mixing, mechanical blending has been the primary method used to deposit the filler onto the polymer particle surface, with the exceptions of Hochberg and Grunlan *et al.* who coated the polymer powders using film deposition techniques.[39, 40] Other than results reported by Bouchet *et* *al.,*[13] the class of filler materials used has been limited to metals or carbon. Virtually no temperature or pressure-controlled experiments have been implemented to study their effect on the percolation threshold of any composite system with a segregated network microstructure. Similarly, the role of the specimen thickness on the properties of the microstructure has been also ignored. The influence of the particle size ratio between the filler and the polymer appears to be the only fabrication parameter to have been extensively investigated.[6, 12, 13]

Table 2.1. Fabrication conditions for polymer-matrix composites reported in the literature with segregated network microstructures.

Ref.	Matrix/Filler Composite	Time	Temperature	Compaction Pressure
[6]	High-density Polyethylene/Ni	-	20°C	1000 kg/cm^2 (98.1 MPa)
[7]	Polyurethane elastomer/Ni	30 min.	120°C	4200 psi (29 MPa)
[8]	Polyvinylchloride/Ni	10 min.	120-130°C	700 kg/cm^2 (68.6 MPa)
[9]	Polymethylmethacrylate/Cu	10 min.	145°C	100 kg/cm^2 (9.81 MPa)
[10]	Polyvinylchloride/Cu	-	130-140°C	44 MN/m^2 (44 MPa)
[11]	Urea-formaldehyde embedded cellulose/Zn	30 min.	150°C	20 MPa
[12]	Ultra-high molecular weight polyethylene /Carbon	-	170-210°C	13.8-44.2 MPa
[13]	Ultra-high molecular weight polyethylene/TiN	15-60 min.	140-180°C	5-20 MPa

2.1.3 Models Predicting Percolation in "Segregated Network Microstructures"

The limited number of models developed to explain percolation in segregated network microstructures also reflects the lack of diverse studies on polymer-matrix composites with phase-segregated microstructures.[6, 10, 14, 19] Turner, however, did develop a model based on the concept he proposed for percolation in segregated network microstructures.[6] It was assumed that a monolayer of filler on the surface of the polymer particles was required to form an infinite cluster of filler particles at volume fraction, V_A, while a double layer was necessary to cover the entire polymer particle surface. Equation 1 presents the expression derived by Turner:

$$V_A = \frac{50P_c}{1+\left(\frac{\phi}{4}\right)\left(\frac{R_p}{Rf}\right)} \tag{1}$$

where ϕ is defined as the factor that is dependent on the shape formed by the particles of filler aggregated on the surface of the polymer powder, P_c represents the initial probability for a first nonzero probability of an infinite cluster (as a function of ϕ), and R_p and R_f are the radii of the polymer and filler particles, respectively, assuming $R_p >> R_f$.[6] Figure 2.9 gives a good description of some of the possible shapes that the aggregates can form, where ϕ_Δ represents a triangular aggregate and $\phi_\Box$ represents a square aggregate: [14]

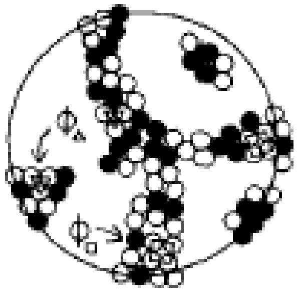

Figure 2.9. Schematic of triangular- and square-shaped aggregates that the conducting filler may form on the surface of the polymer powders in segregated network microstructures.[14]

However, comparison between Turner’s experimental and calculated results indicated that the experimental percolation threshold was two to three times larger than the calculated V_A when the size ratio between the matrix and filler particles was less than 16.

Figure 2.10 shows the comparison of Turner’s experimental data with theoretical data for nickel/high-density polyethylene composites for R_p/R_m ratios $\geq$ 7.5, where R_p is the radius of the polymer particles, and R_m is the radius of the nickel particles.[6] This discrepancy was attributed to many of the conducting filler particles not contributing to the electrical conductivity of the composite.[6, 19]

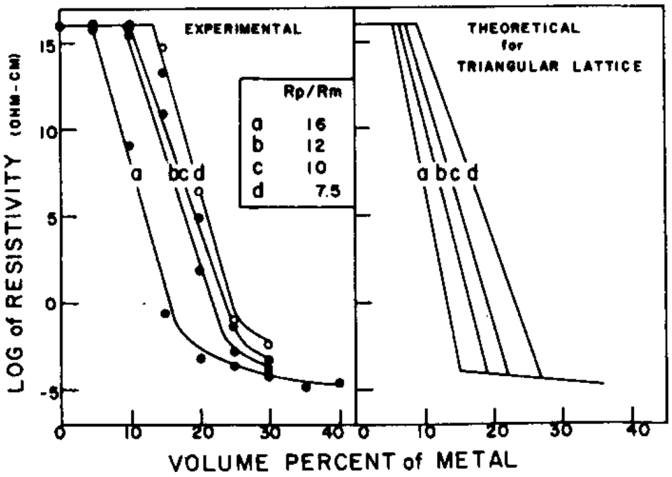

Figure 2.10. Comparison of experimental data with theoretical data for nickel/high-density polyethylene composites for R_p/R_m ratios $\geq$ 7.5, where R_m is the radius of the nickel particles.[6]

Kusy modified Turner’s model by proposing that single and double surface layers on the polymer particles do not form since the filler has a propensity to accumulate in the interstitial spaces at all concentrations during compaction.[14] Kusy presented the expression shown in Equation 2:

$$V_A = \frac{100}{1 + 0.5\left(\frac{\phi}{x_c}\right)\left(\frac{R_p}{R_f}\right)} \tag{2}$$

where the new parameter x_c represents the critical fraction of the polymer particle surface covered by the filler.[14] The equation showed fair agreement with most of the experimental data presented in his work.[14]

Another model describing metal-filled polymer composites with a segregated network microstructure was developed by De and co-workers.[10, 19] Figure 2.11 shows that the authors derived the model assuming that the polymer particles deformed into cubic shapes under pressure. The model also proposed that the metallic filler particles were in a square lattice arrangement around the surface of the polymer particles.

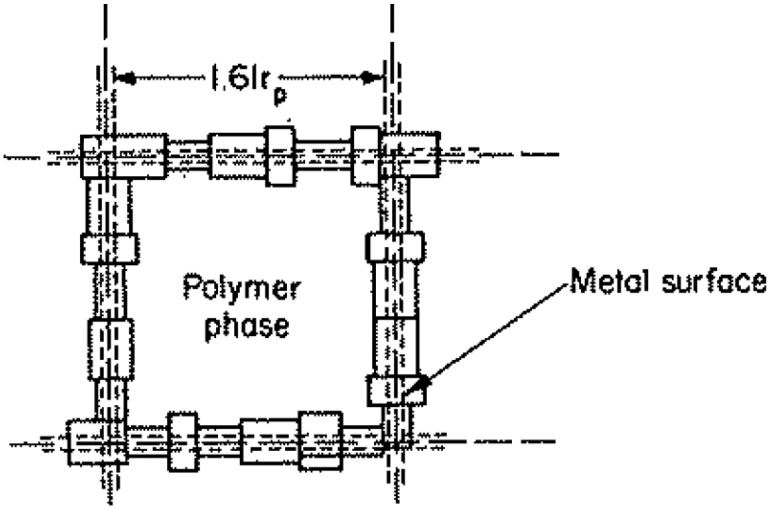

Figure 2.11. The model proposed to describe a polymer/metal composite having the metal particles arranged in a square lattice around the polymer phase (modified).[10]

By considering the volume to surface area ratios of the filler and matrix particles, De derived the expression shown in Equation 3, where V_A is defined as it was in Equations 1 and 2.[19] De's model yielded the best agreement with the experimental data reported in previous studies about polymer-matrix composites with segregated network microstructures.[19]

$$\frac{2V_A}{100-2V_A} = 2.99\left(\frac{R_p}{R_f}\right) \tag{3}$$

2.2. Polymethylmethacrylate (PMMA) and Indium Tin Oxide (ITO)

Polymethylmethacrylate (PMMA) and indium tin oxide (ITO) were chosen as the matrix and filler materials, respectively, for this study. PMMA is a common replacement for glass due to its high transparency, easy processing, and low cost. ITO is known as a premier electrode material due to its ability to be simultaneously transparent and conducting as a thin film. The following subsections describe some studies on the physical properties (i.e., glass transition temperature, viscosity) of PMMA that are related to its processing. Information about the properties and applications of ITO is also provided.

2.2.1. Polymethylmethacrylate (PMMA)

PMMA is a common matrix material used in polymer-matrix composites.[9, 15, 17, 18, 21, 22] The glass transition temperature and coarsening mechanisms of PMMA play an important role in the processing of the PMMA for polymer-based composites. It is a well-known amorphous material with a glass transition temperature in the range of 100-120°C.[41] The molecular structure of PMMA is shown in Figure 2.12.

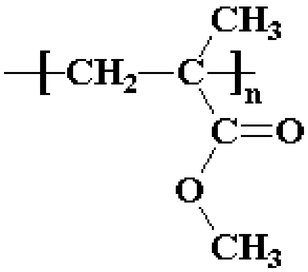

Figure 2.12. Molecular structure of PMMA.

Although the glass transition for amorphous polymers might be confused with a thermodynamic second-order phase transformation (Fig. 2.13), it is not considered a second-order phase transformation since it does not follow the equation developed by Ehrenfest for a true second-order transition:

$$\frac{dT_g}{dp} = \frac{T_g V(T_g)\Delta\alpha}{\Delta C_p} = \frac{\Delta\kappa}{\Delta\alpha} \qquad (4)$$

where T_g is the glass transition temperature, p is the pressure, $V(T_g)$ is the molar volume at T_g, $\Delta\alpha$ is the thermal expansion coefficient difference (rubber to glass) at T_g, ΔC_p is the molar heat capacity difference, and $\Delta\kappa$ is the compressibility difference.[41, 42]

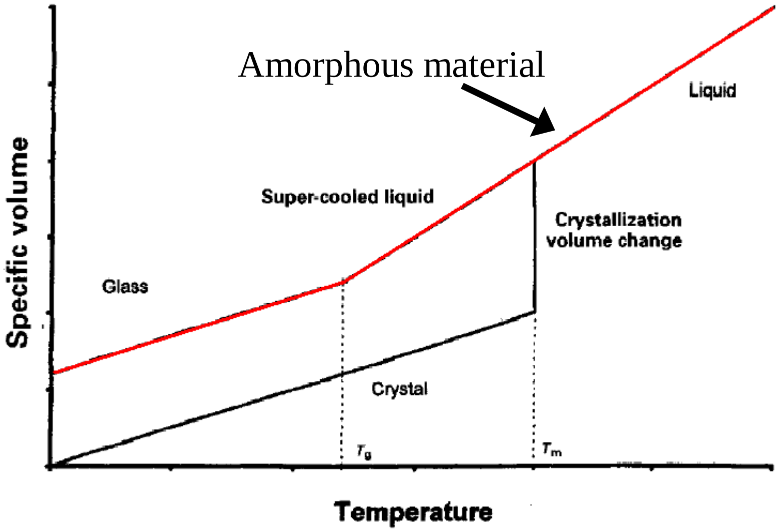

Figure 2.13. Specific volume versus temperature for an amorphous material.[41]

An early study by Saito *et al.* specifically showed that the glass transition for PMMA was rate-dependent.[43] Figure 2.14 shows the dielectric dispersion of PMMA as a function of temperature. The dielectric dispersion (Fig. 2.14a) was calculated by taking

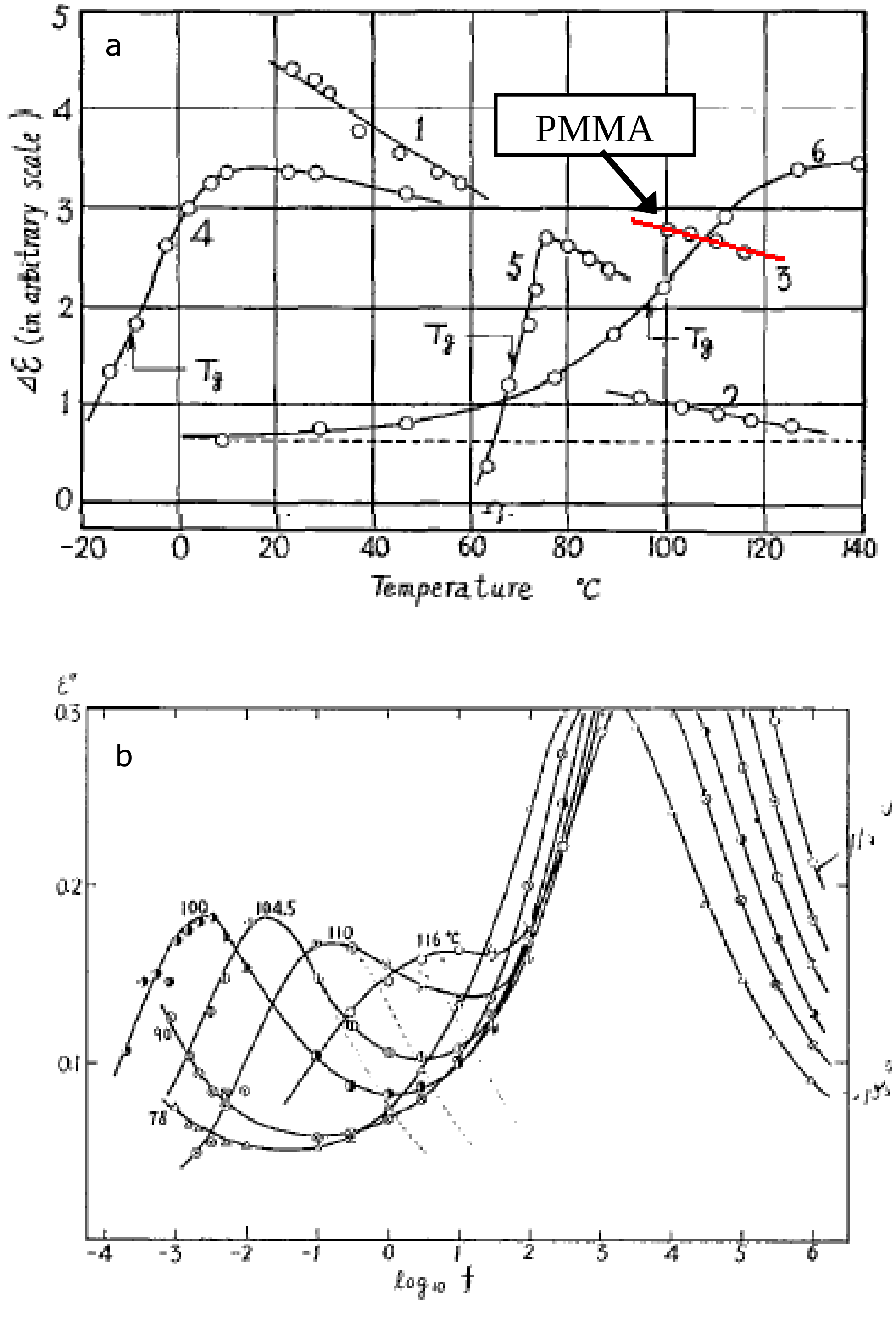

Figure 2.14. (a) Dielectric loss of PMMA; and (b) Dielectric dispersion for various polymers as a function of temperature (Modified).[43]

the area under the curves for the dielectric loss versus the log of frequency in the low frequency region (Fig. 2.14b). The dielectric loss at the higher frequencies was ignored since it was attributed to the motion of side chains, which is not relevant to the glass transition temperature. This conclusion was based on the relationship between the dielectric dispersion and temperature described by Equation 5:

$$\varepsilon_0 - \varepsilon_\infty = [3\varepsilon_0 / (2\varepsilon_0 + \varepsilon_\infty)][(\varepsilon_\infty + 2) / 3]^2 \times \left(\frac{4\pi n g \mu^2}{3kT}\right) \qquad (5)$$

where $\varepsilon_0 - \varepsilon_\infty$ is the dielectric dispersion, n is the concentration of dipoles, μ is the dipole moment, g is a parameter relating to dipole-dipole interactions, k is the Boltzmann constant, and T is the absolute temperature.[43] The experimental data for PMMA (Fig. 2.14b) indicated that the term ($ng\mu^2$) was nearly independent of temperature, which suggested that no considerable molecular arrangement occurred and a relaxation process governed the glass transition in PMMA. Similar conclusions have been drawn for other amorphous polymers.[44]

An important study by Kuczynski *et al.* described the flow properties of PMMA particles.[45] The experiment was conducted by sintering PMMA spherical grains to a flat block of PMMA and measuring the neck diameter. The neck radius was measured as a function of time in the temperature range 127-207°C (Fig. 2.14). Assuming that the Ostwald power law, $\sigma = K(\acute{\varepsilon}_s)^n$ (where n is the flow behavior index, σ is the shear stress, K is the consistency index, and $\acute{\varepsilon}_s$ is the shear strain rate), could describe the polymer flow; an empirical equation was derived to describe the relationship between the neck diameter and time (Eq. 6):

$$\left(\frac{x^2}{a^{1.02}}\right)^p = \mathrm{F(T)}t \tag{6}$$

where x is the neck radius, a is the particle radius, F(T) is a function of only temperature, t is the time, and p is the inverse of the flow behavior index.[45] The flow behavior index was determined by the slope of x^2/a versus log t (Fig. 2.15).[45]

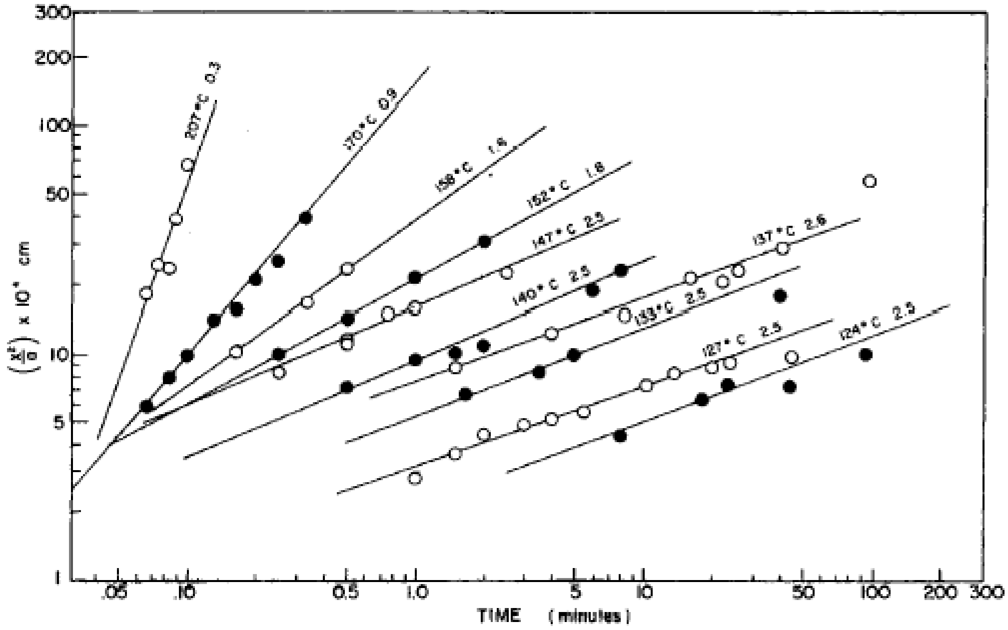

Figure 2.15. Variation of the ratio x^2/a with time for spheres of poly(methylmethacrylate) sintered at indicated temperatures.[45] (x – neck radius, a – particle size radius)

Based on the Ostwald power law and the experimentally determined flow index behavior, Kuczynski proposed that the behavior of PMMA was non-Newtonian and exhibited pseudo-plastic (shear-thinning) flow up to 170°C, and dilatant (shear-thickening) flow at higher temperatures.[45, 46]

The model used by Kuczynski neglects applied stress, which means that it is imperfect for describing the coarsening that occurs between PMMA particles during hot pressing. However, the temperature selected for the experimental procedure used to form the PMMA-ITO nanocomposites in this research is appropriate based on the literature and the desired viscoelastic behavior for the PMMA matrix particles.

2.2.2. Indium Tin Oxide (ITO)

Optically transparent and electrically conducting oxides were first discovered by Badeker in 1907.[47] Materials that are both transparent and conducting are rare since conducting materials have a tendency to absorb wavelengths in the visible light region. Figure 2.16 shows the typical index of absorption for conducting materials.

During World War II, transparent conducting materials became critical to bombing missions, as they were developed for defrosting windows in airplanes at high-altitudes.[48] In the 1960s, indium tin oxide (ITO) was discovered to be a transparent conducting oxide when deposited as a thin film.[49] Since then, ITO has become one of the most commonly used transparent conducting oxides in applications ranging from flat-panel display electrodes to electromagnetic shielding.

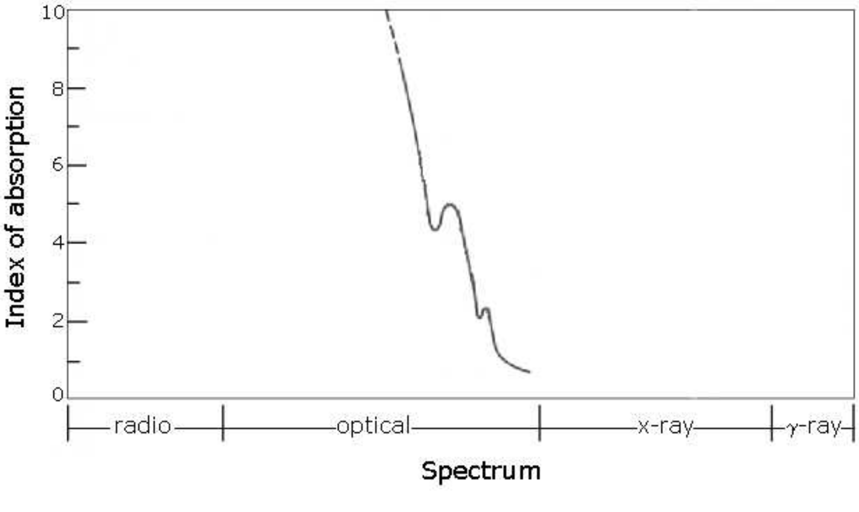

Figure 2.16. Typical index of absorption for conducting materials in various spectra (modified).[50]

Indium oxide has a cubic bixbyite crystal structure and electrical resistivities as low as ~10^{-3} Ω-cm have been reported for this material.[51] Tin doping of indium oxide has been shown to decrease the resistivity to as low as ~10^{-4} Ω-cm by increasing the carrier concentration in the material.[47, 51-53]

Equation 7 shows that the electrical conductivity is proportional to the carrier concentration, where σ is the conductivity, N_e is the number of mobile electrons per unit volume, q_e is the charge per electron, and μ_e is the electron mobility in the material.[34]

$$\sigma = N_e q_e \mu_e \tag{7}$$

ITO is classified as a degenerate semi-conducting material.[51] This means that the states at the bottom of the conduction band are filled and the Fermi level is in the conduction band. This results in metal-like conductivity in the material. Consequently, the energy required to excite an electron from the valence band into the conduction band optically becomes greater than the inherent band gap of the material. This is known as the Burstein-Moss effect, where the increase in energy required for a transition in a degenerate semiconductor, ΔE_g, becomes:

$$\Delta E_g = \frac{h^2 k_F^2}{2m_{cv}} \tag{8}$$

where h is Planck's constant, k_F is the Fermi wave vector (which is a function of carrier concentration), and m_{cv} is the reduced effective mass (which is a function of the conduction and valence band density-of-states effective masses).[54] Due to the Burstein-Moss effect, the material does not respond to wavelengths in the visible light region (400-700 nm) and high transmittance remains possible. Figure 2.17 shows a schematic of the band structure in the material.

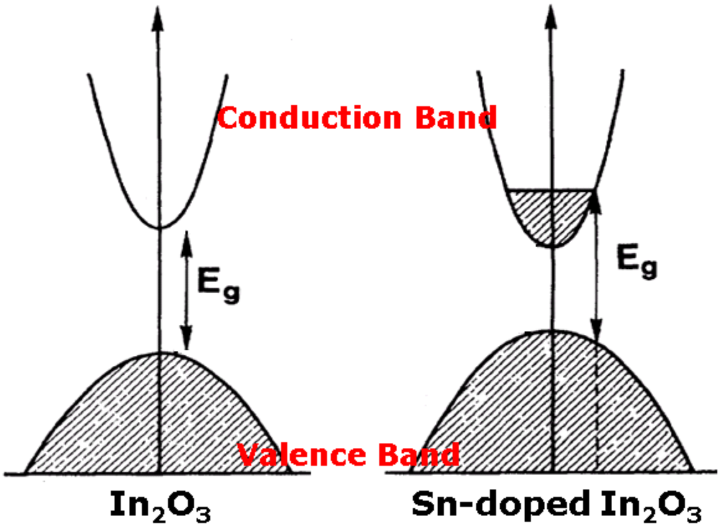

Figure 2.17. Schematic of band structure before (left) and after (right) doping indium oxide with tin (modified).[55]

ITO films were initially deposited using reactive dc sputtering of In-Sn metallic targets in an oxygen atmosphere. However, ITO films are currently deposited using dc sputtering with a ceramic ITO target in an oxygen/argon environment after it was found that In-Sn metallic targets suffered from poisoning effects.[47] Although dc magnetron sputtering is favorable for high deposition rates, this technique results in poor target utilization and costly down time. Wet surface grinding is often used to prepare the ITO targets used in sputtering. Within the past decade, there have been reports of potential health hazards as a result of wet surface grinding of indium tin oxide.[56, 57]

The deposition environment plays an important role in the resultant properties of ITO. This is because generated oxygen vacancies may contribute free electrons to the conduction band. Notably, excess defect concentrations can impede the electron mobility in ITO, which in turn can reduce the electrical conductivity (Eq. 7).[58] Figure 2.18 shows the effect of oxygen concentration on the optical transmittance and electrical resistivity of sputtered ITO films.

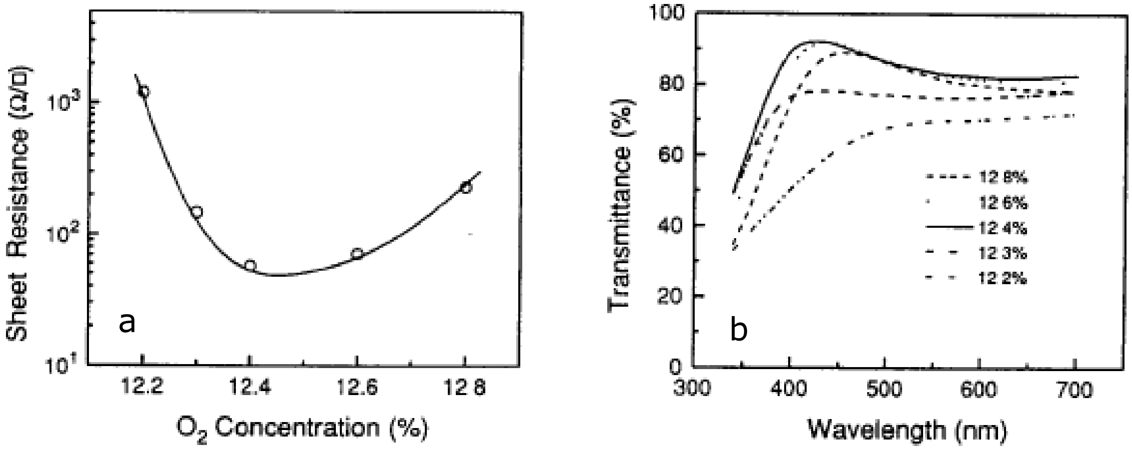

Figure 2.18. O_2 concentration given as the $[O_2]/([Ar] + [O_2])$ percentage vs. (a) sheet resistance and (b) transmittance of visible light for as-deposited ITO. The thickness of the films is 1150 Å.[59]

In order to address the efficiency issues related to the poor ITO target utilization during sputtering, hydrothermal methods,[60] sol-gel routes,[61-65] and colloidal chemistry processes[66-70] have been explored to synthesize ITO nanoparticles. It is believed that by depositing and sintering ITO nanoparticles on substrates, this would increase the efficiency of utilized ITO and allow coatings onto complex-shaped surfaces.[71] Many of the ITO nanoparticle synthesis methods have been shown to yield indium tin oxides having various compositions, degrees of crystallinity, particle morphologies, etc. Consequently, each of these techniques yields materials with different electrical and optical properties. Figure 2.19 shows an example of different types of ITO nanoparticles produced by hydrothermal[60] and colloidal chemistry methods.[68]

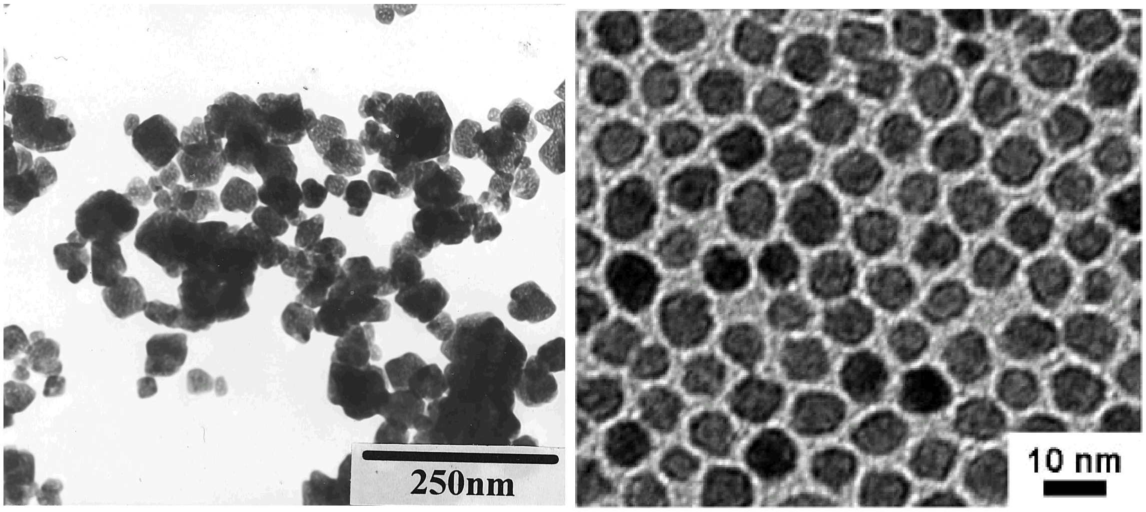

Figure 2.19. TEM images of (a) hydrothermally derived ITO nanoparticles;[60] and (b) ITO nanoparticles synthesized by a colloidal chemistry route.[68]

In addition to thin film applications, there have also been a few attempts to use ITO nanoparticles as fillers in transparent polymer-matrices.[15, 17, 21, 22, 72-74] Miyazaki *et al.*[73] embedded ITO nanoparticles in urethane in order to modify the types of wavelengths transmitted through the polymer. Carotenuto *et al.*[72] reported electrical and optical properties for ITO nanoparticles incorporated into a poly(vinyl pyrrolidone) (PVP) matrix (shown in Figure 2.20). However, due to high percolation thresholds and scattering effects, useful electrical conductivity and optical transmittance have not been achieved simultaneously for ITO-filled polymer matrix nanocomposites thus far.

Figure 2.20. Image demonstrating the transparency of an ITO-PVP nanocomposite film.[72]

CHAPTER 3

EXPERIMENTAL PROCEDURE

This section gives the details of the ITO nanoparticle fillers used in this research; and the fabrication parameters used for controlling the microstructures of the PMMA-ITO nanocomposites. Subsequently, the different characterization techniques used for microstructural examination and properties characterization are also described.

3.1 Filler and Matrix Components

Three types of ITO nanoparticles were combined with PMMA particles to explore their effect on the microstructures of the PMMA-ITO nanocomposites. The three types of ITO nanoparticle fillers used will hereafter be referred to using capital alphabetical letters.

Table 3.1. Manufacturer Specifications for ITO and PMMA particles used in PMMA-ITO nanocomposites.

ITO Type	Particle Size	Surface Area	Surface Functionalized
A	≤ 50 nm	27 m^2/g	No
B	< 45μm	-	No
C	≤ 7 nm	-	Yes
PMMA	5-100 μm	-	-

Table 3.1 summarizes the manufacturer specifications of the ITO nanoparticles and PMMA particles. ITO Filler A and Filler B were purchased from Aldrich Co., and ITO Filler C was chemically synthesized. The details of the chemical synthesis of ITO Filler

C and its properties are described in Appendices A and B. The PMMA particles were purchased from Buehler Ltd.

3.2 Composite Fabrication Process

The PMMA particles and ITO nanoparticles were initially mixed either in cyclohexane (VWR Scientific), or by mechanical blending in air. Overall, four sets of PMMA-ITO nanocomposites were fabricated in this research, which will hereafter be referred to using roman numerals. Mechanical blending was used to process all of the nanocomposites after it was determined that the ITO nanoparticles adhered better to the PMMA particles in the absence of the cyclohexane. Table 3.2 summarizes the details for each set fabricated: I, II, III, and IV. All of the PMMA-ITO nanocomposites were formed into partial or full disc-shaped specimens using a Struers mounting press. At least three specimens were fabricated under identical conditions in order to obtained standard deviations for the measured properties. The compaction pressure and rate was controlled manually by a knob on the control panel of the mounting press. Figure 3.1 displays the Struers mounting press used in processing the nanocomposites and the top of the molding cylinder where the ITO-coated PMMA particles are compression molded. After each specimen was hot pressed, the molding cylinder was cooled to room temperature by circulated tap water.

The first set (I) was fabricated with the objective of determining which of the three ITO nanoparticle fillers yielded the most suitable microstructure. The PMMA-ITO nanocomposites in Set I were fabricated using 0.275 g of ITO-coated PMMA particles. This yielded nanocomposites having thicknesses of ~0.5 mm. The composition of the specimens was held constant at 0.4 vol.% ITO. The nanocomposites were formed using

Table 3.2. Sets of PMMA-ITO nanocomposites fabricated under different conditions.

Set	ITO Type	Range of ITO Concentration	Amount of Powder	Pressure	Temp.	Time
I	A, B, C	0.07 vol.%	0.275 g	6.4 MPa	~157°C	15 min.
II	A	0.0 – 1.6 vol.%	0.275 g	6.4 MPa	~157°C	15 min.
III	B	0.3 – 2.4 vol.%	0.275 – 2.0 g	6.4 – 51.3 MPa	~157°C	15 min.
IV	A	0.0 – 1.6 vol.%	2.0 g	25.6 MPa	~157°C	8 min.

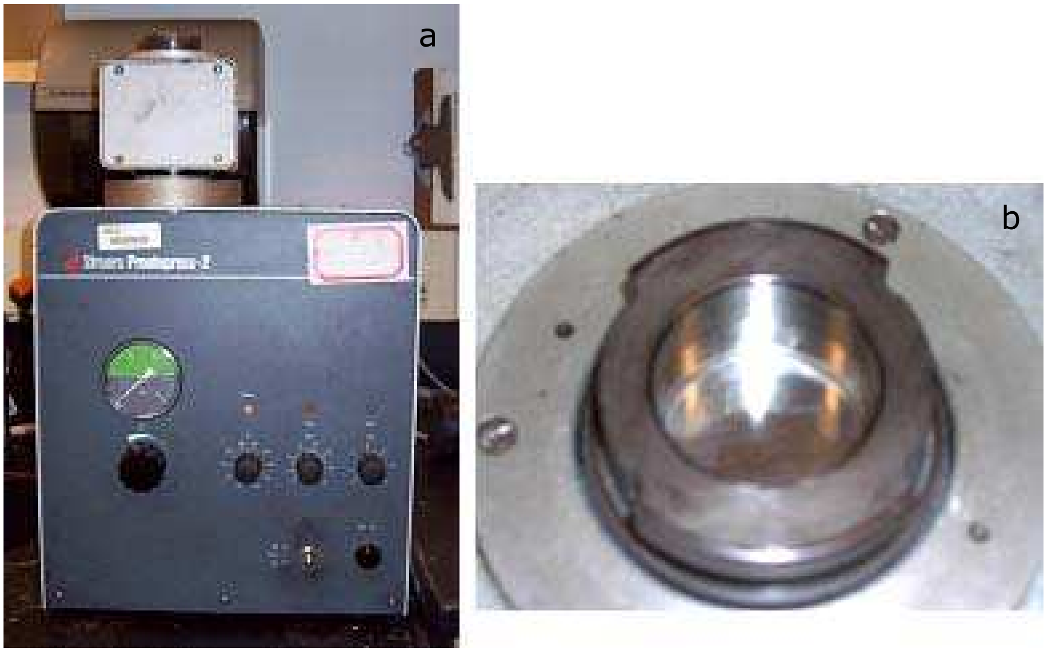

Figure 3.1. (a) Struers mounting press used to fabricate PMMA-ITO nanocomposites; (b) top of molding cylinder where ITO-coated PMMA particles were compacted in the mounting press.

6.4 MPa of pressure. The mounting press was set to 170°C for 15 minutes. However, a temperature label (Teletemp Model 110-6) placed inside the molding cylinder (near the top) indicated that the temperature only reaches between 155-160°C at this setting. Based on the data collected from Set I, the second set (II) of PMMA-ITO nanocomposites were fabricated using only ITO filler A with compositions ranging from 0.0-1.6 vol.% ITO. Set II of the nanocomposites were fabricated with the objective of determining the effect of the composition on the microstructure of the specimens. Similarly, the nanocomposites were formed with 0.275 g of ITO-coated PMMA particles, which yielded thicknesses of ~0.5 mm. The mounting press was set to 170 °C, corresponding to a temperature between 155-160°C inside the sample chamber. A pressure of 6.4 MPa was applied for 15 min. to the mixed PMMA and ITO particles during the molding process.

The third set (III) of PMMA-ITO nanocomposites were fabricated with the objective of studying the effect of the processing conditions on the electrical properties and improving the electrical conductivity of the nanocomposites. ITO filler B was used as the filler for Set III since more filler nanoparticles would be consumed for this experiment and ITO filler B was less expensive than ITO filler A. Set III of the nanocomposites had filler concentrations between 0.3-2.4 vol.% ITO. The compaction pressure was varied between 6.4-51.3 MPa for each composition. The sample thickness of the composites was controlled by hot pressing different amounts of ITO-coated PMMA particles (2.0 g, 1.0 g, 0.4 g, 0.275 g). The thickness was only varied for PMMA-ITO nanocomposites with 2.4 vol.% ITO. The compaction pressure was also varied in combination with the starting amount of powder for this composition. Compression molding different amounts of ITO-coated PMMA particles yielded composites with thicknesses ranging between ~0.5-2.0 mm. For all of the nanocomposites in Set III, the fabrication temperature and time were the same as for Sets I and II.

Based on the results of Set III, different processing parameters were used in the fabrication of the PMMA-ITO nanocomposites in Set IV. ITO filler A was used as the filler for Set IV. The filler concentration was varied between 0.0-1.6 vol.% ITO. The specimens were formed by application of 25.6 MPa of pressure for 8 min. to 2.0 g of ITO-coated PMMA particles. This yielded nanocomposites having thicknesses of ~2.0 mm. The mounting press was set to 170 °C, corresponding to a temperature between 155-160°C inside the sample chamber.

3.3 Microscopy and X-ray Diffraction

Optical micrographs of the specimens were acquired with the XSB 411 and LEICA DMRX microscopes without polarized light. Fractured cross-sections were examined with the LEO 1530 and the Hitachi S-800 scanning electron microscopes (SEM) operated at 15 kV. Images were acquired using the INLENS detector on the LEO 1530 SEM. In preparation for SEM, the nanocomposites were fractured at room temperature. It was important to fracture the nanocomposites below the glass-transition temperature of the PMMA matrix in order to avoid polymer flow and deformation artifacts which could alter the position of the filler. A coating of ~15 nm of gold was deposited onto the fracture surfaces with an EM350 sputter coater before SEM examination to prevent charging.

X-ray diffraction (XRD) was primarily used for confirming the phase and determining the average particle size of the three different types of ITO nanoparticle fillers. The nanoparticles were dropped onto a Si(510) zero-background substrates (The

Gem Dugout) prior to analysis either from an acetone or acetone/chloroform solution. High-resolution diffraction experiments were conducted on a Philips PW 1800 θ/2θ automated powder diffractometer (APD) with a Bragg Brentano geometry and Cu-Kα radiation. Scans were conducted in the range of 20° to 80° with a step size of $\Delta 2\theta = 0.03°$, allowing 3.6 seconds per step.

Transmission electron microscopy (TEM) was used to obtain high magnification images of the different types of ITO nanoparticle fillers. A JEOL 100CX II TEM operating at 100 kV was used at a magnification of 320,000X.

3.4 Optical Spectroscopy

Transmittance spectroscopy of the nanocomposites in Set II were acquired using a Beckman DU-640 spectrophotometer with a spot size of 2mm^2 at a scan speed of 1200 nm/min between 200 nm and 1100 nm wavelengths. Air was taken as the reference.

Refractive index and extinction coefficient values were measured for the nanocomposites in Set IV. The optical constant measurements were taken with a Metricon PC 2010 Waveguide coupler using the internal reflection intensity analysis (IRIA) technique.[75, 76] Measurements were conducted at room temperature using a 543 nm wavelength light source. The samples were measured at 300-400 different incident angles covering the total reflection to transmission regions and the intensities were recorded by two Keithley 2000 multimeters every 0.15º. Measurements of the composites were taken both in-plane and through the thickness using different optical polarizations. A more detailed description of the IRIA method is available elsewhere.[76, 77]

3.5 Ultra-Small Angle X-ray Scattering

Ultra-small angle x-ray scattering (USAXS) experiments were conducted on thin composite specimens. The objective was primarily to obtain the size distribution of the ITO nanoparticle aggregates formed in the polymer matrix. The USAXS analysis required the specimen thickness to be no thicker than ~0.5 mm.

USAXS experiments in slit-smeared configuration were performed at the Advanced Photon Source (APS) at Argonne National Laboratories. The energy of the x-rays used in the USAXS experiments was 11.9 keV. The data were calibrated to absolute intensity using the thicknesses of the specimens.

The slit-smeared data obtained from the USAXS experiments were analyzed using the Igor Pro (Wavemetrics Inc.) graphing and analysis package. Data reduction was accomplished using the Indra 2 package[78] and the reduced data were modeled using the Irena 2 package.[79] Modeling the scatter population, viz. the ITO aggregate distribution, was conducted under the assumption of a dilute limit. The volume distribution of the aggregates was obtained directly from the modeling results.

3.6 DC Electrical Measurements

Two-wire DC electrical measurements were taken of the different types of ITO nanoparticles fillers. The electrical measurements were taken by placing 0.3 g of ITO nanoparticles in a custom-made die having a cylinder made of nylon with a 10 mm inner diameter. Figure 3.2 shows the plastic die used to measure the conductivity of the ITO nanoparticles. Figure 3.3 displays the experimental set up used to measure the conductivity of the ITO nanoparticles. A two-wire connection was made across the stainless steel pistons using a Fluke 8840A multimeter. Pieces of paper towels were used

Figure 3.2. Image of custom-made plastic die.

Figure 3.3. Image of experimental set up used to measure the dc electrical conductivity of ITO nanoparticle fillers.

as insulation between the pistons and the platens of the Carver dry press to prevent any electric current from passing through the press. The conductivity of the nanoparticles was measured between 50-200 MPa.

3.7 AC Impedance Measurements

Impedance spectroscopy was used to measure the electrical resistance through the thickness of PMMA-ITO nanocomposite samples in Sets II, III, and IV. Prior to the measurements, the sample thickness (for conductivity calculations) was determined with a digital caliper (Mitutoyo Corp., model 500-196) to an accuracy of ±0.001 mm. Thickness measurements were taken at five different locations across the specimens and averaged. Conductive silver paint (SPI Supplies) was applied to each surface of the specimen to act as a current collector. The solvent contained in the silver paint was evaporated in a convection oven set to 80°C. After drying, it was confirmed that the resistance of each electrode was less than 1 Ω by a multimeter (Wavetek LCR55) in order to minimize the contact resistance during data acquisition.

The impedance spectra were collected between 10^{-2} and 10^{6} Hz by a Solartron 1260 Impedance/Gain Phase Analyzer combined with a Solartron 1296 Dielectric Interface. For the higher conducting composites (specifically belonging to Set (IV)), where it was necessary to acquire the impedance spectra at higher frequencies, the data was collected by a Hewlett Packard 4192 LF Impedance Analyzer between 10^{1} Hz and 10^{7} Hz. All of the electrical measurements were taken using 0.1 V_{rms} and without any dc bias. Figure 3.4 shows an image of the contacts made with the specimens for the electrical measurements.

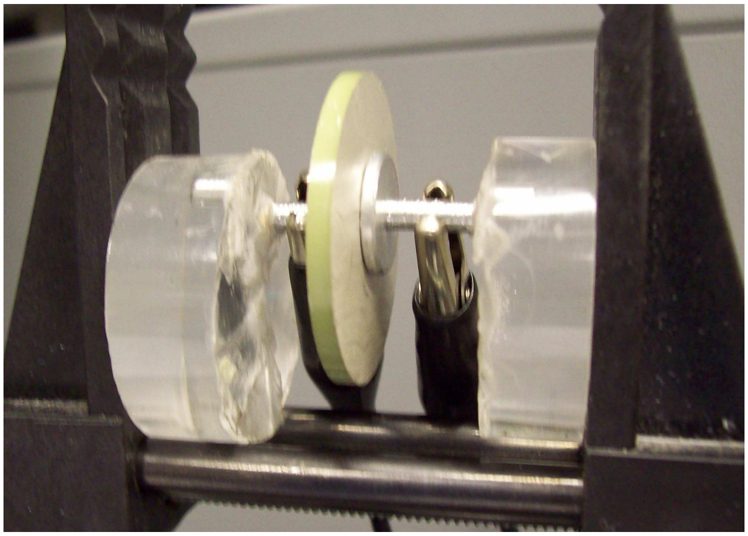

Figure 3.4. Image of contacts made across the thickness of the specimen for ac electrical measurements.

3.7.1 Calculation of specimen conductivity

The value of the dc resistance was taken from the intercept between the imaginary data and the real axis on the complex-plane impedance plot (Z’’ vs. Z’) and used to calculate the dc conductivity.[5] For very insulating samples, where the data did not intercept the real axis, the data was fit and extrapolated using an equivalent circuit of a resistance, R, and a constant phase element (CPE) in parallel. The equivalent circuit is defined by Equation 1:

$$Z^* = 1/[(1/R + Y_0(i\omega)^{\alpha}] \qquad (1)$$

where Y_0 is the CPE constant and α is the CPE power ($0 \leq \alpha \leq 1$).[80] Zview® software (Scribner Associates, Inc.) was used to perform a least squares fit of the insulating specimen data to Equation 1 in order to estimate the R and CPE values.

The resistance values were extracted from extrapolated or actual complex-plane impedance plots and used to calculate the dc electrical conductivity of the specimens using Equation 2:

$$\sigma = t / A \cdot R_{dc} \tag{2}$$

where t is the thickness of the specimen, A is the area of the electrode surface, and R_{dc} is the value obtained at the intercept between the imaginary data and the real axis.

CHAPTER 4

RESULTS AND DISCUSSION

In this chapter, the characterization results from the different sets of fabricated specimens, described in the experimental procedure chapter (Table 3.2, page 30), are presented and discussed. The first part of the chapter discusses the Set I specimens, where different mixing methods and different types of ITO nanoparticle fillers were explored. In the second part of the chapter, the microstructural evolution in Set II specimens, as the ITO concentration is varied, is discussed. The electrical and optical properties of the Set II nanocomposites are also examined. In the third part of the chapter, the effect of compaction pressure and sample thickness on the microstructure and electrical properties of Set III specimens is described. In the last part of the chapter, the electrical and optical properties of optimized Set IV nanocomposites are discussed.

4.1 Component Properties and Efficiency of Network Formation in PMMA-ITO Nanocomposites

4.1.1 Characterization of Results

SEM and optical micrographs of the PMMA particles used as the matrix materials in the nanocomposites are shown in Figure 4.1. The PMMA particles are spherical and have a wide particle size distribution between 5-100 μm, comparable to the specifications given by the manufacturer (Table 3.1). Figures 4.2a and 4.2b present XRD data obtained for the PMMA particles and a PMMA-ITO nanocomposite, respectively. The broad peaks around 14° and 30° indicate that the polymer is amorphous.[81] Figure 4.2b also shows three peaks at 21°, 30°, and 35° that correspond to the diffraction pattern for ITO.

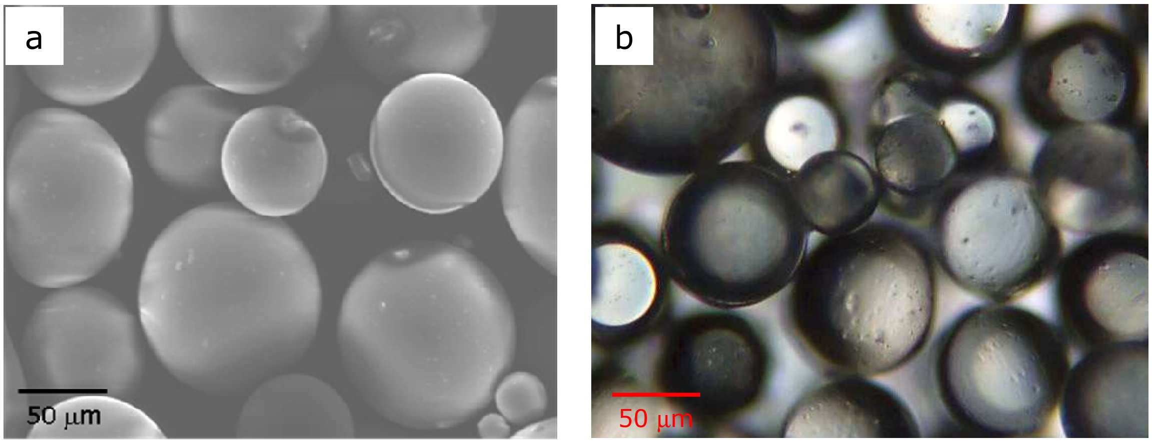

Figure 4.1. (a) SEM image of PMMA particles; (b) Transmission optical microscopy image of PMMA particles.

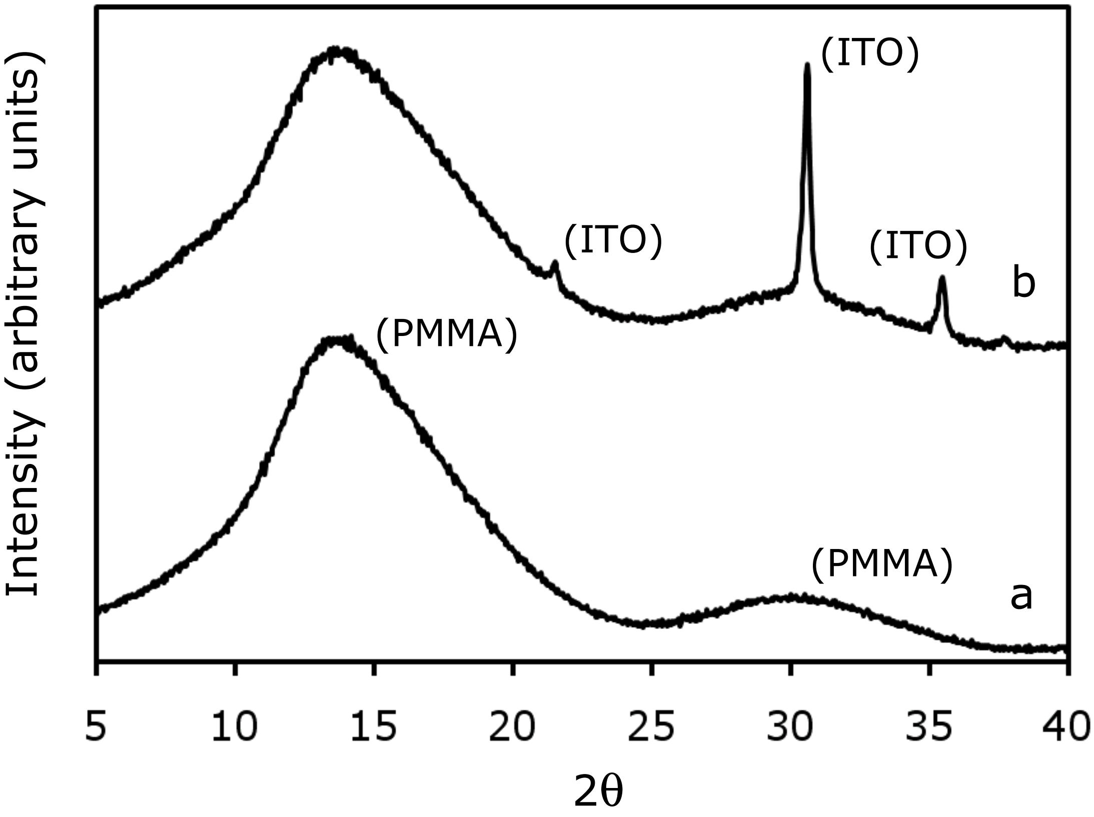

Figure 4.2. XRD pattern of (a) PMMA particles and (b) PMMA-ITO nanocomposite filled with 0.17 vol.% ITO.

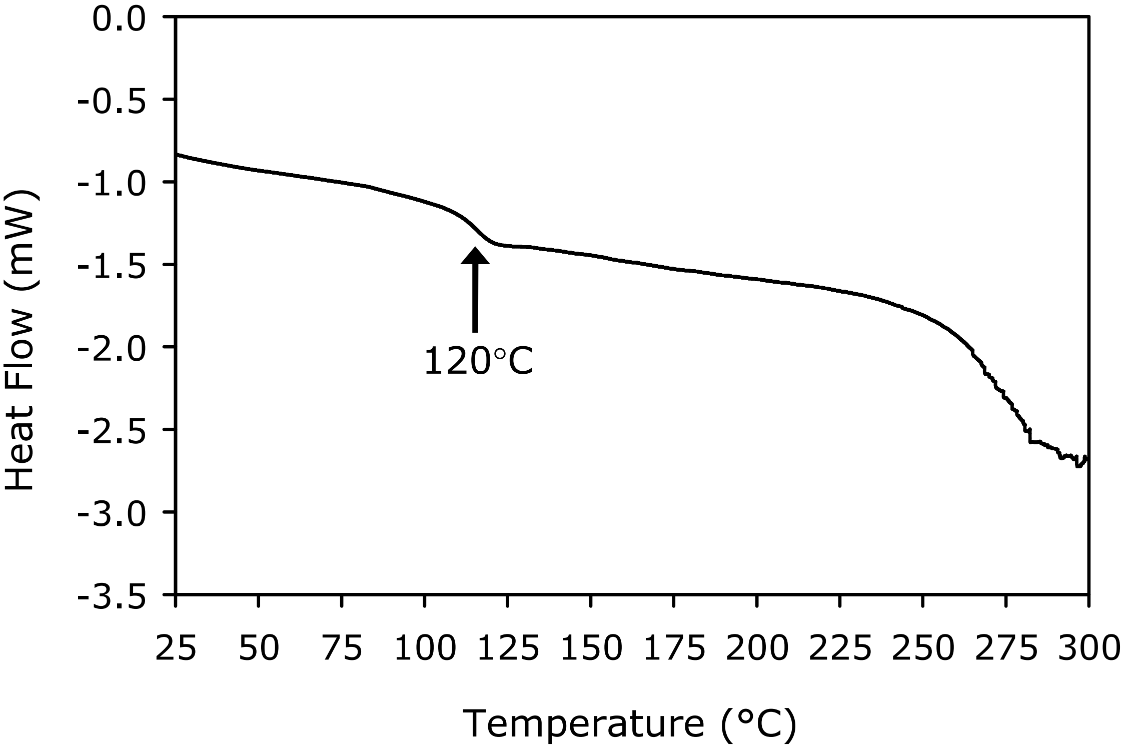

Figure 4.3. Differential scanning calorimetry scan of PMMA particles.

Figure 4.3 displays a differential scanning calorimetry (DSC) scan of the PMMA particles taken with a ramp rate of 20° C/min. The data shows that the PMMA has a glass-transition temperature around 120 °C, and a degradation temperature around 260°C.

TEM images of the three different types of ITO nanoparticle fillers (A, B, and C) are shown in Figure 4.4. The image of Filler A displays that the particle size distribution is bimodal, and is a combination of spherical 10-20 nm and 50-100 nm flat-edged crystals. Electron diffraction and energy-dispersive x-ray spectroscopy (EDS) analysis of the ITO nanoparticles indicate that both types of particles consist of the same cubic phase of ITO. The image of Filler B shows that the particles are much smaller than the size given in the manufacturer specifications (Table 3.1, page 28). Figure 4.4b also indicates that the particle size distribution is narrower than Filler A, and that the particles contain

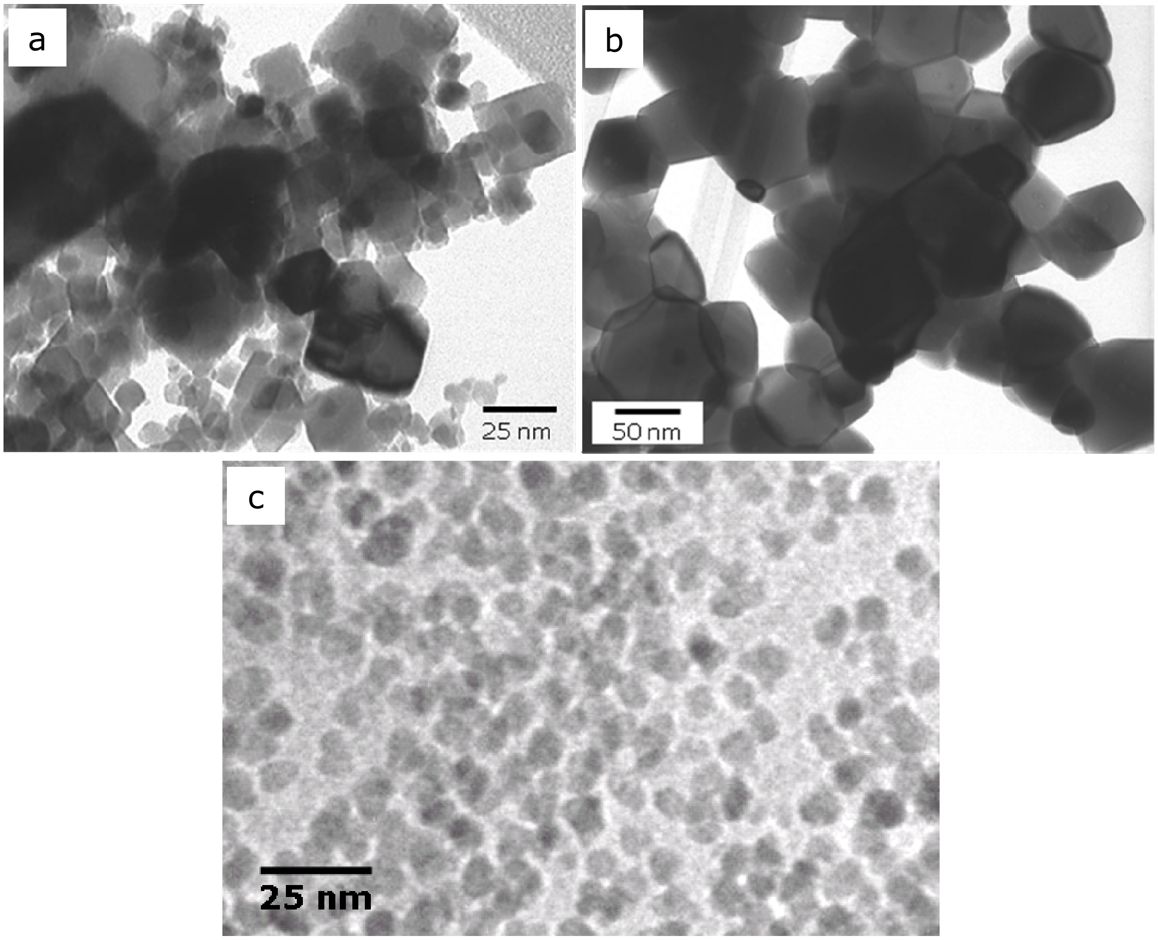

Figure 4.4. TEM images of three different types of ITO nanoparticles proposed as candidate fillers: (a) Filler A; (b) Filler B; (c) Filler C.

some flat-edges. Additionally, Filler B appears to be severely aggregated. Filler C possesses a narrow size distribution between 7-10 nm, and the TEM image does not show any significant agglomeration or aggregation.

XRD patterns for Filler A, B, and C are displayed in Figure 4.5. The peaks are centered at the peak positions of indium oxide having a cubic bixbyite structure (ICDD Card No. 6-416). The XRD patterns display no discernable tin oxide peaks or other indium compounds. The average particle size was calculated from the XRD patterns using the Debye-Scherrer formula:

$$t = \frac{0.9\lambda}{B\cos\theta} \quad (1)$$

where t is the grain size in nanometers, λ is the x-ray wavelength in nanometers (Cu Kα = 0.154 nm), B is the full width at half maximum (FWHM) of the XRD peak in radians, and θ is the Bragg diffraction angle.[82] Based on the calculation, Fillers A, B, and C possess an average particle size of 40.4 nm, 37.9 nm, and 6.8 nm, respectively.

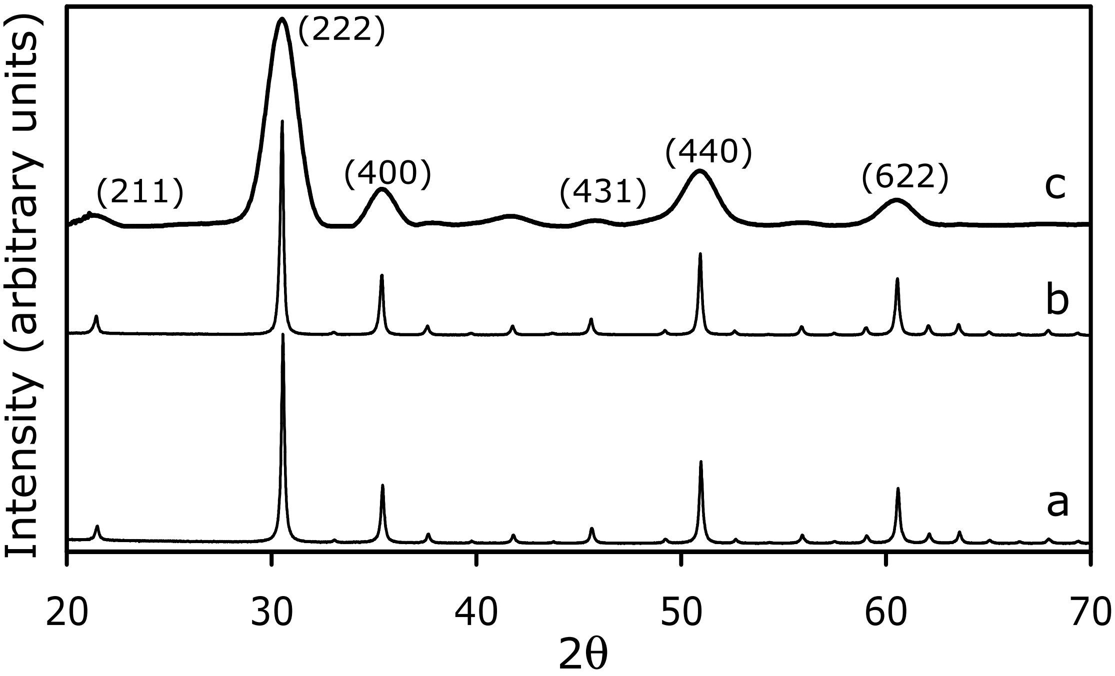

Figure 4.5. XRD of ITO nanoparticle Fillers A, B, and C.

The PMMA and Filler A were initially mixed by two different methods. The first method consisted of adding both particles to a glass flask with 20-25 mL of cyclohexane. The mixture stirred overnight by a Teflon stirring bar over a magnetic stirring plate. Subsequently, the cyclohexane was evaporated at room temperature under vacuum over an additional 24 hours. The second mixing method involved placing the PMMA and

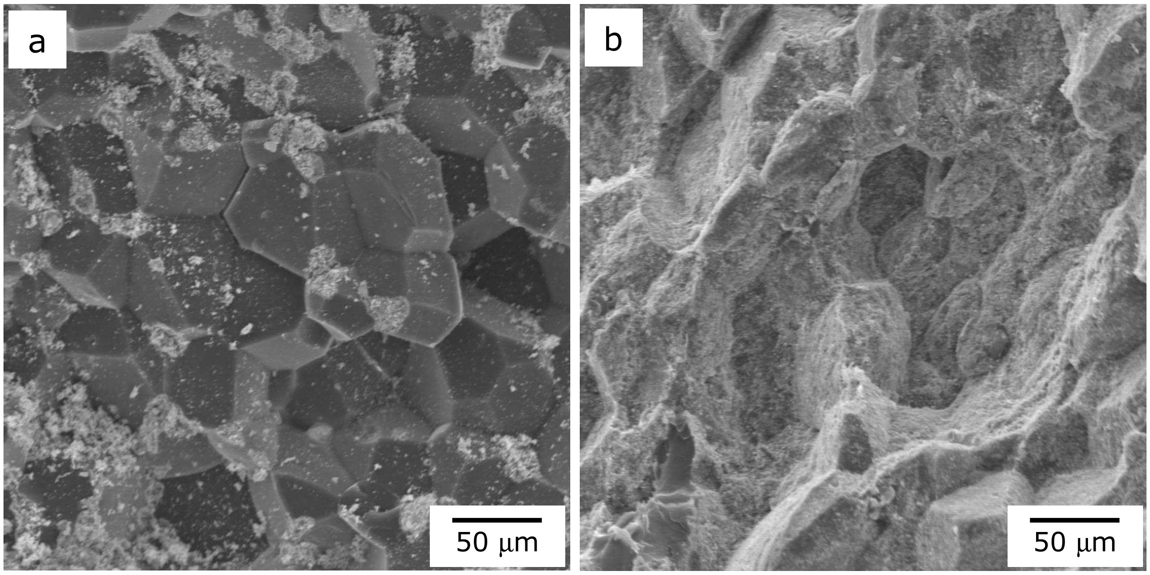

Figure 4.6. SEM images of cross-sections of PMMA-ITO nanocomposites formed from PMMA particles coated with 2.4 vol.% ITO by (a) mixing in cyclohexane with a magnetic stirring plate; and (b) mechanical mixing in air.

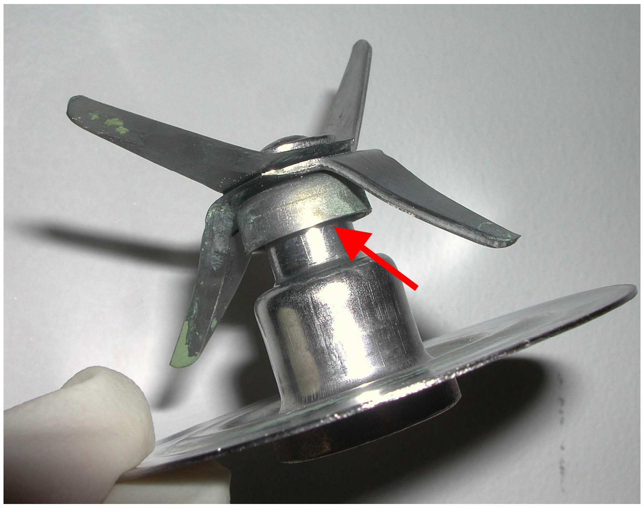

Figure 4.7. Source of severe aggregation underneath the cusp of the mixing blade.

Filler A particles in a plastic container and mechanically mixing in air, as described in the experimental section. Cross-section SEM images of specimens formed from the different methods (Figure 4.6) indicate that mixing in cyclohexane resulted in poor adhesion of the ITO nanoparticles to the surfaces of the PMMA particles. The ITO appears lighter than the PMMA in the SEM images.

Very large dark aggregates were visible to the eye in several batches of ITO-coated PMMA particles after mechanical mixing. Additional experiments showed a significant reduction in the number of large aggregates by mixing at lower speeds and removing trapped materials from underneath the cusp of the mixing blade after each time it was used. Figure 4.7 displays the mixing blade used in combining the PMMA and ITO particles with an arrow indicating where most of the residual trapped particles were found within the blade.

Figure 4.8 shows transmission optical micrographs and SEM images of the cross-sections of each nanocomposite fabricated in Set I. Figures 4.8a-b present a PMMA-ITO nanocomposite with 0.07 vol.% ITO Filler A. Figures 4.8c-d display a PMMA-ITO nanocomposite with 0.07 vol.% ITO Filler B. Figures 4.8e-f show a PMMA-ITO nanocomposite with 0.07 vol.% ITO Filler C. The ITO is darker than the PMMA in the optical micrographs.

Figures 4.8a-d reveal microstructures composed of polyhedral-shaped PMMA particles, and unusual displacement of ITO Fillers A and B. Figures 4.8a-b indicate that Filler A is green in color and has almost completely displaced to the edges of the PMMA particles after compression molding. As a result of the lack of particles remaining on the faces of the polyhedral-shaped PMMA particles, Figure 4.8b displays that trans-particle

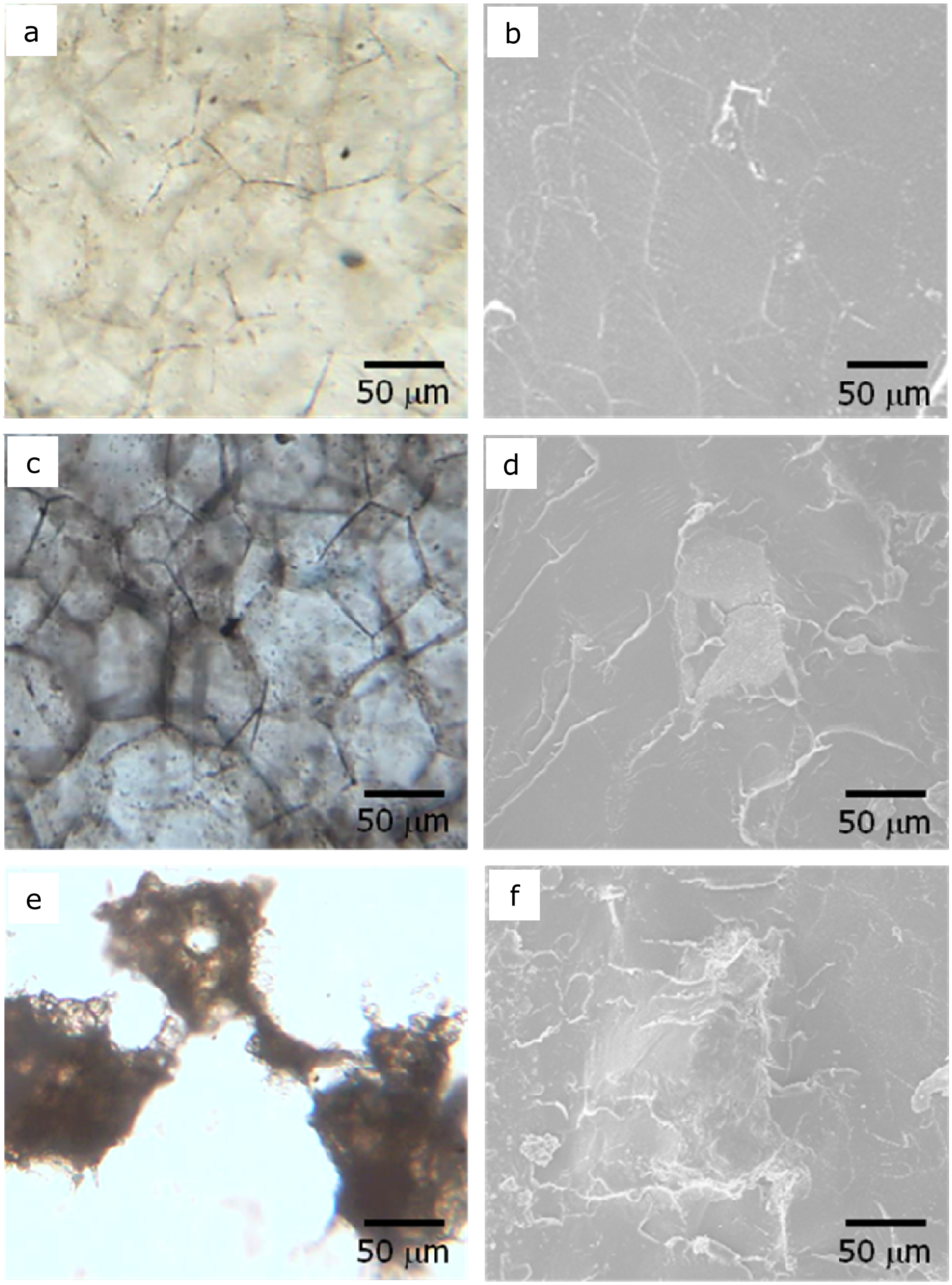

Figure 4.8. Transmission optical micrographs and SEM cross-section images for PMMA-ITO composites with 0.07 vol.% of different types of ITO. (a) micrograph of composite with Filler A; (b) SEM image of composite with Filler A; (c) micrograph of composite with Filler B; (d) SEM image of composite with Filler B; (e) micrograph of composite with Filler C; (f) SEM image of composite with Filler C.

fracture occurs through the cross-section upon mechanical failure. The PMMA-ITO nanocomposite with ITO Filler B also demonstrates some displacement of the ITO nanoparticles, but with less efficiency since some ITO nanoparticles can be seen on the surfaces of some of the PMMA particles in Figure 4.8d. As a result, this causes a combination of inter-particle and trans-particle fracture through the cross-section. Notably, the specimen shown in Fig. 4.8c-d is the only composite in Set I where the ITO nanoparticles were observed to turn gray after compression molding.

Figures 4.8e-f show that the PMMA-ITO nanocomposite exhibits an entirely different microstructure when ITO Filler C is used. ITO Filler C exists as huge agglomerates in the PMMA matrix, and appear to demonstrate no attachment or displacement with the PMMA particles after compression molding. As a result, complete coalescence of the PMMA particles occurs, and no grain structure is observed in the micrograph in Figure 4.8e. The composite with Filler C displays a smooth cross-section over the whole fracture surface.

4.1.2 Analysis and Discussion

Figures 4.1 and 4.4 show that the PMMA matrix particles are much larger than the ITO nanoparticle Fillers A, B, and C. Turner and co-workers[6-8] have shown that this criterion is necessary in order to form a highly phase-segregated microstructure via compression molding.

Mallarias *et al.*[6] and Bouchet *et al.*[13] both found that the filler particles adhere best to the polymer matrix particles when electrostatic forces are present. Figure 4.6 suggests that using cyclohexane as a medium to mix the particles is not the best method to coat the PMMA particles. It is speculated that the cyclohexane may leave a residue on the surface of the particles, which hinders the effects of electrostatic forces. Figure 4.6a also shows that the PMMA-ITO nanocomposite formed from particles mixed in cyclohexane exhibits inter-particle fracture over the cross-section despite the ITO nanoparticles not being well adhered to the surface of the PMMA particles. This also suggests that the cyclohexane prevents coalescence between the PMMA particles, which indicates a residue remaining on the surfaces of the PMMA particles after the cyclohexane was evaporated. Cyclohexane was chosen as the solvent because it has a fairly low vapor pressure and does not dissolve PMMA. However, the cyclohexane vapor pressure may have made it more difficult to remove from the surface of the particles than originally planned.

The large aggregates identified in the initial batches of the ITO-coated PMMA particles appeared similar to the materials removed from under the cusp of the mixing blade displayed in Figure 4.7. These large aggregates appeared to be composed of ITO particles, which were likely formed due to the shear force exerted on the materials when they were trapped between the inner and outer walls of the rotating cusps. In order to reduce the shear, the mechanical mixing was performed at the lower of the two available speeds. Additionally, in order to limit significant amounts of materials from being trapped under the cusp of the blade, the mechanical mixing was carried out in controlled discontinuous time intervals. By controlling the extent of continuous mixing, this minimized the number of particles that drifted underneath the cusp by the rotating blade.

Fractography of the PMMA-ITO nanocomposites is important to understanding the position of the ITO nanoparticles in the PMMA matrix. Crack propagation experiments with polymer-matrix composites having phase-segregated microstructures are typically used to identify the position of the filler in the microstructure.[5, 17, 20-22, 83] The location of the filler is determined by observing the type of fracture incurred along the cross-section of the specimens. Figure 4.9 shows examples of cross-sections when fracture occurs through the PMMA (trans-particle) and in between the PMMA particles (inter-particle) when they are coated with ITO.

Figure 4.9a shows the fracture surface of a PMMA sample that does not contain any ITO filler. When the neat PMMA fractures, the surface looks dark under SEM and contains ridges that are characteristic of mechanical failure in polymeric materials. In the PMMA-ITO nanocomposites (Figs. 4.8b, 4.8d, 4.8f) the regions where trans-particle fracture of the matrix particles occurs appear comparable to that shown for the neat PMMA (Figure 4.9a). Trans-particle fracture in the composites typically occurs when there is little or no filler present at the interfaces between the PMMA particles. Absence of ITO on the surface of the PMMA particles may result from either insufficient initial filler content, or partial penetration of the ITO into the bulk of the polymer particle during processing.[17, 21, 22] Coalescence of the polymer happens and fracture occurs through the polymer phase when ITO nanoparticles are absent from the surface of the PMMA particles.

Figure 4.9b displays the magnification of an interface between two PMMA particles along the cross-section of a PMMA-ITO nanocomposite that has undergone trans-particle fracture. The indentations, located perpendicular to the polymer phase boundary, indicate penetration of the PMMA by the ITO nanoparticles. As a result, some bonding between the PMMA particles along the interface can also be observed.

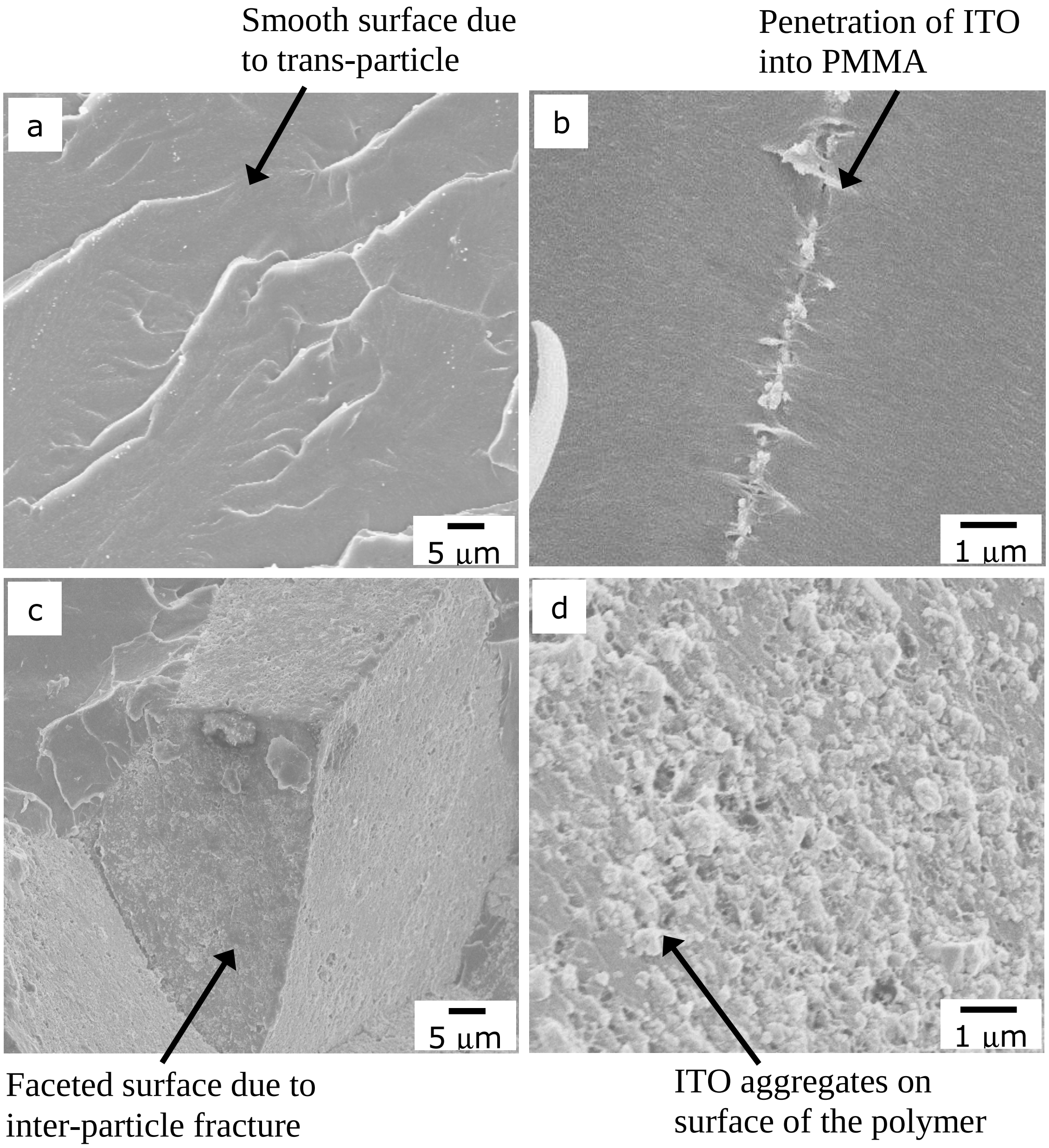
Smooth surface due to trans-particle

Penetration of ITO into PMMA

Faceted surface due to inter-particle fracture

ITO aggregates on surface of the polymer

Figure 4.9. Examples of trans-particle fracture for (a) neat PMMA; (b) a PMMA-ITO nanocomposite; (c) An example of inter-particle fracture for a PMMA-ITO nanocomposite; (d) Magnification of the surface of an ITO-coated PMMA particle shown in (c).[21]

Figure 4.9c presents an example of inter-particle fracture upon fracture of the PMMA-ITO nanocomposites. Inter-particle fracture indicates that an appreciable number of ITO nanoparticles are located at the interfaces of the ITO-coated PMMA particles. This is because coalescence of PMMA-PMMA interfaces is prevented, leaving the space between the ITO-coated PMMA particles as the easiest path for cracks to propagate through the microstructure. In the SEM images, inter-particle fracture can be recognized when the fracture surface appears faceted due to the isolation of individual PMMA particles. Figure 4.9c shows the cross-section of a PMMA-ITO composite at higher magnification than Figures 4.8b, 4.8d, and 4.8f. Only a few facets of a PMMA particle can be seen. Since the ITO is lighter in color than the PMMA under SEM, the surfaces of the faceted PMMA particle appear lighter when they are coated with the ITO. Figure 4.9d displays an even higher magnification image of the ITO-coated PMMA particle that is shown in Figure 4.9c. It can be seen that the ITO nanoparticles also exist as large aggregates on the surface of the PMMA.

The cross-sectional images of the microstructures show that the spherical PMMA particles (Fig. 4.1) deform into faceted polyhedral-shaped particles during compression molding of the samples (Figs. 4.6, 4.8, 4.9). Although this morphology may suggest a crystalline structure, Figure 4.2b shows that the PMMA remains amorphous after the ITO nanoparticles are added and the composite is formed, as expected. Based on sintering studies previously reported, the PMMA particles should exhibit pseudoplastic, viscoelastic flow for the compaction temperature and time used to form the samples.[45, 46] Consequently, this type of deformation can be expected due to the nature of the pressure distribution during fabrication, since the process occurs above the glass-transition

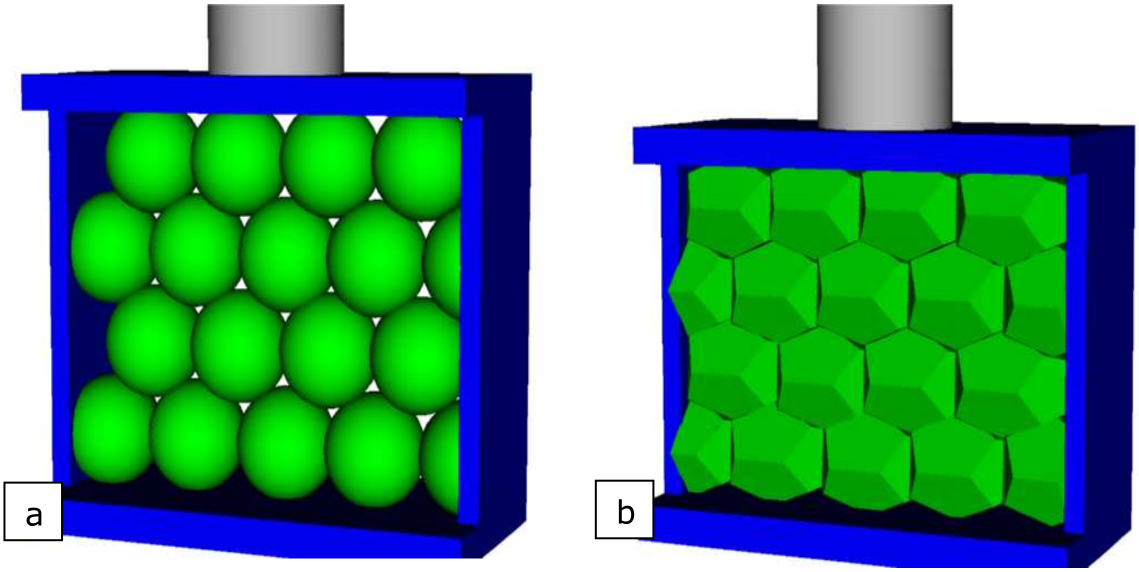

Figure 4.10. Schematic of ITO-coated PMMA particles forming a space-filling microstructure upon compression molding. (a) Starting ITO-coated PMMA particles; (b) Polyhedral deformation after compression molding.

temperature of the polymer phase (Fig. 4.3). There is sufficient driving force to reduce the open space between the packed spheres when force is applied to the spherical PMMA powders. As the polymer flow tends to displace air, a polyhedral morphology is the most efficient shape that can be obtained that will reduce the porosity and surface energy of the initially spherical particles.[83] Therefore, it is thermodynamically favorable to form a 'space-filling' microstructure, which necessitates the polymer phase to deform into polyhedral-shaped particles.[29, 84] A schematic of the packing process that occurs during compression molding is shown in Figure 4.10.

However, no other studies were found in the literature search that describes the spherical-to-polyhedral transition in morphology seen for the ITO-coated PMMA matrix particles except for the work reported by Gerhardt and co-workers.[5, 17, 21, 22] The reason that this morphology has never been reported for any polymer matrix materials before may be due to the fact that the polymer deformation is extremely sensitive to the pressing parameters and fabrication conditions used to form the composites. It has been observed that the microstructure and related properties of polymer-matrix nanocomposites are highly dependent upon the size of the filler,[6] the size ratio between the filler and the polymer matrix,[13-16] and the thickness of the composite,[21] as well as the applied pressure, temperature, heating time and cooling rate. More details about the effects of the processing parameters on the microstructure and properties will be addressed in Section 4.3.

Kusy proposed that there may be a propensity for the filler to occupy the interstitials between the polymer matrix particles upon compaction.[14] However, Figure 4.8a indicates an unusually large degree of displacement of the ITO Filler A. It happens that the interstitial voids in the microstructure take on the shape of narrow paths, due to the polyhedral morphology of the PMMA particles. This forces ITO Filler A to aggregate into structures that are comparable to wires at the interfaces of the PMMA particles (Figs. 4.8a, c). If these self-assembled ITO aggregate structures are responsible for percolation in the PMMA-ITO nanocomposites, this could lead to improved predictability of percolation in similar phase-segregated microstructures, provided the shape of the aggregates can be controlled in the similar manner demonstrated here.

Based on the data collected from Set I, the proposed microstructure is illustrated by Figure 4.11. Figure 4.11a shows an SEM image of the ITO-coated PMMA particles before compression molding. The ITO nanoparticles are visible as large aggregates that are dispersed across the surface area of the spherical PMMA particles.

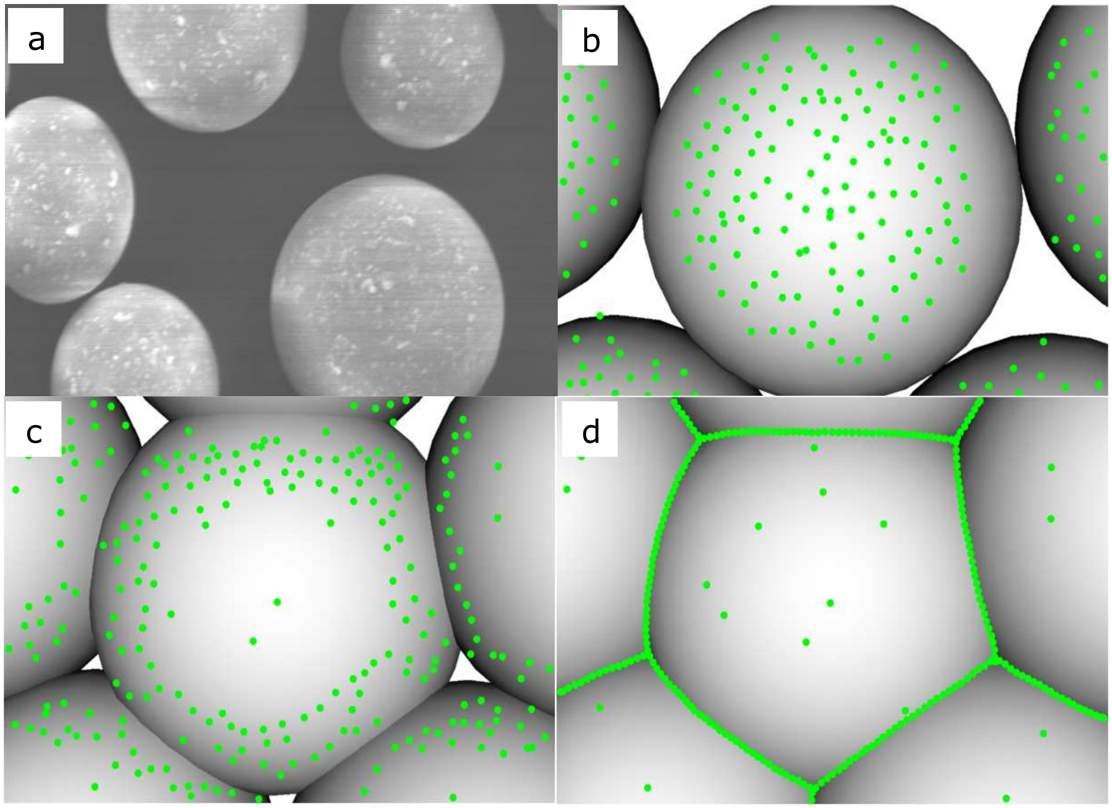

Figure 4.11. (a) SEM image of ITO-coated PMMA particles. Illustration of ITO-coated PMMA particles: (b) before compression molding, (c) during compression molding, and (d) after compression molding for a composite with an ITO concentration near the percolation threshold. The filler is depicted as small green particles, and the PMMA particles are depicted as large gray particles.

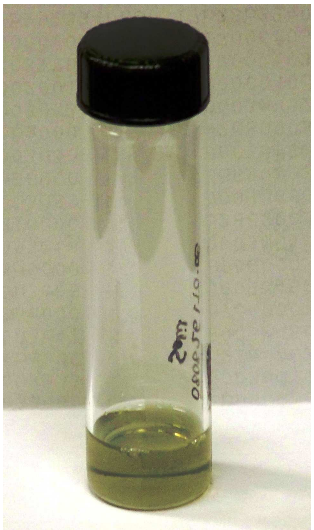

Figure 4.12. ITO Filler C dispersed in chloroform.

In Figures 4.11b-d, the ITO nanoparticles are represented by small green circles, and the PMMA particles appear as the larger gray shapes in the schematic. The 3-dimensional schematic specifically shows the deformation of the PMMA particles and re-arrangement of the ITO nanoparticles during compression molding. Before compaction (Fig. 4.11b), the PMMA particles are depicted similar to Figure 4.11a. During compression molding (Figs. 4.11c-d), the PMMA deforms into polyhedral-shaped particles, and the ITO nanoparticles are displaced to the edges of the newly deformed matrix particles.

Figures 4.8c-d also indicate some displacement of Filler B in a similar fashion to the schematic in Figure 4.11. There is likely less displacement due to the Filler B nanoparticles being severely aggregated as shown in the TEM image (Fig. 4.4b). For this particular sample, it was also observed that the ITO nanoparticles turned from green to gray in color after composite fabrication. This color is characteristic of ITO when a change in oxygen stoichiometry occurs. It is unclear why this change is not seen for Filler A, especially since Filler A has a higher surface area than Filler B. Figures 4.8e-f exhibit virtually no displacement of ITO Filler C in the PMMA matrix during composite fabrication. Figures 4.8e-f specifically show that the PMMA particles completely coalescence around the large ITO aggregates.

Due to the high surface area of ITO Filler C (~7-8 nm, Fig. 4.4c), there is a high tendency for the particles to aggregate (Fig. 4.8e) after the ligands are burned off. Figure 4.12 displays an image of the colloidal ITO Filler C in chloroform after the nanoparticles are isolated immediately after synthesis. The image shows that the ligands prevent the ITO nanoparticles from agglomerating in non-polar solvents. This behavior is typical of nanocrystal oxides that are precipitated in the presence of myristic acid.[85] In the future, it will likely be necessary to modify the method used to combine the ITO particles (made by colloidal methods) with PMMA particles in order to form nanocomposites with the desired phase-segregated microstructure. As a result of the agglomeration observed for Filler C after removal of the ligands, these nanoparticles were determined to be unsuitable as fillers for the PMMA-ITO nanocomposites in this research.

4.1.3 Conclusions

PMMA and ITO particles were mixed and compression molded to form nanocomposites with phase-segregated microstructures. SEM images indicate that mixing the components in air results in better adherence of the ITO nanoparticles to the surface of the PMMA particles. It was also found that controlling the speed and length of mixing of the particles resulted in smaller aggregates of ITO nanoparticles in the specimens.

Three different types of ITO nanoparticles were embedded in the PMMA matrix in order to study their effect on the resultant microstructure. The resultant microstructures of the nanocomposites were observed using transmission optical microscopy and SEM. It was shown that the position of the ITO nanoparticles around the PMMA particles could be determined based on the fracture surface characteristics along the cross-section of the nanocomposites. Typically, inter-particle fracture indicates that the ITO nanoparticles are located on the surface of the PMMA particles, and trans-particle fracture indicates that the ITO nanoparticles either occupy interstitials between the PMMA particles or have penetrated the surface of the PMMA particles.

Images of the microstructures of the nanocomposites showed that the PMMA particles transform from spherical to polyhedral-shaped upon compaction. The images also displayed that the nanocomposites filled with one type of ITO nanoparticles (Filler

A) exhibited significant displacement of the ITO nanoparticles towards the straight edges of the PMMA particles during compression molding. The ITO nanoparticles self-assemble into aggregates along the edges of the polyhedral-shaped PMMA particles; assuming structures similar to that of wires. The displacement is explained by it being thermodynamically favorable for the PMMA particles to form a space-filling microstructure during compression molding, and the free-flowing ability of the ITO nanoparticles. It was also shown that displacement of the ITO nanoparticles during compression molding is either less efficient or does not occur when the nanoparticles are initially aggregated (Filler B) or have ligands attached to their surfaces (Filler C).

4.2 Behavior of ITO nanoparticles as a function of concentration in Thin PMMA-ITO Nanocomposites[17]

4.2.1 Characterization of Results

In this section, the ITO concentration was varied in order to study the effect on the microstructure and electrical properties of the PMMA-ITO nanocomposites. For this set of specimens, ITO Filler A was used as the filler material. The details of the fabrication conditions for Set II are described in Table 3.2 on page 30. Transmission optical microscopy, SEM images, and impedance spectroscopy were used to characterize the nanocomposites. The objective was to correlate the variations in the microstructure to the electrical response in the specimens.

A transmission optical micrograph and cross-section image for a nanocomposite filled with 0.07 vol.% ITO was presented in the section 4.1.1 in Figure 4.8a-b. Figure 4.13 displays the effect on the microstructure when more ITO was added to nanocomposites that were fabricated by the same process as the specimen in Fig. 4.8a-b.

Figure 4.13 shows transmission optical micrographs and SEM images of the cross-sections for nanocomposites with concentrations of 0.50, 0.83, and 1.64 vol.% ITO. Figures 4.13a-b display the transmission optical micrograph and a cross-section SEM image of a PMMA-ITO composite containing 0.50 vol.% ITO. The optical micrograph for this nanocomposite appears more opaque than the micrograph shown for the composite with 0.07 vol.% ITO (Fig. 4.8a) and shows a higher concentration of ITO along the edges of the polyhedral-shaped PMMA particles. The cross-section SEM image (Fig. 4.13b) shows fractured surfaces that are characteristic of both inter-particle and trans-particle fracture. Agglomerates of ITO nanoparticles can also be seen on some of the flat faces of the PMMA particles, where facets can be seen. The location of the ITO nanoparticles across some of the flat faces is likely responsible for the increased opacity observed in the corresponding optical micrograph.

Figures 4.13c-d display the optical micrograph and cross-section SEM image of a composite filled with 0.83 vol.% ITO. The optical micrograph (Fig. 4.13c) shows that the specimen becomes less translucent as the ITO concentration in the matrix is increased. The ITO can clearly be recognized across the faces of the PMMA. The corresponding SEM image (Fig. 4.13d) shows more inter-particle fracture as well as additional ITO nanoparticle aggregates positioned on the flat faces of the PMMA particles. Consequently, this image best shows the polyhedral morphology of the PMMA in 3-dimensions with the ITO covering the polymer. The onset of the formation of ITO sheets appearing across the faces of the PMMA seems to be a result of the higher ITO content present in this composite. Figures 4.13e-f show the optical micrograph and

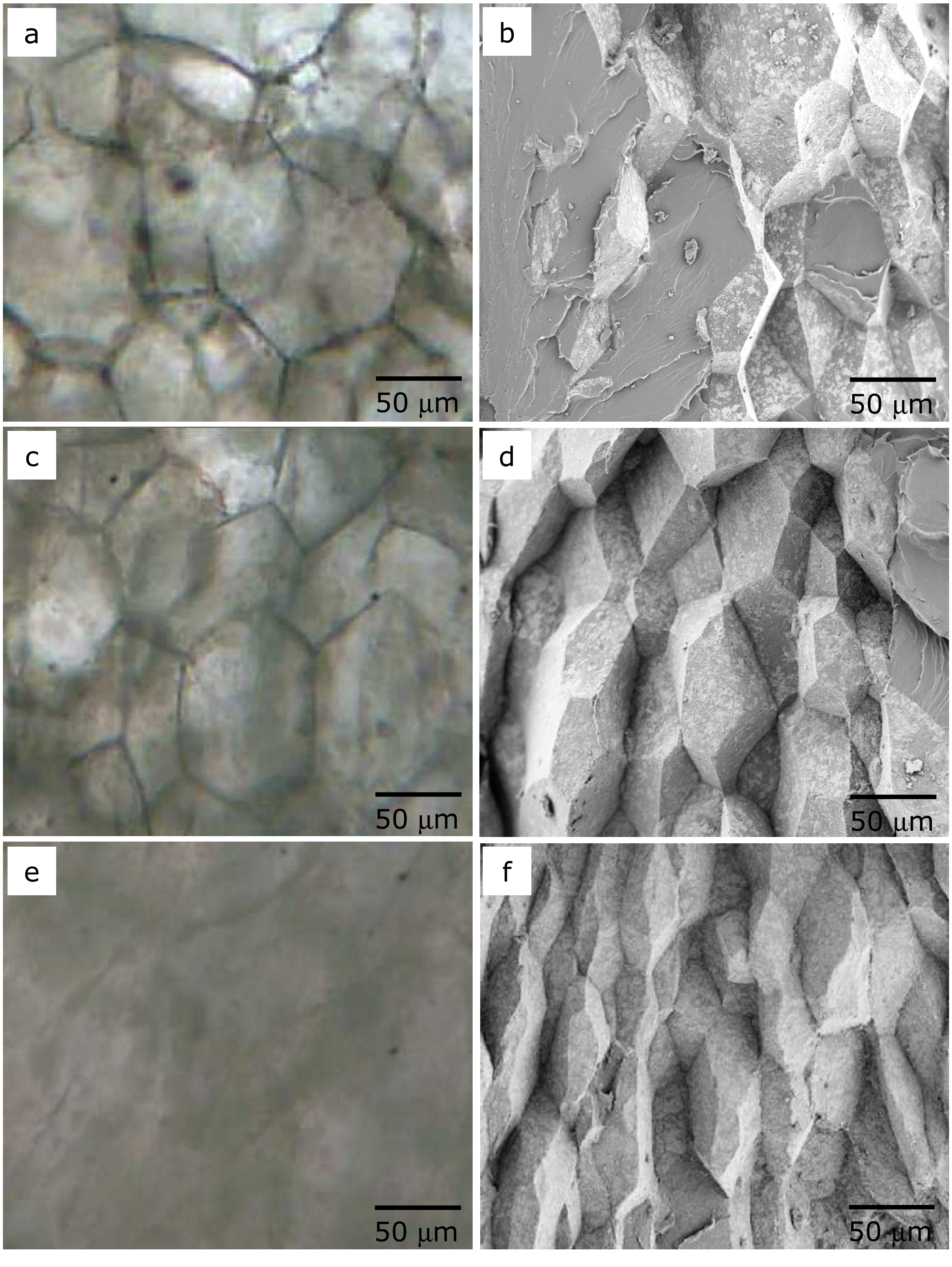

Figure 4.13. Transmission optical micrographs (TOM) and cross-section SEM images of PMMA-ITO composites with different ITO contents. a) TOM of composite with 0.50 vol.% ITO; b) SEM image of composite with 0.50 vol.% ITO; c) TOM of composite with 0.83 vol.% ITO; d) SEM image of composite with 0.83 vol.% ITO B; e) TOM of composite with 1.64 vol.% ITO; f) SEM image of composite with 1.64 vol.% ITO.[17]

cross-section SEM image of a composite filled with 1.64 vol.% ITO. There are no significant features that are identifiable in the optical micrograph (Fig. 4.13e) due to the high concentration of ITO and resulting opacity. However, the corresponding SEM image for this specimen (Fig. 4.13f) shows inter-particle fracture over the entire cross-section of the nanocomposite. The SEM image also reveals that there is preferential deformation of the PMMA powders in one direction. The preferential deformation is seen to occur parallel to the pressing direction used in the compression molding. This may also be attributed to the higher ITO content, and will be addressed in the discussion section.

Figure 4.14 displays the electrical conductivity of the ITO Filler A used for the PMMA-ITO nanocomposites used in Set II. The bar graph indicates conductivities between 0.02-0.11 S/cm when pressures between 50-200 MPa are applied to un-sintered ITO Filler A nanoparticles.

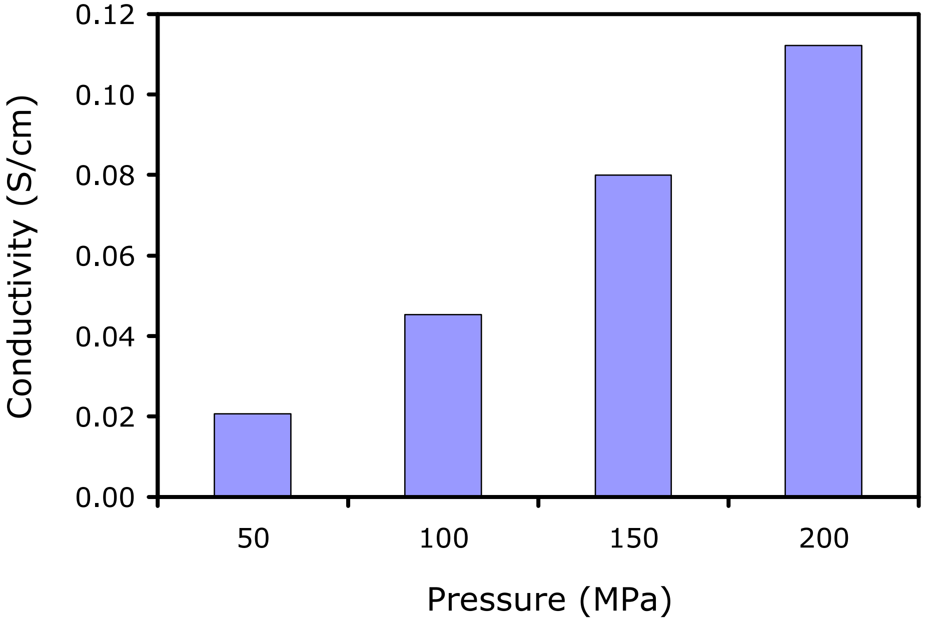

Figure 4.14. Electrical conductivity of un-sintered ITO Filler A nanoparticles as a function of pressure.

Figure 4.15 displays complex plane impedance plots for the PMMA-ITO nanocomposites, where the imaginary part of impedance is plotted against the real part of impedance. Complex plane impedance plots typically display semicircles, with frequency decreasing from left to right. A large semicircle indicates a large resistance and, thereby, a more electrically insulating sample while a small semicircle corresponds to a small resistance and a more electrically conducting sample. In the different parts of Figure 4.15, the semicircles had to be viewed on two different scales since the resistance values changed over several orders of magnitude as a result of percolation. Percolation in insulator-conductor composites such as these can cause the transition from an insulating electrical response to semi-conducting behavior. In Figure 4.15a, the data markers, which form a small arc, represent the experimental data of a composite with 0.17 vol.% ITO, and the solid line is the fitted curve used to estimate the impedance of the sample. Only a small part of the semicircle can be observed due to the highly insulating behavior of this sample. Therefore, an equivalent circuit of a resistance, R, and a constant phase element (CPE) in parallel was used to fit the experimental data, as described in section 3.7.

Figure 4.15b shows higher magnifications of the origins of the plots in Fig. 4.15a to reveal smaller semicircles for the more conducting specimens, specifically composites with 0.50, 0.74, 0.83, and 1.64 vol.% ITO. The dc resistance values of these samples were taken from the intercepts of the semicircles with the real axis. The values at the intercepts are used to calculate the dc resistivities (and hence the conductivities) of the composites.

The dc conductivity of the PMMA-ITO nanocomposites as a function of ITO content is shown in Figure 4.16. The error bars include data from at least three different

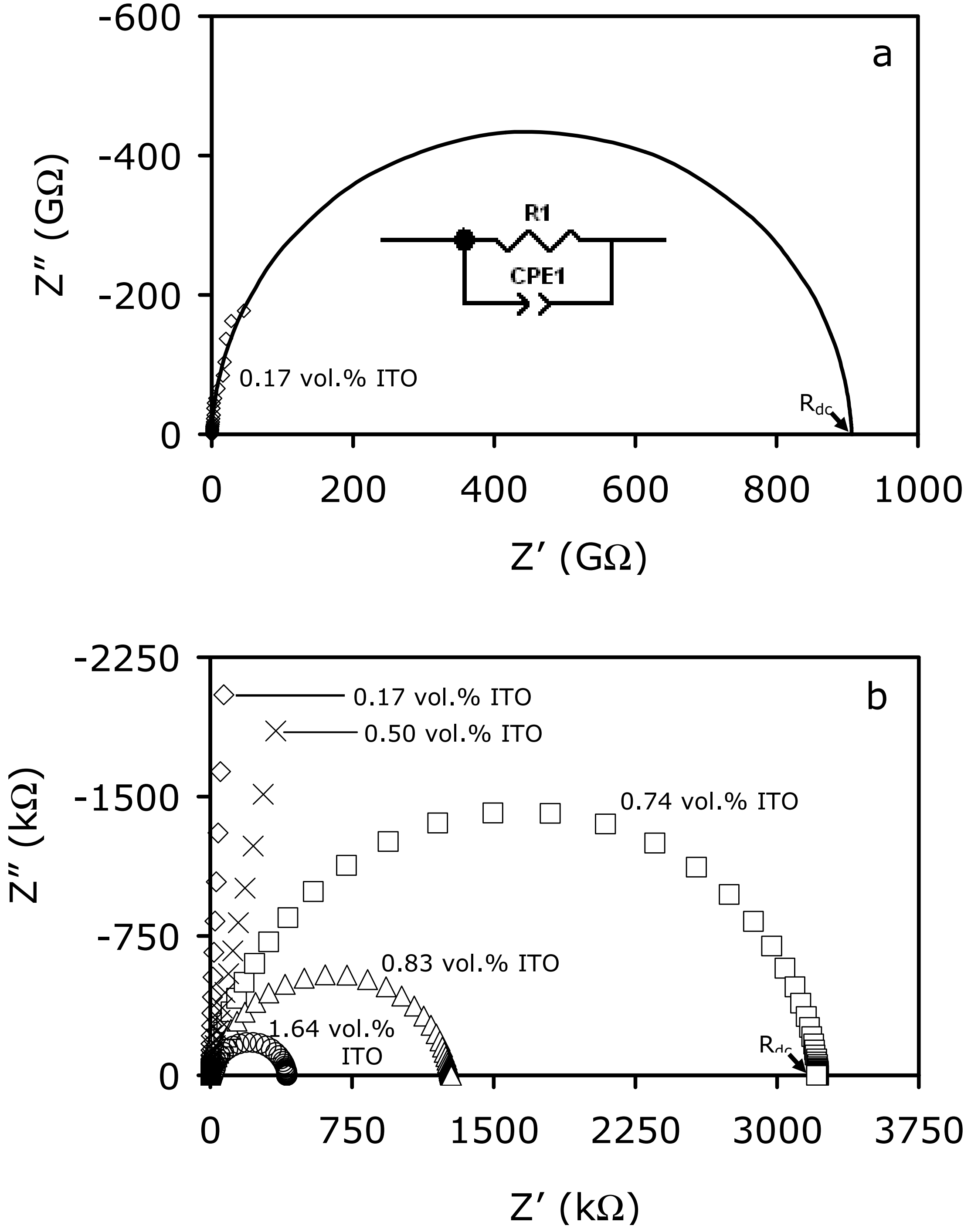

Figure 4.15. Representative complex plane impedance plots of individual PMMA-ITO nanocomposites. Part b is a magnification of the origin of part a.

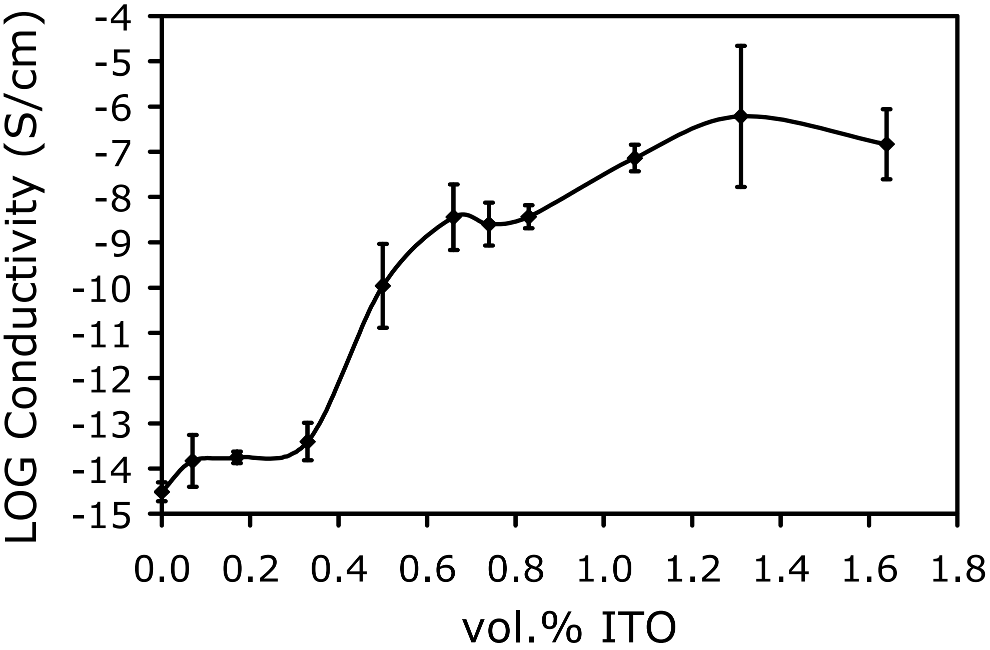

Figure 4.16. Electrical conductivity of PMMA-ITO nanocomposites as a function of ITO content.

specimens for each composition, all fabricated under the same conditions. It is speculated that the bimodal distribution of the ITO nanoparticles and the PMMA size distribution have contributed to some of the larger standard deviations seen in the data. The electrical conductivity of the PMMA-ITO nanocomposites remains comparable to that of pure PMMA until 0.2 vol.% ITO content. Between 0.2-0.6 vol.% ITO there is an increase in the conductivity by approximately six orders of magnitude. Between ~0.7-0.9 vol.% ITO there is a small plateau and the electrical conductivity remains relatively constant within this composition range. When the ITO content is increased to over 1.0 vol.% ITO, the conductivity rises again by approximately one order of magnitude. Although the final composition (1.64 vol.% ITO), a minor decrease in the conductivity is detected. Notably, the maximum conductivity achieved in the nanocomposites is much lower than the conductivity measured for the ITO nanoparticles. This can be attributed to weak physical contact or contact resistance between the ITO nanoparticles in the specimens.[6]

The degree of transparency observed in the optical micrographs of the PMMA-ITO nanocomposites is quantified by transmittance spectroscopy data shown in Figure 4.17. Figure 4.17 displays the transmittance spectra between 200-1100 nm, from the ultra-violet (UV) region to the near infrared (IR) range. The typical absorption edge for PMMA is observed in the UV region of the graph.[86, 87] Figure 4.17 shows that the transmittance in the visible light region (400-700 nm) is depressed as more ITO nanoparticles are added. Beyond the composition of 0.50 vol.% ITO, the spectra become more difficult to distinguish between the specimens with different filler concentrations. The decrease in transmittance correlates well with the transmission optical micrographs of the PMMA-ITO nanocomposites that contained higher concentrations of ITO. Notably, Figure 4.17 does not reveal a reflection edge for any of the spectra taken of the specimens. A reflection edge in the IR region is characteristic of ITO due to inherent free electrons.[67, 88] In the case of the PMMA-ITO nanocomposites, it is speculated that a reflection edge is not observed due to interactions between the PMMA and ITO particles at their interfaces. Figure 4.18 displays the UV-Vis-IR transmittance spectrum obtained from ITO Filler C dispersed in chloroform (non-polar solvent). The transmittance spectrum for Filler C indicates that ITO nanoparticles may exhibit a reflection edge in the absence of the PMMA particles.

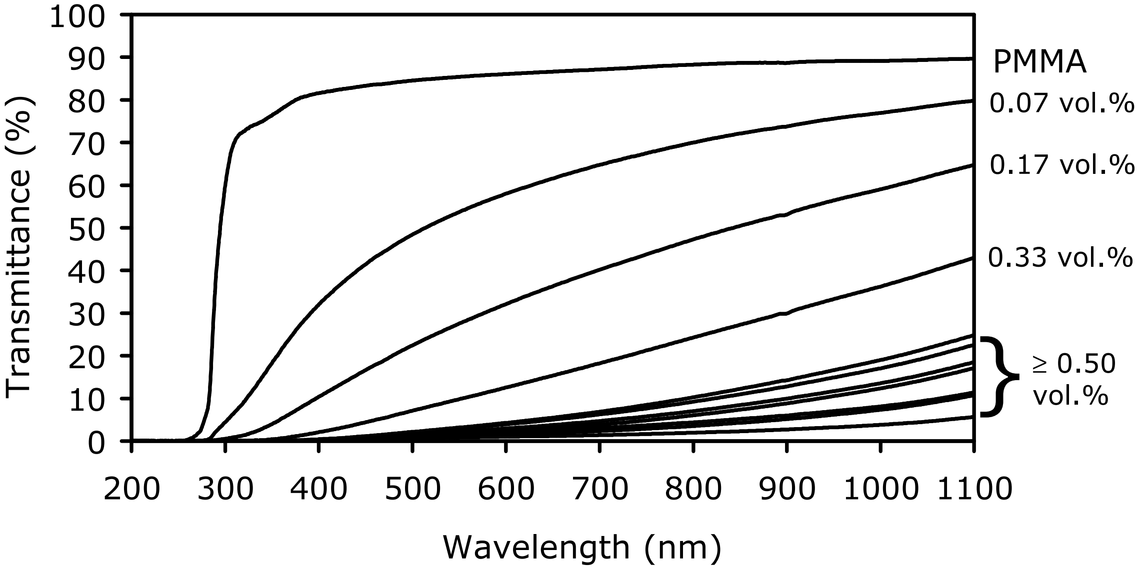

Figure 4.17. Transmittance spectra of PMMA-ITO nanocomposites between 200-1100 nm.

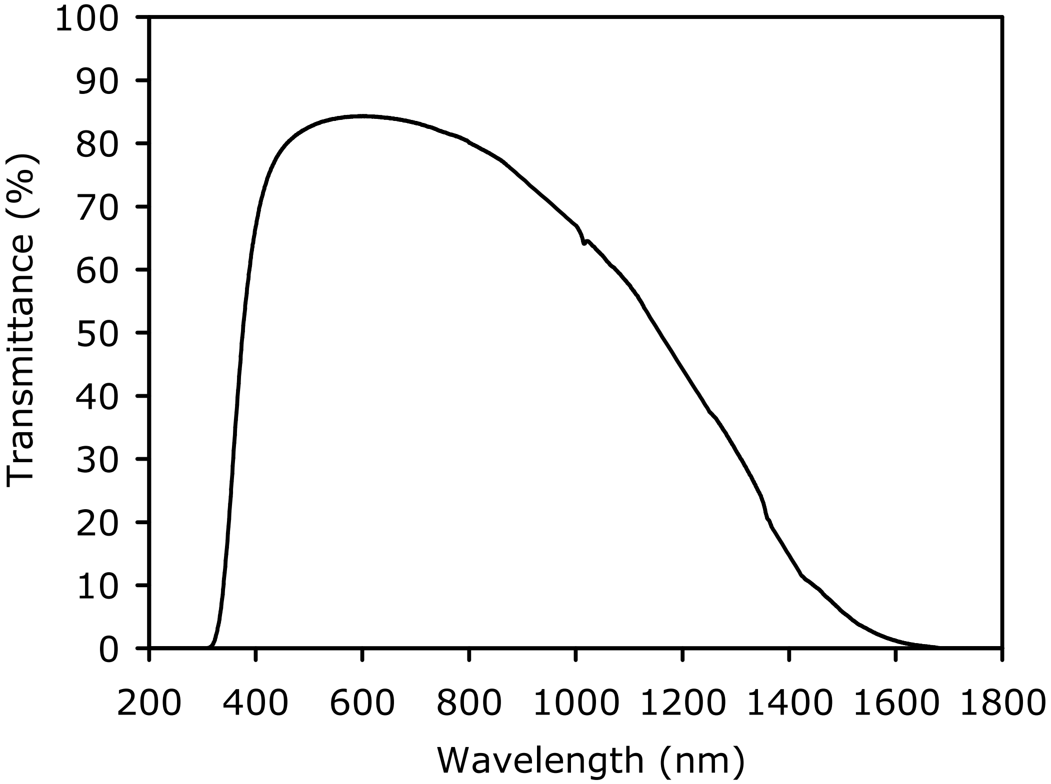

Figure 4.18. UV-Vis-IR transmittance spectra of ITO Filler C dispersed in chloroform.[67]

4.2.2 Analysis and Discussion

The optical micrographs and SEM images depicted in Figure 4.13 demonstrate the unique behavior of the faceted microstructures in the PMMA-ITO nanocomposites. These results are in agreement with several other polymer-matrix nanocomposites containing similar microstructures that have been previously reported by Gerhardt and co-workers.[5, 18, 20, 23]

One of the most interesting characteristics in the microstructures of the nanocomposites is the process by which a conducting network of ITO nanoparticles apparently forms in the PMMA matrix of the samples. Despite becoming widely accepted that percolation in segregated network microstructures occurs by the filler remaining undisturbed during hot pressing, the electrical and microscopy data presented in this research suggests that this is not the case for the PMMA-ITO nanocomposites.

Although the ITO is spread over the entire surface of the PMMA particles prior to compaction (Fig. 4.11a), the images of the microstructures (Fig. 4.13) show that the ITO nanoparticles collect and align along the edges of the polyhedral PMMA after more ITO is added. The effect of pressure, viscosity of the polymer matrix, and surface forces may all affect the redistribution of the filler. It can be surmised that the viscosity of the PMMA particles is too high to be penetrated by the ITO nanoparticles at the compression molding temperature used (~157°C). Even though the pressure does not provide enough force for the ITO nanoparticles to penetrate the surface of the PMMA particles, there is still sufficient energy available for the PMMA to flow and displace the ITO nanoparticles. Thus, the polymer fills the space that the ITO initially occupied and the ITO is carried towards the interfaces between the PMMA particles (see Fig. 4.11). After the ITO is displaced, the edges of the polyhedral PMMA particles become the primary site for contact between the ITO nanoparticles, which ultimately leads to the formation of an interconnected ITO network similar to the appearance of wires (Figs. 4.13a-b).

Further evidence that the ITO concentrated along the edges of the polyhedral PMMA particles forms an interconnected 3-D network is indicated by the significant increase in the conductivity of the nanocomposites at the compositions where only that feature is dominant. This is seen to occur at concentrations between 0.33-0.50 vol.% ITO for the PMMA-ITO nanocomposites fabricated under these processing conditions (Fig. 4.16). Such a low percolation threshold value is generally characteristic of polymer matrix composites containing phase-segregated microstructures.[5-10, 12, 13, 16, 17, 19-23] The data presented in Figure 4.16 is consistent with classical percolation theory:

$$\sigma_{dc}=\sigma_{m}|p - p_{c}|^{t} \tag{2}$$

where σ_{dc} is the dc conductivity of the composite, σ_{m} is the conductivity of the conducting phase, p is the volume fraction of the conducting phase, p_c is the volume fraction near the percolation threshold, and *t* is a system-specific value.[89, 90] The expression states that the conductivity in the system is expected to increase by several orders of magnitude around the percolation threshold.

The conductivity data also correlates well with the data collected by the UV-Vis-IR transmittance measurements, which shows a significant reduction in the transmittance after around the percolation threshold (Fig. 4.17). This reduction in the transmittance is common when percolation occurs in composites containing transparent materials, due to scattering effects caused by the continuous inter-particle contact established between the filler particles.[86]

The optical micrographs and SEM images of the composite filled with 0.50 vol.% ITO (Figs. 4.13a-b) show that the ITO is heavily concentrated along the edges of the polyhedral PMMA particles at this composition. Even though the ITO is also shown to occupy some of the flat faces of the PMMA, it appears to be discontinuous over the faces across the sample thickness, which strongly suggests that percolation is achieved as a result of a network formed along the edges of the polyhedral-shaped PMMA particles.

The electrical conductivity data shows that after percolation occurs, the conductivity of the composites remains relatively constant as the concentration is increased to ~0.8 vol.% ITO (Fig. 4.16). The transmission optical micrographs and SEM images for the composite filled with 0.83 vol.% ITO (Fig. 4.13c-d) show that the ITO continues to accumulate across the faces of the polyhedral PMMA at these compositions. The presence of the ITO on the faces of the PMMA is also indicated by the decrease in optical transmittance at this composition (Fig. 4.17). It is believed that the ITO begins to occupy the faces as a result of the edges of the PMMA particles becoming completely filled by the ITO. Although the polymer was easily able to displace the ITO at lower concentrations, the quantity of ITO above the percolation threshold is large enough that displacement of the ITO becomes too difficult. As a result of the ITO nanoparticles occupying the faces of the PMMA, room temperature fracture causes crack propagation to occur between the ITO-coated, polyhedral-shaped PMMA particles. Fracture surfaces of nanocomposites containing ITO concentrations above the percolation threshold reveal an ordered, faceted cross-section.

Further increases in the ITO content have an additional effect. As can be seen in the optical micrograph and SEM image of the PMMA-ITO nanocomposite filled with

1.64 vol.% ITO, the polyhedral PMMA particles are now completely covered by the ITO (Fig. 4.13e-f). As a result, the wire-network is no longer visible and the transmittance of visible light is minimal due to scattering by the ITO inter-particle contacts (Fig. 4.17). The small rise in electrical conductivity as the ITO content is increased beyond ~1.0 vol.% ITO (Fig. 4.16) may be attributed to the interconnectivity of the ITO nanoparticles that form sheets across the faces of the PMMA particles.

The SEM image of the composite with 1.64 vol.% ITO shows some uniaxial deformation of the polyhedral-shaped PMMA particles along the pressing direction. This suggests that the flow of the PMMA becomes restricted by the high concentration of ITO nanoparticles, thus limiting the space available to both phases during compaction. The specimens likely become more rigid as a result of increasing the concentration to 1.64 vol.% ITO due to the formation of the ITO nanoparticle sheets that surround the PMMA. This may generate normal forces, which can cause some of the ITO nanoparticles to penetrate the surface of the PMMA particles. This can cause the conductivity of the PMMA-ITO nanocomposites to slightly decrease since some of the ITO nanoparticles become electrically isolated inside the PMMA particles.

4.2.3 Conclusions

Correlation between the electrical, optical, and microstructural data of PMMA-ITO composites has been established in order to provide insight about the effect of the ITO concentration on the properties and microstructures of the PMMA-ITO nanocomposites. The results for the nanocomposites described in this section demonstrate that the ITO nanoparticles first accumulate along the edges of the PMMA particles until the concentration equals the percolation threshold, which occurs around 0.50 vol.% ITO.

At concentrations equal to or lower than the percolation threshold, the ITO nanoparticles assemble into three-dimensionally interconnected wire-like aggregates along the edges of the polyhedral-shaped PMMA particles. Beyond the percolation threshold, the ITO nanoparticles begin to form conducting sheets across the flat faces of the PMMA particles. These results significantly contrast from previous studies, which proposed that percolation in segregated network microstructures only occurred as the result of limited or no displacement of the filler on the surface of the polymer particles during composite fabrication; and that percolation should not occur unless an interconnected network existed across the faces of the polymer matrix particles.[6-8] The effects of the composite fabrication parameters on the microstructure and properties of the PMMA-ITO nanocomposites will be examined in Section 4.3.

4.3 Optimization of Fabrication Conditions for Improved Conductivity/Microstructure

4.3.1 Characterization of Results

In this section, the ITO concentration, compaction pressure, and sample thickness are varied in order to study the effect on the microstructure and electrical properties of the PMMA-ITO nanocomposites. For this set of specimens, ITO Filler B was used as the filler material. The details of the fabrication conditions for Set III are described in Table 3.2 on page 30. SEM images and impedance spectroscopy were used to correlate variations in the microstructure to the changes in the electrical properties of the nanocomposites.

The effect of compaction pressure was studied for all nanocomposites that were fabricated using 0.4 g of powder consisting of ITO-coated PMMA particles. Figure 4.19

describes the electrical conductivity of the ITO Filler B used for the PMMA-ITO nanocomposites in Set III. The bar graph indicates conductivities between 2-3 S/cm when pressures between 50-200 MPa were applied to un-sintered ITO Filler B nanoparticles. Notably, these nanoparticles possess a higher electrical conductivity than Filler A by 1-2 orders of magnitude. Although the certificate of analysis issued by Aldrich Co. confirmed that both Filler A and Filler B contained 10 at.% Sn, it is speculated that the difference in electrical properties between the nanoparticles may be attributed to different oxygen contents in the nanoparticles.

Figure 4.20a shows the ac conductivity as a function of frequency for PMMA-ITO nanocomposites filled with 0.3 vol.% ITO made using 6.4, 25.6, and 51.3 MPa. The data show that the conductivity is frequency dependent in the entire frequency range for all samples of this composition. This is typical of specimens with compositions below the percolation threshold, which tend to exhibit electrically insulating behavior.[5, 21, 22, 80, 89]

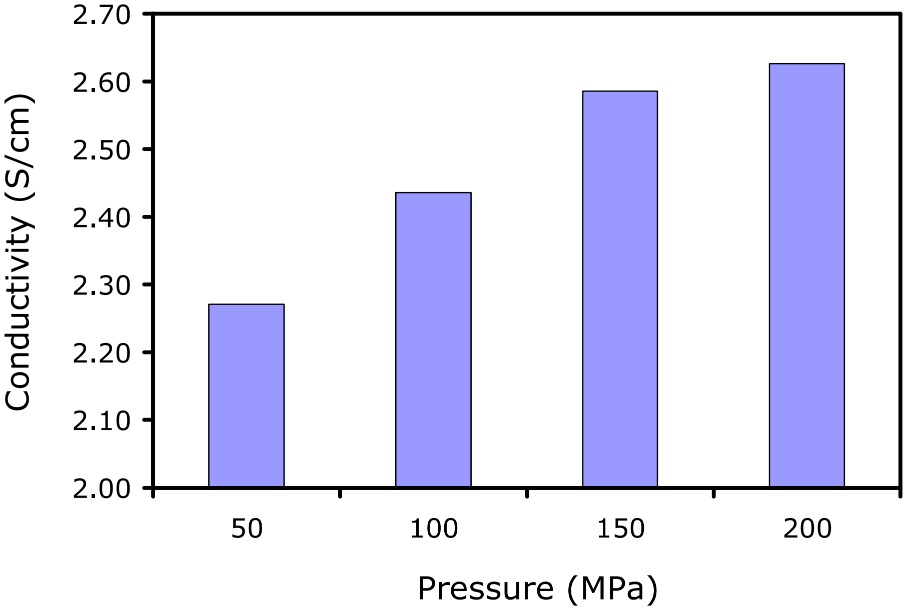

Figure 4.19. Electrical conductivity of un-sintered ITO Filler B nanoparticles as a function of pressure.

Figure 4.20b and Figure 4.20c show the fracture surfaces of nanocomposites containing 0.3 vol.% ITO that were formed with the lowest and highest compaction pressures (6.4 MPa and 51.3 MPa). Both fracture surfaces displayed in Figures 4.20b and 4.20c consist of randomly located faceted regions and smooth regions. The faceted regions appear lighter in color because the ITO nanoparticles are on the surface of the PMMA particles.[17, 21, 22] As described in section 4.1.1, the faceted regions occur due to crack propagation between the ITO-coated PMMA particles, and the smooth regions occur due to trans-particle fracture through the PMMA particles.

Figure 4.21a shows the ac conductivity as a function of frequency for PMMA-ITO nanocomposites filled with 1.3 vol.% ITO fabricated using 6.4, 25.6, and 51.3 MPa. For the composite formed with the highest pressure, 51.3 MPa, the conductivity still shows frequency dependence over the entire range. However, for nanocomposites formed with 6.4 MPa and 25.6 MPa, frequency-independent regions of the conductivity begin to emerge. The frequency at which the ac conductivity transitions from frequency-independent to frequency-dependent is typically referred to as the critical frequency, f_c. The critical frequency is located by finding the intersection of two tangent lines from the frequency-dependent and frequency-independent regions as shown in Figure 4.21a.[5, 21, 22] Frequency-independent behavior of the conductivity is usually indicative of interconnectivity between the conducting particles. The transition from frequency-dependent to frequency-independent conductivity will be discussed in more detail in section 4.3.2.

Figure 4.21b and Figure 4.21c show the fracture surfaces of nanocomposites containing 1.3 vol.% ITO that were formed with 6.4 MPa and 51.3 MPa, respectively. In

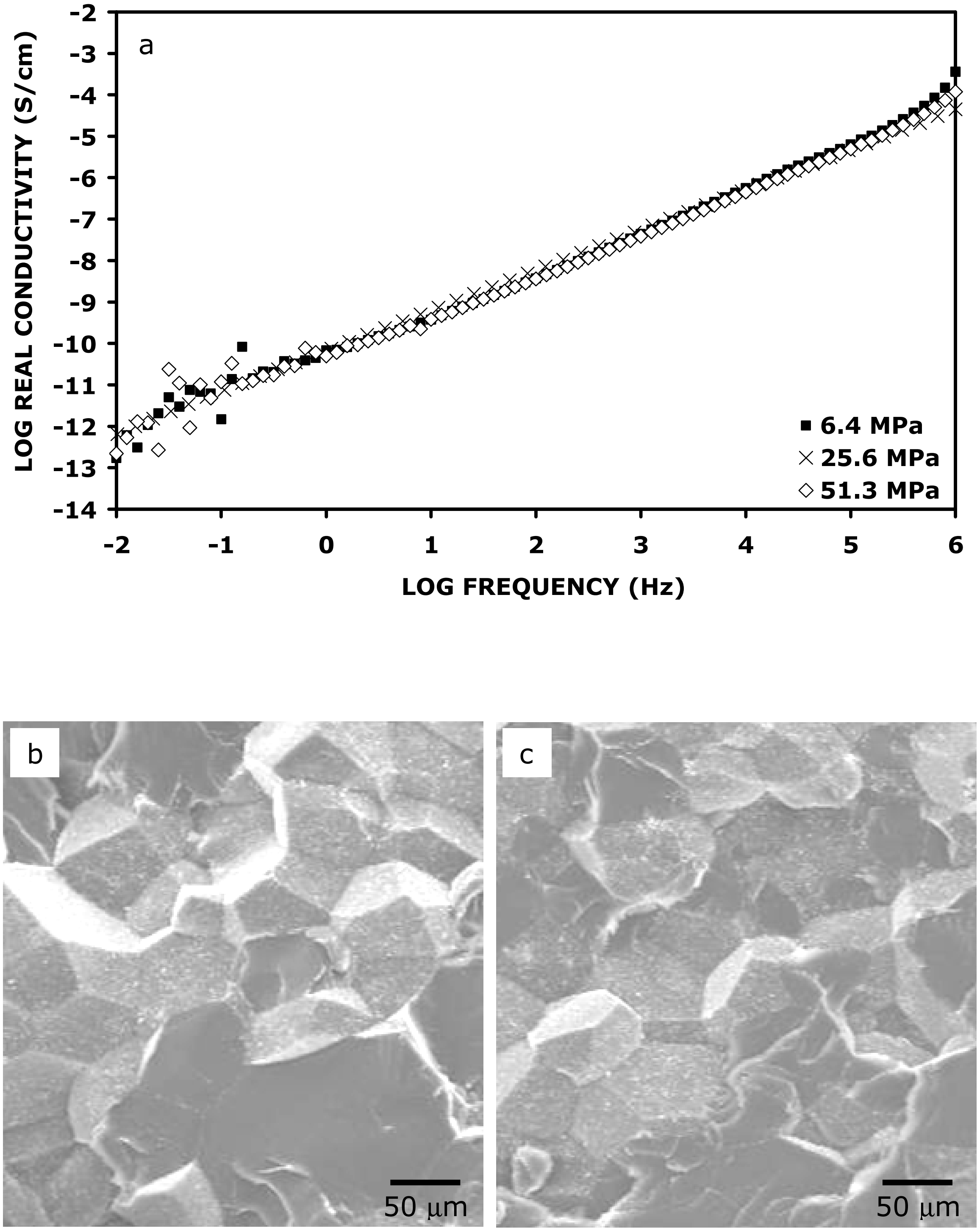

Figure 4.20. (a) The ac conductivity vs. frequency for PMMA-ITO nanocomposites filled with 0.3 vol.% ITO molded using 6.4 MPa, 25.6 MPa, and 51.3 MPa. Fracture surfaces of nanocomposites formed using (b) 6.4 MPa and (c) 51.3 MPa.[21]

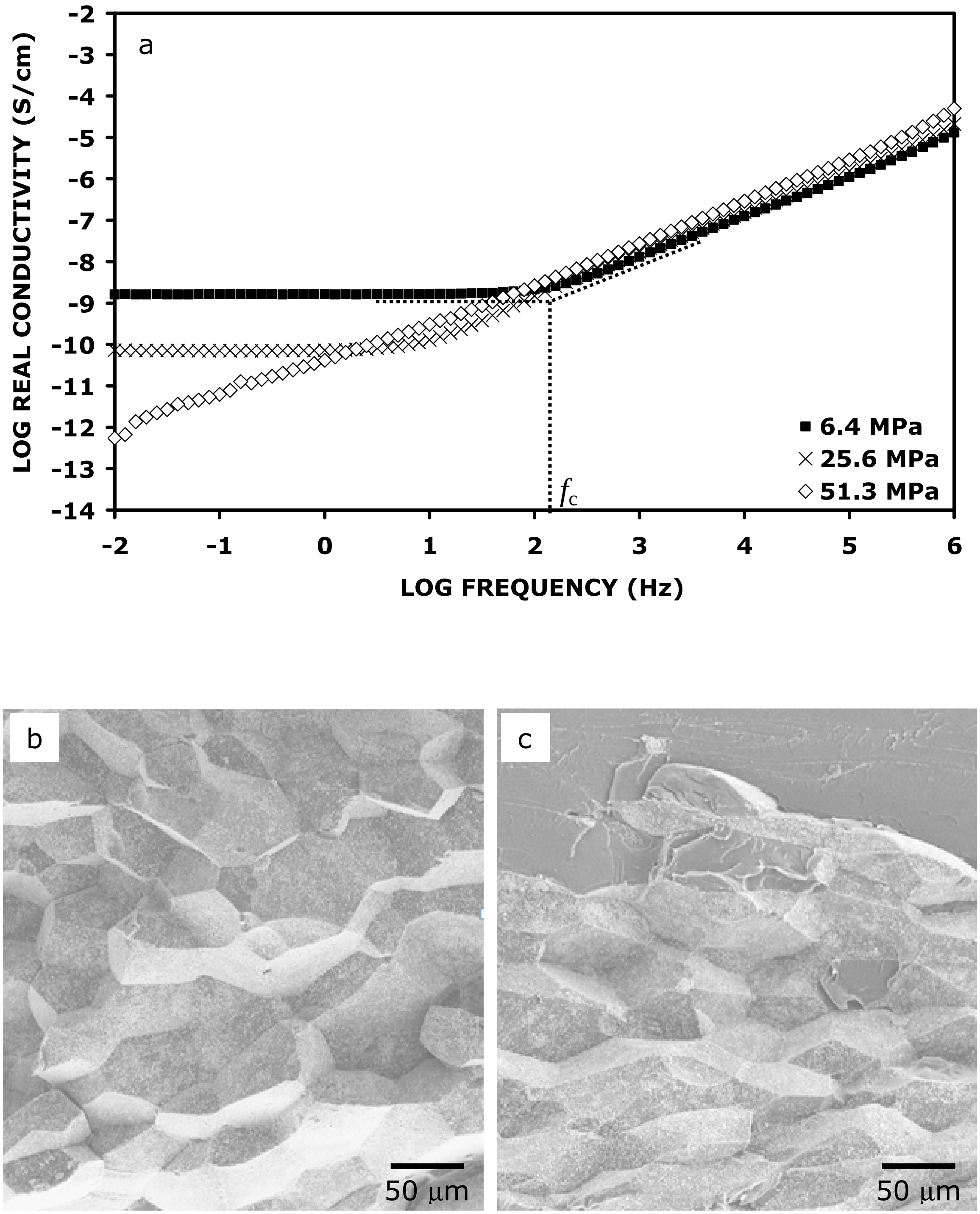

Figure 4.21. (a) The ac conductivity vs. frequency for PMMA-ITO nanocomposites filled with 1.3 vol.% ITO molded using 6.4 MPa, 25.6 MPa, and 51.3 MPa. Fracture surfaces of nanocomposites formed using (b) 6.4 MPa and (c) 51.3 MPa.[21]

the image of the nanocomposite formed with 6.4 MPa (Fig. 4.20b), the fracture surface is faceted over the entire cross-section, which indicates primarily inter-particle fracture between the ITO-coated PMMA particles. However, when the compaction pressure is increased to 51.3 MPa (Fig. 4.20c), trans-particle fracture of the PMMA particles is visible near the edge of the cross-section. Notably, the smooth fracture is located just below the surface of the nanocomposite, which is closest to the piston during compression molding. The fracture surface becomes faceted as crack propagation occurs towards the center of the cross-section. This transition from smooth to rough fracture may be explained by pressure gradients that occur during compression molding, and will be discussed in more detail in the discussion section.

Figure 4.22a shows the ac conductivity as a function of frequency for PMMA-ITO nanocomposites filled with 2.0 vol.% ITO made using 6.4, 25.6, and 51.3 MPa. The data shows that for this composition, frequency-independent regions of the conductivity exist for all applied compaction pressures. Similar to Figure 4.21a, the data shows that the frequency independent conductivity and the corresponding critical frequency increase when a lower compaction pressure is used. Figure 4.22b and Figure 4.22c show the fracture surfaces of nanocomposites containing 2.0 vol.% ITO that were formed with 6.4 MPa and 51.3 MPa, respectively. The cross-section of the nanocomposite formed with 6.4 MPa (Fig. 4.22b) is comparable to Fig. 4.21b in that the fracture surface is dominated by facets. For the nanocomposite filled with 2.0 vol.% ITO and formed with 51.3 MPa (Fig. 4.22c), trans-particle fracture is less apparent near the edge of the cross-section. Upon closer inspection, the PMMA particles in Figures 4.21c and 4.22c also appear to have undergone some flattening under these conditions. These attributes are likely due to

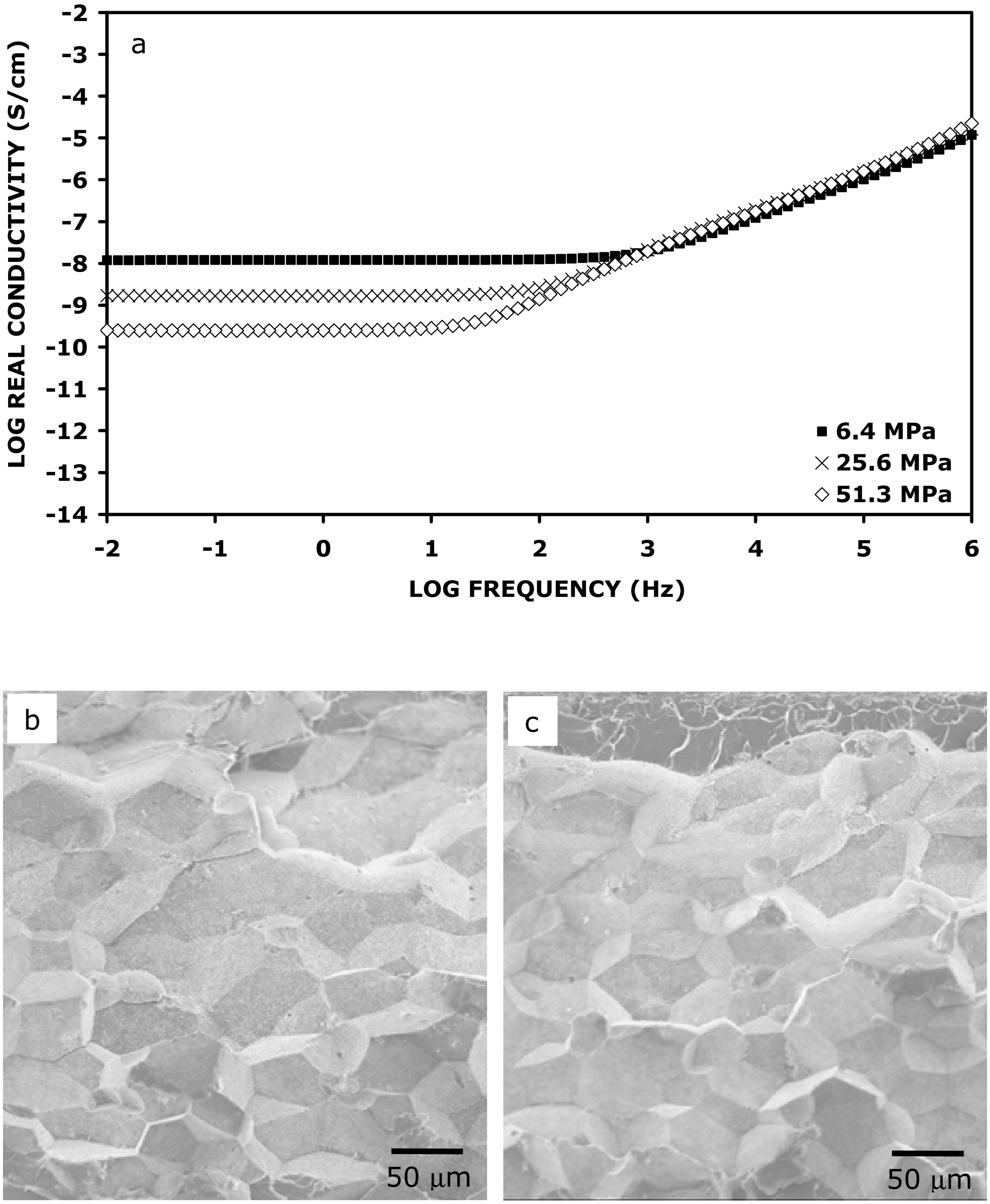

Figure 4.22. (a) The ac conductivity vs. frequency for PMMA-ITO nanocomposites filled with 2.0 vol.% ITO molded using 6.4 MPa, 25.6 MPa, and 51.3 MPa. Fracture surfaces of nanocomposites formed using (b) 6.4 MPa and (c) 51.3 MPa.[21]

the combined effects of the pressure transmitted during compaction and an increase in the rigidity of the nanocomposites with the addition of more ITO nanoparticles.

Figure 4.23 summarizes the steady-state (dc) conductivity as a function of ITO content for PMMA-ITO nanocomposites formed using 6.4, 25.6, and 51.3 MPa. The dc conductivities were calculated from the impedance spectra as described in section 3.7. The error bars include data from at least three different specimens fabricated under the same conditions. The wide PMMA particle size distribution and the compaction rate are likely responsible for some of the larger standard deviations seen in the data. Control of the compaction rate was limited since it could only be adjusted manually by a knob on the control panel of the mounting press. In spite of these limitations, there is a detectable effect of the compaction pressure on the percolation threshold and resultant dc conductivity.

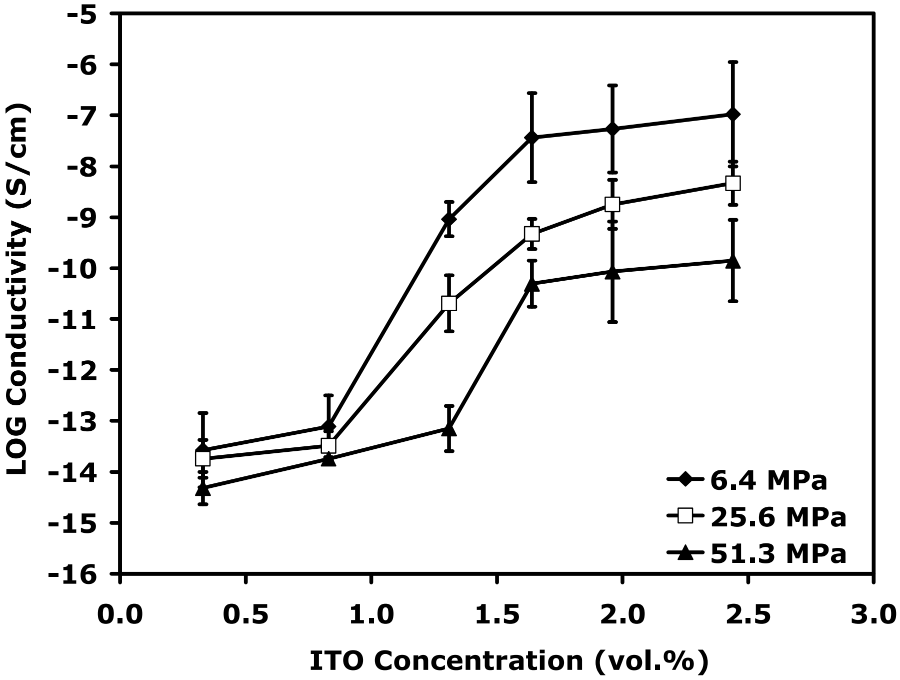

Figure 4.23. The dc conductivity vs. ITO concentration for PMMA-ITO nanocomposites molded using three different compaction pressures.

Figure 4.23 indicates that higher compaction pressure generally results in lower conductivity especially for PMMA-ITO nanocomposites with concentrations above the percolation threshold. For samples with the highest ITO content, the conductivity decreases by over two orders of magnitude when the applied compaction pressure is raised from 6.4 MPa to 51.3 MPa. The graph also shows that when 6.4 MPa and 25.6 MPa are used, the specimens require about 0.8 vol.% ITO to achieve percolation. For specimens fabricated using 51.3 MPa, over 1.5 vol.% ITO was necessary to attain percolation.

The effect of sample thickness was determined by varying the amount of powder used to make the nanocomposites. Figure 4.24 displays the ac conductivity as a function of frequency for PMMA-ITO nanocomposites containing 2.4 vol.% ITO made using 2.0 g and 0.275 g of ITO-coated PMMA particles with different compaction pressures. When the nanocomposites are fabricated using 0.275 g of powder and 51.3 MPa, the conductivity shows frequency dependence over the entire range. For nanocomposites formed with 0.275 g, a transition to frequency-independent conductivity emerges when the compaction pressure is reduced to 25.6 MPa. This is similar to the trend presented in Figure 4.21a. When the amount of powder used to make the nanocomposites is increased to 2.0 g, the samples exhibit frequency-independent conductivity nearly over the entire frequency range. Figure 4.24 also indicates that the electrical behavior of the thicker nanocomposites is not significantly affected by the change in compaction pressure used during the fabrication process.

Figure 4.25 shows the fracture surfaces for PMMA-ITO nanocomposites containing 2.4 vol.% ITO made using 2.0 g and 0.275 g and compaction pressures of 6.4

MPa or 51.3 MPa. The SEM images of nanocomposites formed with 2.0 g of ITO-coated PMMA powders (Fig. 4.25a-b) indicate that the compaction pressure does not have a significant effect on the microstructure of these samples, as already suggested by the electrical conductivity results. In both cases, inter-particle fracture occurs over the entire cross-section of the nanocomposites, and the ITO is visible on the surfaces of all of the deformed PMMA particles. However, when 6.4 MPa is used to mold nanocomposites with 0.275 g of ITO-coated PMMA powder, Figure 4.25c shows that the fracture surface exhibits random smooth and faceted regions. When the compaction pressure is increased to 51.3 MPa for a nanocomposite made with 0.275 g powder, the image (Fig. 4.25d) displays smooth regions and trans-particle fracture nearly over the entire cross-section. These observations of the microstructures may be explained by pressure gradients, which are dependent on the amount of powder that is being compacted.

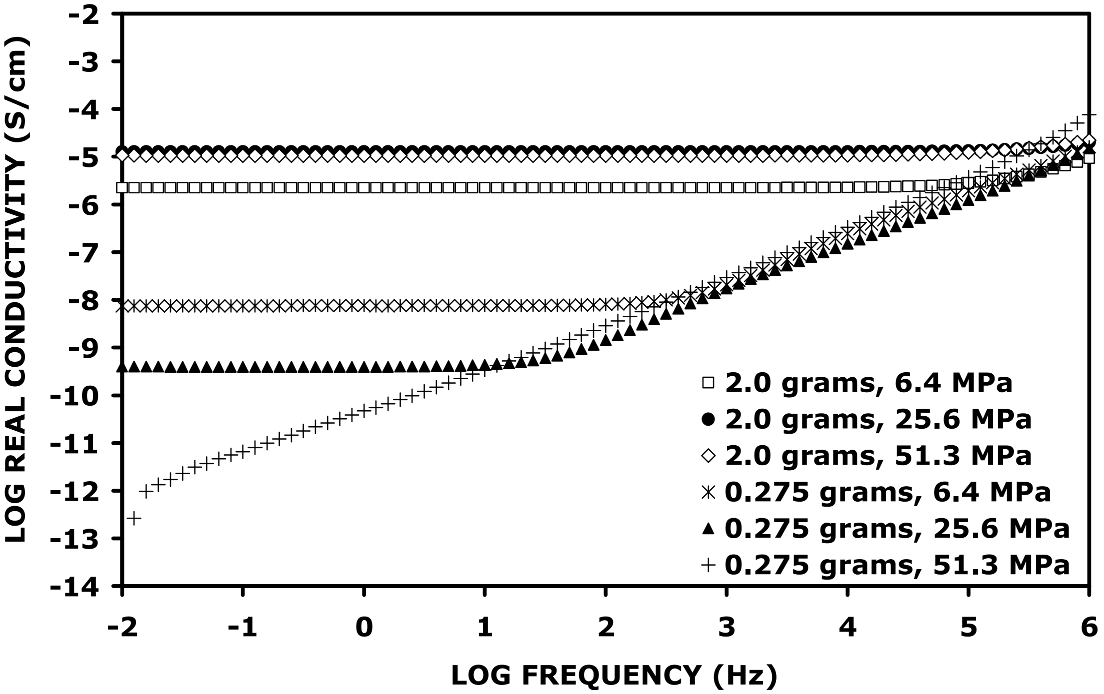

Figure 4.24. The ac conductivity vs. frequency for PMMA-ITO nanocomposites with 2.4 vol.% ITO formed with different amounts of powder and compaction pressures.[21]

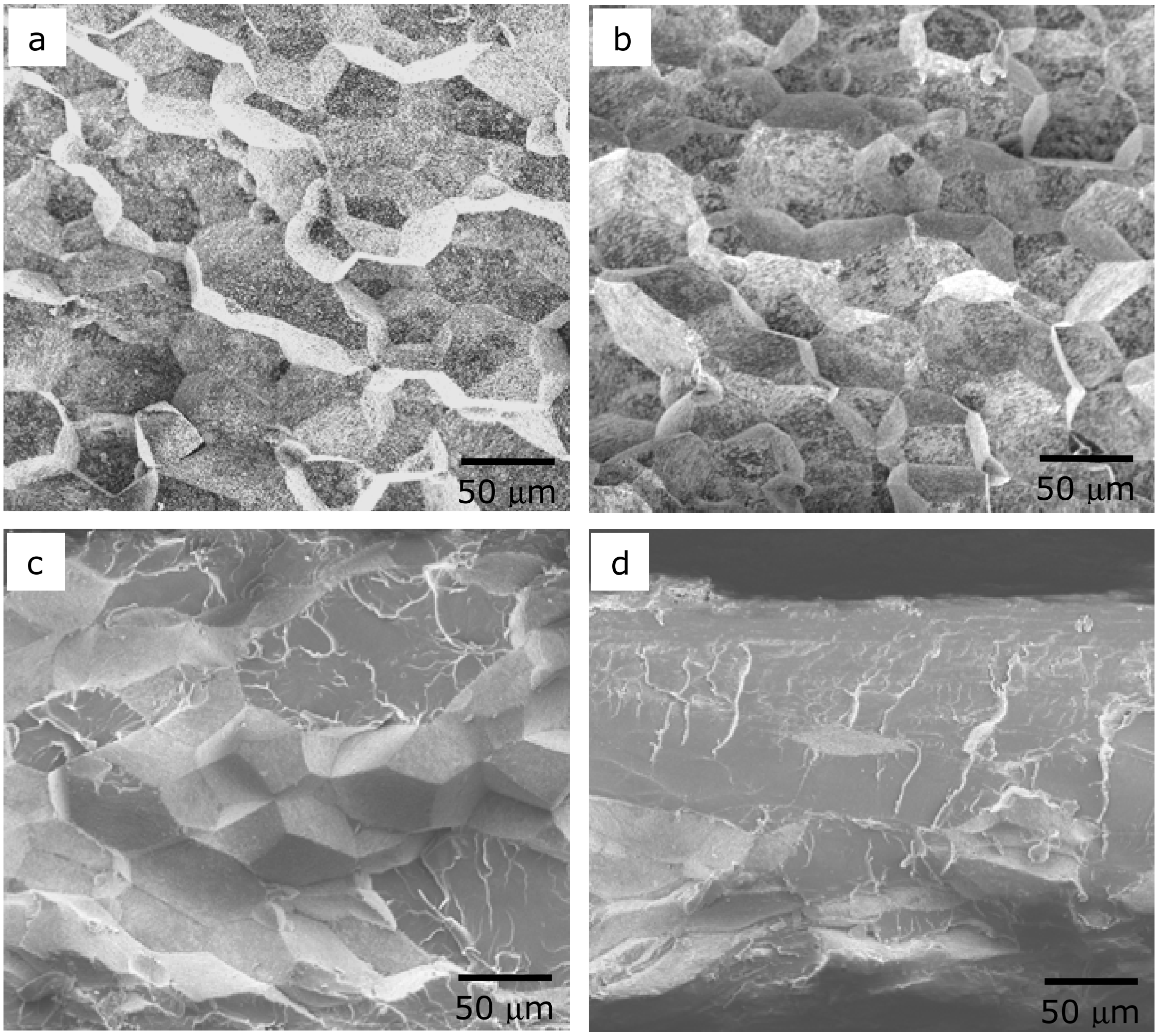

Figure 4.25. Fracture surfaces of PMMA-ITO nanocomposites (2.4 vol.% ITO) formed with different amounts of powder and compaction pressures. (a) 2.0 g, 6.4 MPa; (b) 2.0 g, 51.3 MPa; (c) 0.275 g, 6.4 MPa; and (d) 0.275 g, 51.3 MPa.[21]

Figure 4.26 summarizes the dc conductivity results as a function of the amount of powder used to compression mold nanocomposites filled with 2.4 vol.% ITO at different compaction pressures. The graph shows that as the quantity of powder that was used to form the nanocomposites is increased, the compaction pressure plays less of a role in determining the conductivity of the specimens. On the other hand, the compaction pressure has a significant effect on the resultant conductivity when the amount of powder used to make the nanocomposites is below 1.0 g. The electrical properties exhibited by the nanocomposites are naturally related to the microstructures shown in Figure 4.25. The behavior of compacted powders as a function of quantity will be further described in section 4.3.2.

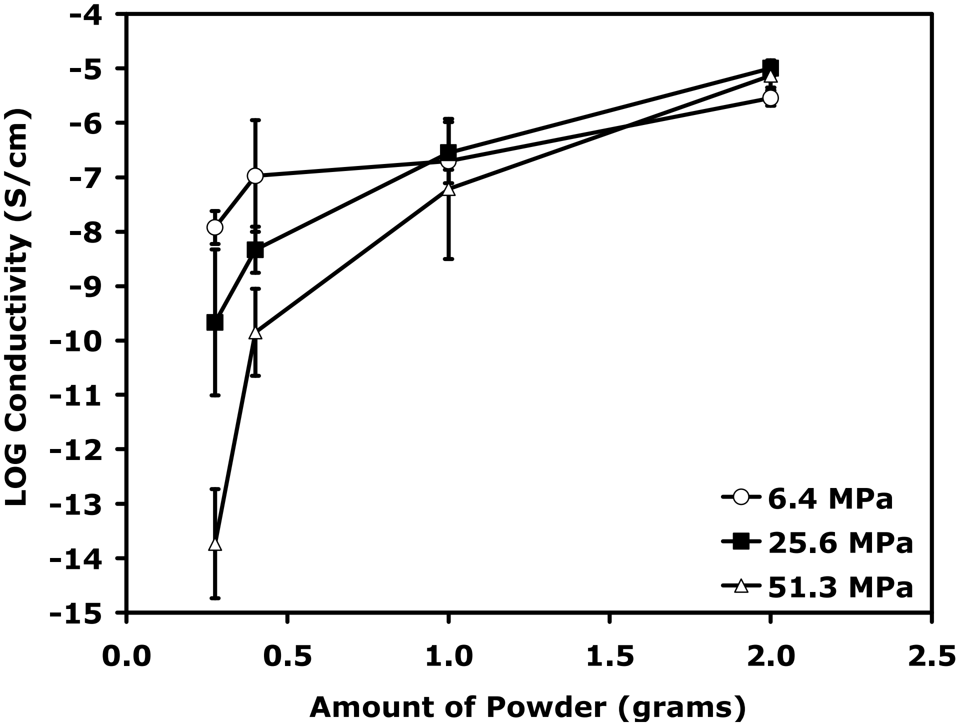

Figure 4.26. The dc conductivity vs. amount of powder used to form PMMA-ITO nanocomposites with 2.4 vol.% ITO. The graph shows data for the three different compaction pressures.[21]

4.3.2 Analysis and Discussion

It is difficult to deduce any effect of the compaction pressure on nanocomposites that contain ITO concentrations below the percolation threshold (<1.3 vol.% ITO) because they are very insulating. For PMMA-ITO nanocomposites filled with 0.3 vol.% ITO, the electrical data and microstructure are indistinguishable when different compaction pressures are used (Fig. 4.20). This is because the ITO nanoparticles cannot form continuous chains at low concentrations in the matrix. Consequently, this causes most of the cross-section to exhibit trans-particle fracture and very high electrical resistance.

In PMMA-ITO nanocomposites having ITO concentrations above the percolation threshold (>1.3 vol.% ITO), the electrical properties and microstructure are more sensitive to variations in the compaction pressure. This is shown in Figs. 4.21 and 4.22, where increasing the compaction pressure dramatically alters the ac conductivity in the composites. Changes in the microstructure can also be recognized in the SEM images of the microstructures. The crack propagation behavior in the cross-sections was observed for several nanocomposites fabricated under identical conditions. The nanocomposites were fractured at room temperature in order to avoid polymer flow and deformation artifacts. The trans-particle fracture at the edges of the nanocomposites can be explained by a pressure gradient transmitted through the powder during composite fabrication. The pressure transmitted during compression molding may be described by the following equation:

$$P_x/P = \exp\,[-4uzH/D] \qquad (3)$$

where P is the applied pressure, P_x is the pressure at any position x below the punch, u is the coefficient of friction between the powder and the die wall, z is a proportionality factor that represents the ratio of radial stress and axial stress, and H and D are the height of the powder bed and diameter of the punch, respectively.[91] This expression is applicable to single action pressing, which was used in the fabrication of the nanocomposites. The height of the powder bed is proportional to the amount of powder used to form the nanocomposites. Therefore, Equation 3 indicates that the ratio of the amount of powder used to make the nanocomposites to the diameter of the die affects the pressure transmitted during the compaction process.

For nanocomposites with ITO concentrations above the percolation threshold (>1.3 vol.% ITO) that were made with 0.4 g of powder, there is sufficient pressure near the edge of the cross-section to force the ITO into the polymer phase and cause trans-particle fracture (Figs. 4.21c and 4.22c). However, since less pressure is transmitted towards the middle of the cross-section, inter-particle fracture occurs, and a faceted surface appears in the middle because the ITO remains on the surface of the PMMA particles. Figure 4.27 illustrates a schematic of the fracture surface of the PMMA-ITO nanocomposites as a consequence of the pressure distribution described by Equation 3.

The SEM images of the cross-sections of nanocomposites made with different amounts of powder (Fig. 4.25) further show the effect of the starting amount of powder, and hence the H/D ratio. For nanocomposites having 2.4 vol.% ITO that were formed with 0.275 g, trans-particle fracture occurs even when the lowest compaction pressure of 6.4 MPa is used (Fig. 4.25c). The nanocomposite formed with 0.275 g of powder and a compaction pressure 51.3 MPa exhibits trans-particle fracture nearly over the entire

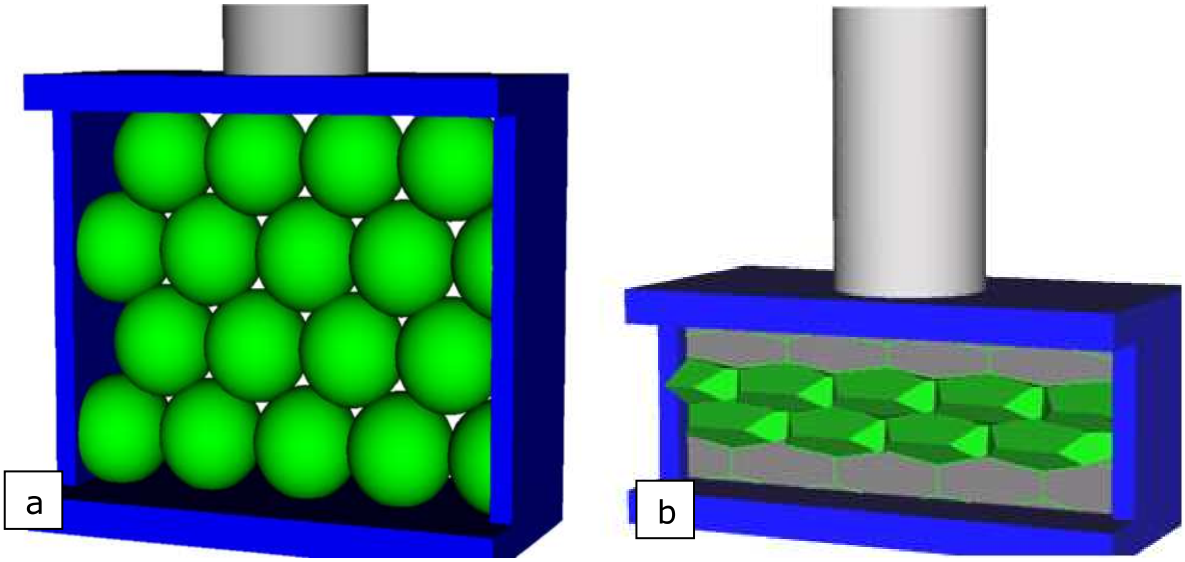

Figure 4.27. Schematic of proposed microstructure of PMMA-ITO nanocomposites when excessive pressure is applied during composite fabrication. (a) Starting ITO-coated PMMA particles; (b) cross-section of microstructure after compression molding.

fracture surface (Fig. 4.25d), indicating that the pressure is more uniformly distributed over the microstructure during compaction as a result of decreasing the H/D ratio. This result is consistent with the expression shown in Equation 3. However, when the amount of powder used to make the PMMA-ITO nanocomposites is increased to 2.0 g (Figs. 4.25a-b), the amount of pressure transmitted is not sufficient to cause the ITO to penetrate to PMMA and thus inter-particle fracture occurs across the whole specimen cross-section.

As discussed earlier, when higher compaction pressures are used and/or the H/D ratio is low, the ITO does not remain on the surface of the polymer phase and coalescence of the polymer particles can occur. This causes the ITO nanoparticles to become electrically isolated by the insulating nature of the polymer. This is demonstrated in the dc conductivity for the PMMA-ITO nanocomposites (Fig. 4.23), which shows that additional ITO is necessary in order to achieve percolation and increase the conductivity of the nanocomposites when high compaction pressures are used.

Limiting the compaction pressure and using larger amounts of powder (and consequently a higher H/D ratio) results in an increase of the conductivity for the PMMA-ITO nanocomposites (Fig. 4.26). This is because increasing the amount of powder used to form the nanocomposites reduces the pressure transmitted through the microstructure during the fabrication process (Eq. 3),[91] which prevents penetration of the ITO into the PMMA. However, it should be noted that there is a minimum pressure necessary to obtain sufficient nanocomposite density in order to promote good contact between the conducting particles and adequate mechanical integrity of the microstructure.

The conductivity of the nanocomposites formed with 2.0 g and 0.275 g can be directly related to the features in the corresponding SEM images (Fig. 4.25). The data suggests that nanocomposites with more facets along the fracture surface possess higher conductivity. The facets occur due to inter-particle fracture caused by an appreciable amount of ITO located at the interfaces between the PMMA particles. Therefore, when more ITO remains segregated in the microstructure, this increases the number of possible ITO conducting paths and enhances the conductivity of the nanocomposites.

More information about the microstructure of the PMMA-ITO nanocomposite is revealed by examining the frequency dependence of the ac conductivity. The ac conductivity can be used to characterize the regions dominated by the resistive and capacitive regions of the microstructure. When there is an insufficient amount of ITO to form an interconnected network in the PMMA matrix, the nanocomposites exhibit frequency-dependent conductivity, $\sigma(\omega)$, according to the power law:

$$\sigma(\omega) \propto \omega^x \tag{4}$$

where ω is the angular frequency, and the exponent is related to the fraction of virtual capacitors that exist in the system.[92] The angular frequency is equal to $2\pi f$, where f is the frequency in Hertz (cycles/sec). This is because the aggregates of ITO in the microstructure are separated by insulating barriers of void space and/or PMMA. This arrangement of ITO may be considered as a variety of capacitive regions in the microstructure of the nanocomposites. The admittance of an insulating capacitive process may be mathematically described by:

$$Y^* = j\omega C \tag{5}$$

where Y^* is the admittance (conductance as a function of frequency), and C is the capacitance.[80] Equation 5 shows that the conductivity ($\sigma \propto Y^*$) is a function of frequency when capacitive behavior is dominant. As a result, the ac conductivity of the nanocomposites is highly dependent on frequency when there is not physical contact between the ITO particles in the matrix.

When percolation is achieved in the nanocomposites and continuous chains of ITO nanoparticles are formed in the matrix, a frequency-independent region emerges in the ac conductivity of the nanocomposites (Figs. 4.21a, 4.22a, 4.24). These continuous chains of ITO nanoparticles may be interpreted as a network of resistors, where each resistor represents one contact between two particles.[93] The conductivity becomes less dependent on the frequency, which is expressed by the following equation:

$$Y^* = 1/R + j\omega C \tag{6}$$

where R is the resistance.[80] The resistance, R, is primarily a function of the contact zone between the ITO particles and their intrinsic electrical properties.

As more ITO exists at the interfaces of the PMMA, and the ITO interconnected network expands, the conductivity of the nanocomposites naturally increases. The data shows that this causes the frequency-independent region of the ac conductivity to grow and the frequency-dependent region to decrease in size (Figs. 4.21a, 4.22a, 4.24). As the frequency-dependent region becomes smaller, the transition to frequency-independent conductivity occurs at higher frequencies. As mentioned in the results section, the frequency at which this transition happens is known as the critical frequency, f_c. (see point marked f_c in Fig. 4.21a). Connor *et al.* has proposed that the critical frequency is associated with the fractal dimension of the aggregates of the filler in the matrix.[94] An empirical relation between the critical frequency and fractal dimension is as follows:

$$f_c \propto |p-p_c|^{\gamma} \tag{7}$$

where p represents the volume fraction of filler at a given composition, p_c represents the volume fraction of filler that is necessary for percolation, and γ represents a value related to the fractal dimension of the conducting volume (according to Connor *et al.*).[94]

Figure 4.28 shows the critical frequency as a function of $|p-p_c|$ plotted in a log-scale for PMMA-ITO nanocomposites formed with 0.4 g of powder. For nanocomposites fabricated with 6.4 MPa, 25.6 MPa, and 51.3 MPa, a linear fit was obtained and values of 0.28, 0.44, and 1.11 were observed for γ, respectively. For this particular experiment, and in contrast to Connor *et al.*, it is proposed that the increasing γ values represent greater complexity in the spatial distribution of the filler in the microstructure. In other words, the scale of complexity is considered to be simplest for the case where the ITO exists primarily on the surfaces of the PMMA particles (resulting in complete inter-particle fracture in the cross-section); and highest when the ITO is distributed both within the

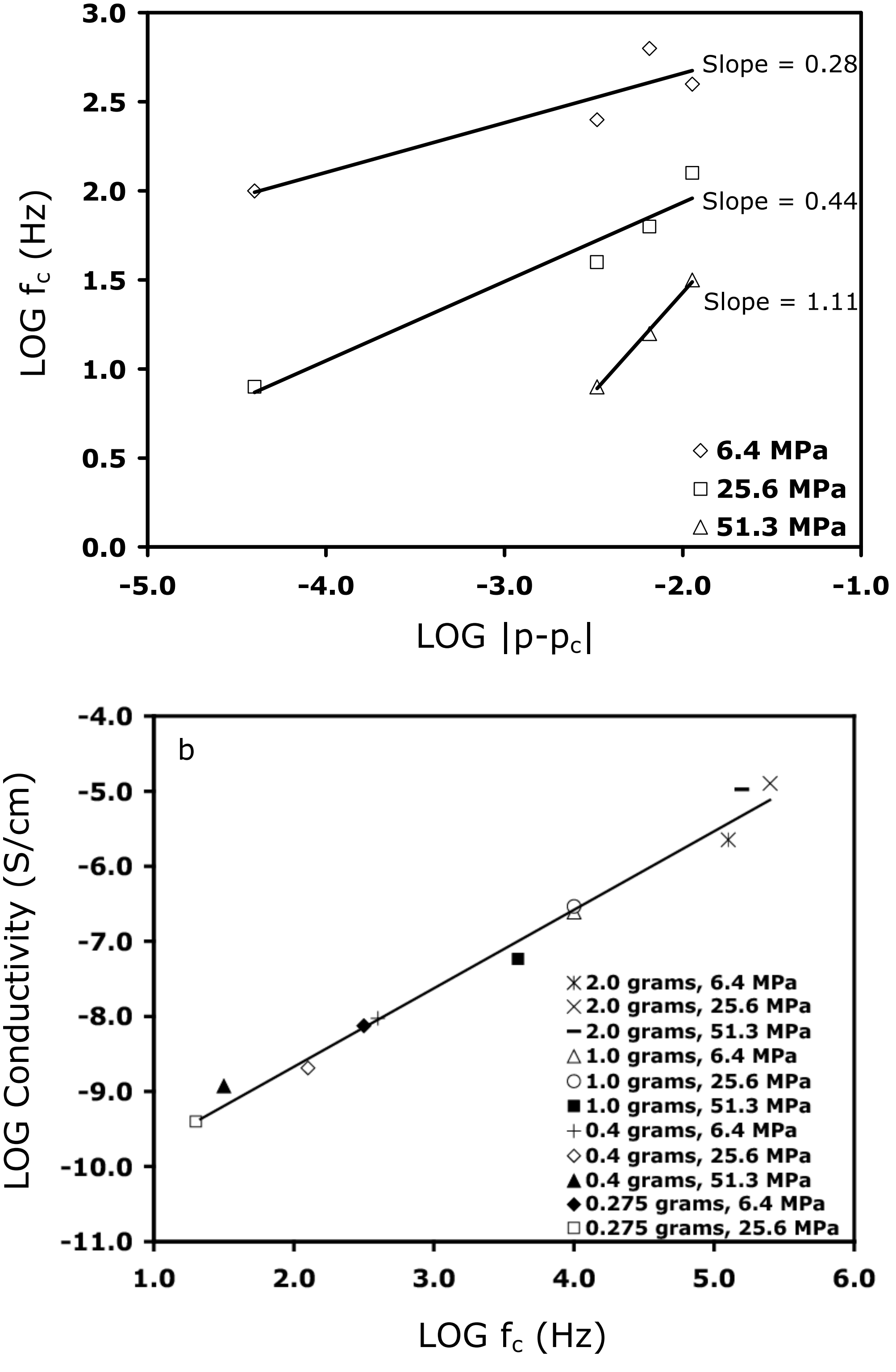

Figure 4.28. (a) Critical frequency f_c as a function of $|p-p_c|$ for PMMA-ITO composites formed with 0.4 g of powder and different compaction pressures, (p_c=0.013); (b) dc conductivity vs. critical frequency for PMMA-ITO composites with 2.4 vol.% ITO formed with various amounts of powder and compaction pressures.[21]

PMMA particles and on the surface of the PMMA particles (resulting in a combination of inter-particle fracture and trans-particle fracture). Based on this interpretation, the data in Figure 4.28a indicates that the PMMA-ITO nanocomposites formed with 51.3 MPa have a more complex microstructure than the nanocomposites formed with lower compaction pressures. This is in agreement with the SEM images of the cross-sections (Figs. 4.20, 4.21, 4.22, 4.25), which exhibit more complexity in the microstructures (i.e., combinations of smooth and faceted fracture surfaces) when the highest compaction pressure is used.

Figure 4.28b introduces an entirely new relationship based on the critical frequency. Figure 4.28b presents the dependence of the dc conductivity on the critical frequency of the PMMA-ITO nanocomposites that contain 2.4 vol.% ITO and were formed with various amounts of powder and compaction pressures. This data shows that as the critical frequency increases (when more continuous ITO chains are formed in the microstructure), the overall conductivity of the nanocomposites increases. A linear relationship, having a slope of 1.06, is observed between the dc conductivity and the critical frequency for the PMMA-ITO nanocomposites. Consequently, it is difficult to assign meaning to this value of the slope since this relationship has not been presented in the literature before.

Figure 4.28b demonstrates the critical role that the microstructure plays in the electrical conductivity and interconnectivity of the filler in polymer-matrix composites. For specimens having the same concentration of ITO (2.4 vol.%), the dc conductivity is improved by over four orders of magnitude when the fabrication parameters are modified to promote interconnectivity between the ITO nanoparticles. Figures 4.28a-b quantitatively show that when the fabrication conditions yield a “simplified system” of resistive and capacitive regions (high segregation between the PMMA and ITO) in the microstructure, the better electrical conductivity in these types of nanocomposites can be achieved.

4.3.3 Conclusions

Correlations were established in order to better understand the effect of the fabrication conditions on the interconnectivity of the ITO nanoparticles in the PMMA-ITO nanocomposites. The data collected for the PMMA-ITO nanocomposites in this study showed that the ac conductivity is dependent on the microstructure of the nanocomposites, and that the microstructure is sensitive to the compaction pressure and amount of powder used to form the nanocomposites. Limiting the compaction pressure used to the fabricate the PMMA-ITO nanocomposites played a key role in preserving the segregation between the ITO and PMMA particles in the nanocomposites and preventing the ITO nanoparticles from penetrating the surfaces of the PMMA particles. The data also showed that the pressure transmitted through the microstructure during compression molding can be controlled and reduced by increasing the quantity of powder used to form the PMMA-ITO nanocomposites.

Preservation of the segregation between the ITO and PMMA was accompanied by expansion of the frequency-independent region in the ac conductivity spectra, and an increase in the measured critical frequency and dc conductivity. Examination of the relationship between the critical frequency, ITO concentration, and dc conductivity provided insight through quantitative means in predicting when the ITO nanoparticles are located at the interfaces of the PMMA phase or beneath the surface the PMMA particles.

For example, when $\gamma \leq 0.4$, where $f_c \propto |p-p_c|^{\gamma}$, good segregation was observed between the ITO and the PMMA particles, resulting in primarily inter-particle fracture between the PMMA particles, and higher electrical conductivity in the specimens.

4.4 Correlation of the Electrical and Optical Properties with the Microstructure of Thick PMMA-ITO Nanocomposites[22]

4.4.1 Characterization of Results

In this section, the ITO concentration was varied in order to study the effect on the microstructure, electrical and optical properties of the PMMA-ITO nanocomposites. For this set of specimens, ITO Filler A was used as the filler material. The details of the fabrication conditions for Set IV are described in Table 3.2 on page 30. Transmission optical microscopy, SEM images, impedance spectroscopy, and analysis of the internal reflection intensity were used to characterize the nanocomposites. The objective was to correlate the variations in the microstructure to the electrical response and complex refractive index measured in-plane and through-plane in the specimens.

4.4.1.1 Microstructural Evaluation

Figure 4.29 shows transmission optical micrographs and SEM cross-section images for composites containing 0.17, 0.83, and 1.64 vol.% ITO. Although the transmission optical micrographs (Figs. 4.29a, 4.29c, 4.29e) display almost identical features for samples with compositions 0.17, 0.83, and 1.64 vol.% ITO due to the thickness of the specimens, the SEM images reveal preferential displacement of the ITO nanoparticles as a function of their concentration, similar to the nanocomposites described in Sets I and II. Figure 4.29b shows that for samples in Set IV with low ITO

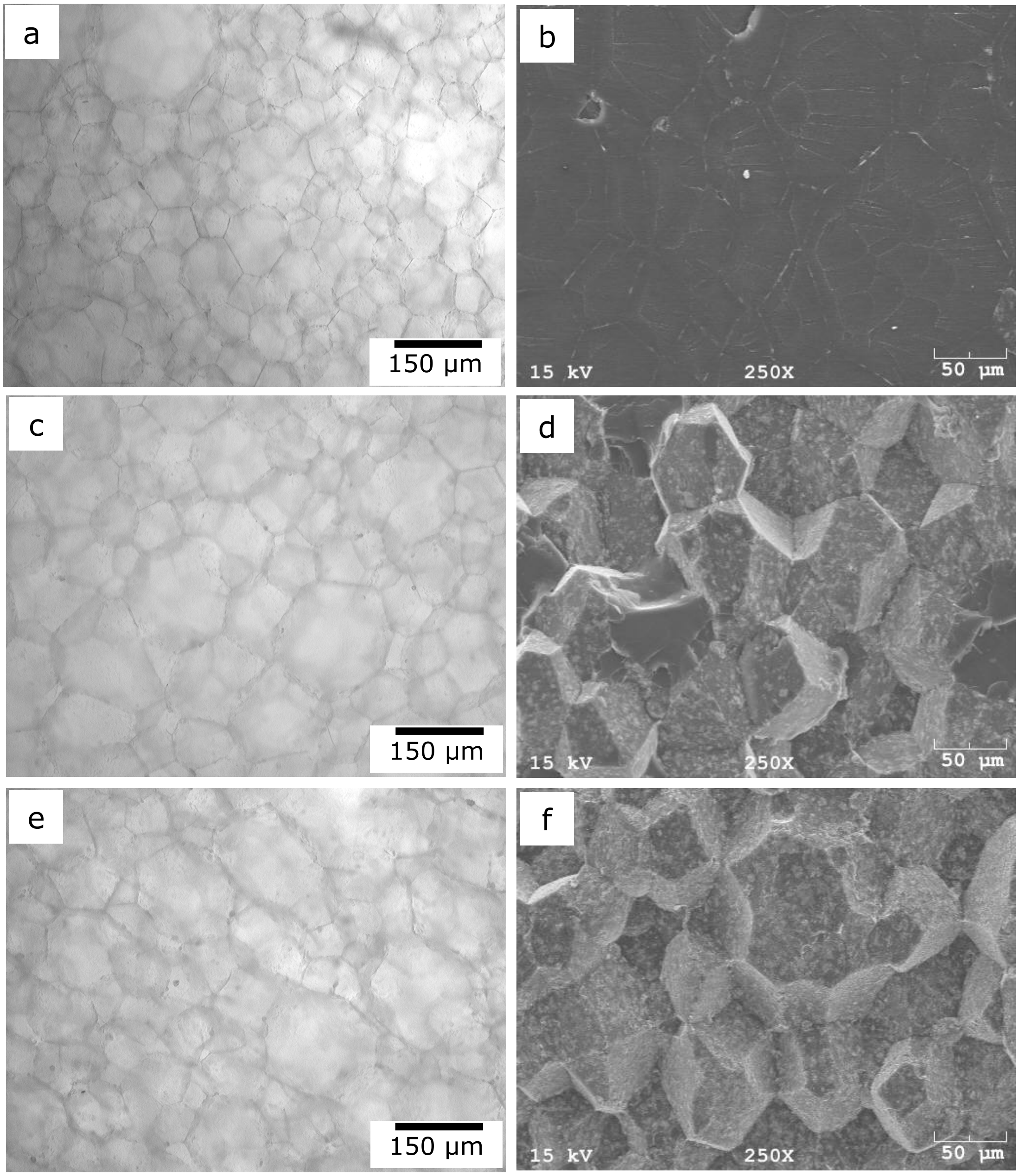

Figure 4.29. Transmission optical micrographs and fractured SEM cross-section images for PMMA-ITO nanocomposites with various ITO concentrations. (a) optical image of composite with 0.17 vol.% ITO; (b) SEM image of composite with 0.17 vol.% ITO; (c) optical image of composite with 0.83 vol.% ITO; (d) SEM image of composite with 0.83 vol.% ITO; (e) optical image of composite with 1.64 vol.% ITO; (f) SEM image of composite with 1.64 vol.% ITO.[22]

concentrations, the ITO nanoparticles are concentrated along the edges of the PMMA particles. As a result, trans-particle fracture occurs upon mechanical failure of the PMMA-ITO nanocomposites.

Figure 4.29d shows that the ITO nanoparticles begin to appear on the flat surfaces of the PMMA after the concentration is increased to 0.83 vol.% ITO. Again, inter-particle fracture occurs more readily since there is weaker bonding between the PMMA particles due to the ITO covering the surfaces. When the ITO concentration is increased to 1.64 vol.% ITO, Figure 4.29f shows that more ITO nanoparticles are located on the surfaces of the PMMA, and that inter-particle fracture occurs over the entire cross-section of the composite. The SEM images indicate that the PMMA particles remain isotropic despite the high ITO concentration.

4.4.1.2 Electrical Properties Results

Figure 4.30 displays complex plane impedance plots for the PMMA-ITO nanocomposites. In Fig. 4.30a, the data markers, which form a small arc, represent the experimental data of a composite with 0.17 vol.% ITO. The solid line is the curve fitted to the equivalent circuit (resistor in parallel with a CPE) in order to estimate the impedance of the specimen. Fig. 4.30b shows a higher magnification of the origin of the plot in Fig. 4.30a to reveal smaller semicircles for the more conducting specimens, specifically composites with 0.50, 0.74, 0.83 vol.% ITO. For samples where a complete semicircle was obtained, the semicircles all appear to have large depression angle. It is speculated that this is due to the complex impedance data being comprised of two overlapping semi-circles. Fig. 4.30c shows that when the ITO concentration is increased above 1.31 vol.% ITO in the composites, additional semicircles become more apparent.

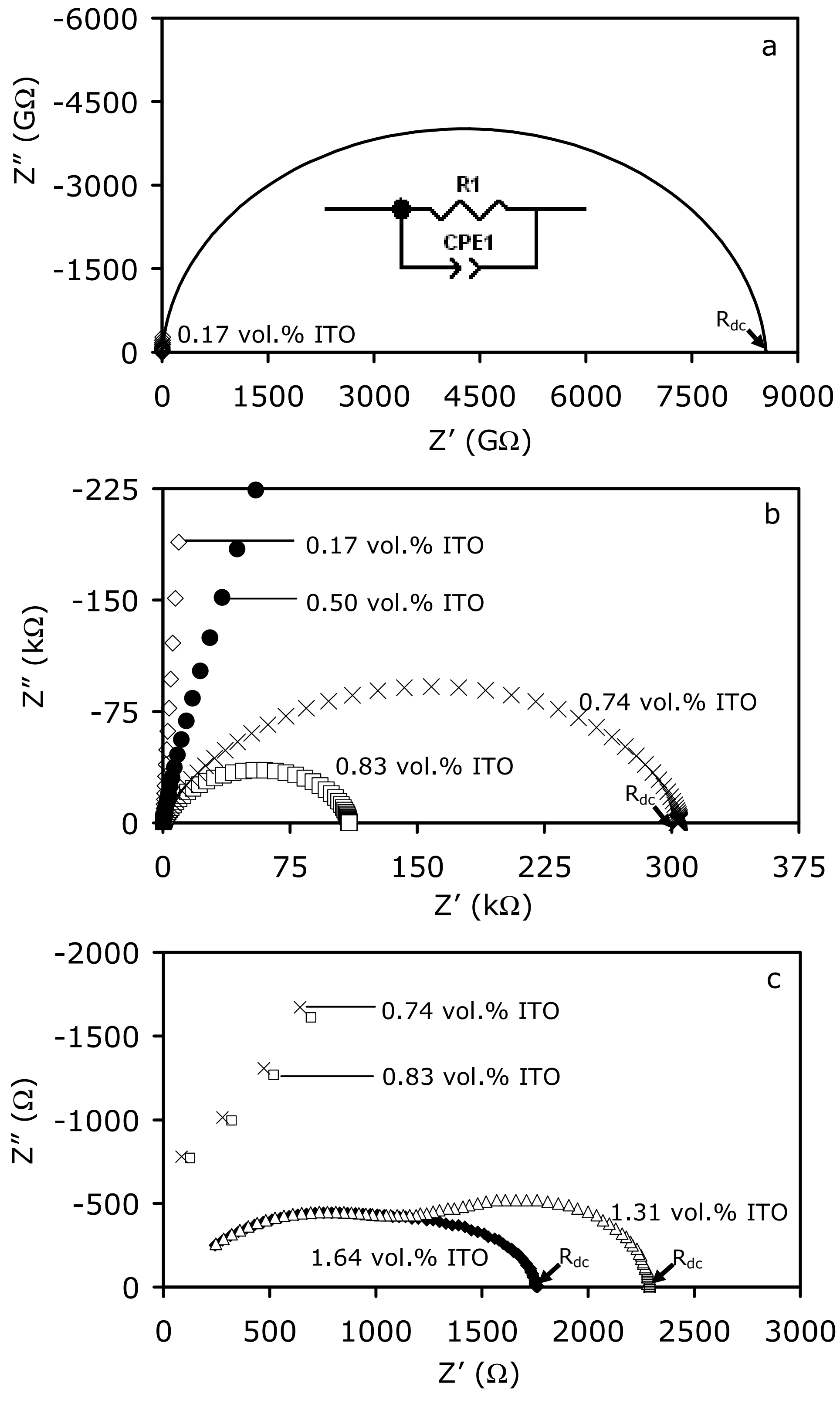

Figure 4.30. Complex plane impedance plots of PMMA-ITO nanocomposites. Parts a-c are different magnifications of the origin of the same figure.[22]

Figure 4.31 shows the dc conductivity of the PMMA-ITO nanocomposites as a function of ITO content. The error bars include measured data from at least three different specimens fabricated under the same exact conditions. Between 0.30-0.80 vol.% ITO, there is an increase in the conductivity by approximately seven orders of magnitude. For ITO concentrations greater than 0.80 vol.% ITO, Figure 4.31 displays a monotonic increase in conductivity. This behavior after the percolation threshold is different from the observations in Set II (Fig. 4.17, page 64). The dc electrical measurements for the PMMA-ITO nanocomposites in Set II revealed an intermediate plateau region after percolation.

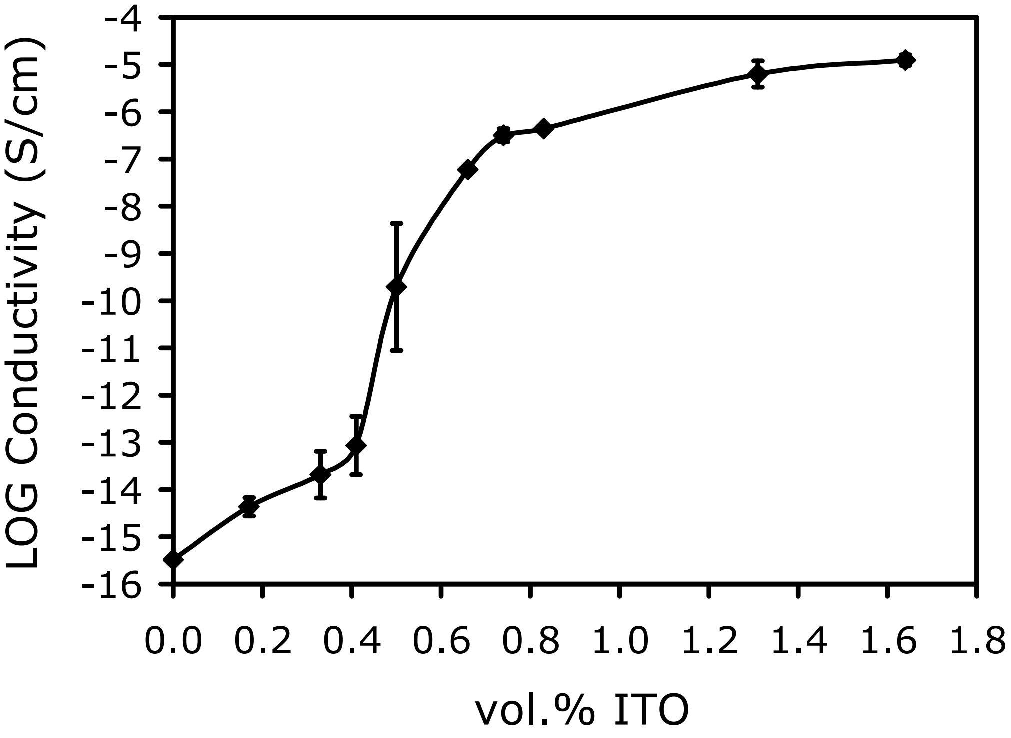

Figure 4.31. Electrical conductivity of PMMA-ITO nanocomposites as a function of ITO content.[22]

Figure 4.32 shows the real part of the conductivity as a function of frequency for the PMMA-ITO nanocomposites. For composites with ITO concentrations lower than

0.50 vol.% ITO, the ac conductivity increases with increasing frequency over the entire frequency range. As the ITO content and the conductivity of the composites increases, the ac conductivity begins to show frequency-independent behavior at the lower frequencies. The transition between the frequency-independent and the frequency-dependent behavior is marked by the critical frequency, f_c (labeled by the dashed line in Figure 4.32, to the ac conductivity versus log of frequency graphs presented in the previous section).

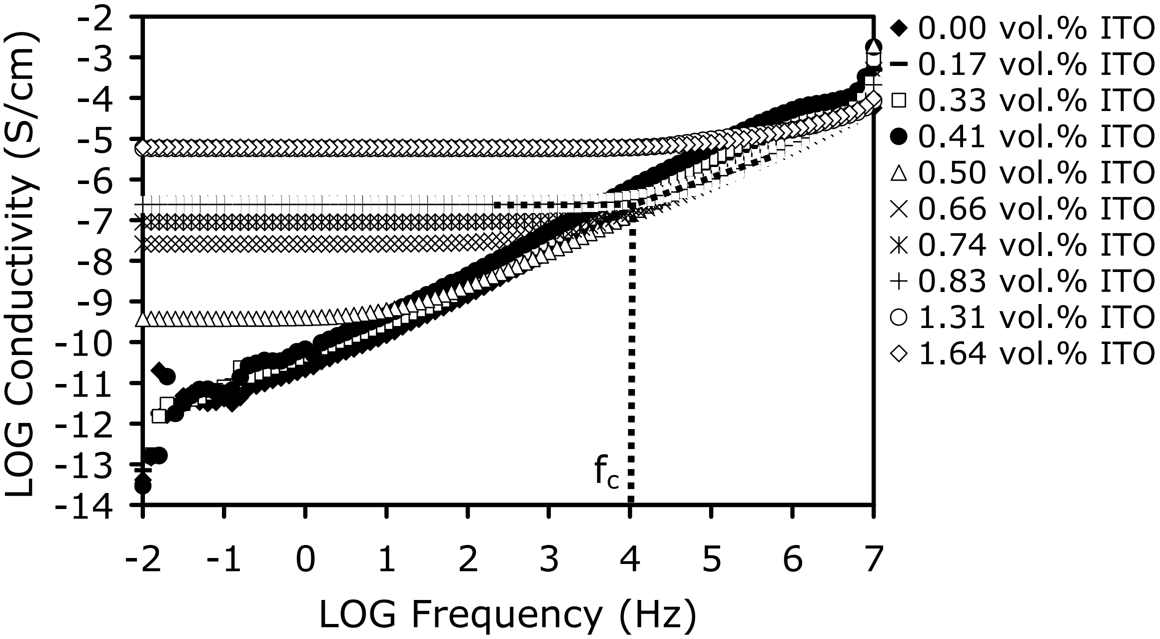

Figure 4.32. The ac conductivity versus frequency for PMMA-ITO nanocomposites as a function of ITO content. The critical frequency, f_c, is indicated for the sample containing 0.83 vol.% ITO.[22]

4.4.1.3 Optical Properties Results[77]

The refractive index and extinction coefficient values of the PMMA-ITO nanocomposites were determined using a modified version of the internal reflection intensity analysis (IRIA) method.[77] Since the samples exhibited high absorbance and scattering, they did not exhibit a linear relationship with the ITO concentration in accordance with the Beer-Lambert Law.[50] It was impossible to acquire the optical constants by conventional methods because a mode pattern could not be obtained from the samples due to their absorbance. The refractive indices of the PMMA-ITO nanocomposites as a function of ITO content are shown in Figure 4.33. The error bars, which represent standard deviations of ±0.001, indicate a systematic error with 0.15 degree resolution.

The IRIA model equations were used to explore the extinction coefficient, k, by taking the differential of the reflectance, R.[77] Differential R vs. k plots were generated from the IRIA equations, assuming air-gap values between 0.03 - 0.05 μm. Figure 4.34 shows how the extinction coefficient was estimated for a PMMA-ITO composite with

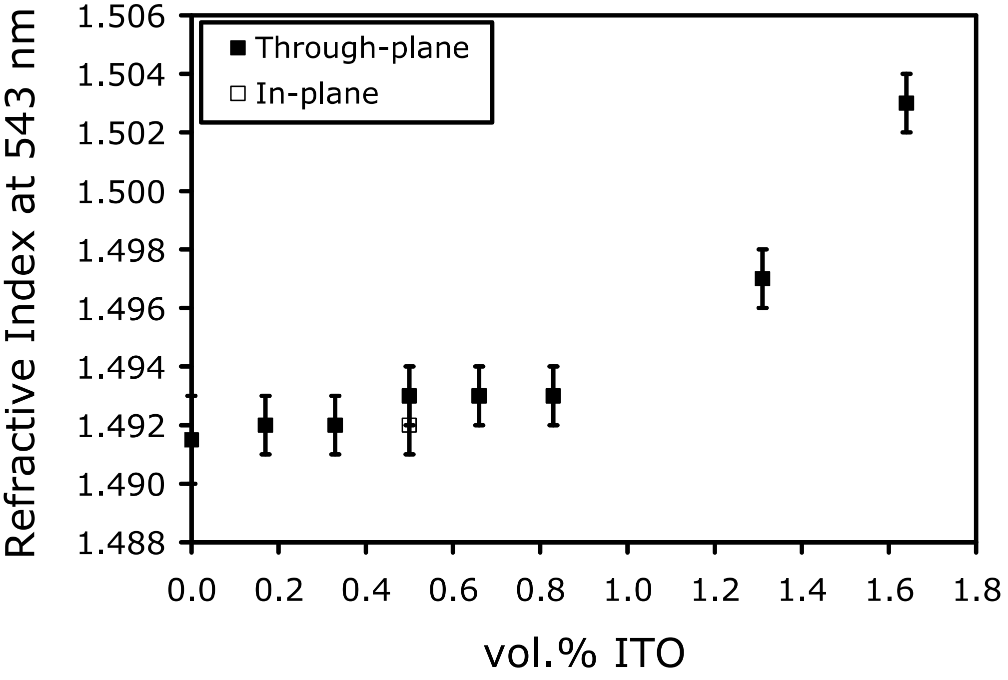

Figure 4.33. Refractive index of PMMA-ITO nanocomposites for 543 nm incident light as a function of ITO content.[22,77]

0.83 vol.% ITO in the in-plane direction with the air-gap boundary conditions. The upper and lower limits for k were estimated by locating the intersection between the break point value in the R vs. β plots (where β is the effective index), and the corresponding differential R vs. k curves. For example, for a break point value of 0.020 (shown in section 4.4.2.2), Fig. 4.34 shows that k lies between 0.005 - 0.008 in the in-plane direction. More details about the estimation of the extinction coefficient values for the PMMA-ITO nanocomposites are described by Li (M.S. Thesis, 2003).[77]

Figure 4.35 displays dependence of the extinction coefficient on the ITO concentration for the PMMA-ITO nanocomposites. The graph shows that the extinction coefficient values increase as more ITO nanoparticles are added to the PMMA matrix. The standard deviations for the estimated values also expand with higher ITO content. The method by which these values were obtained will be described further in Section 4.4.2.

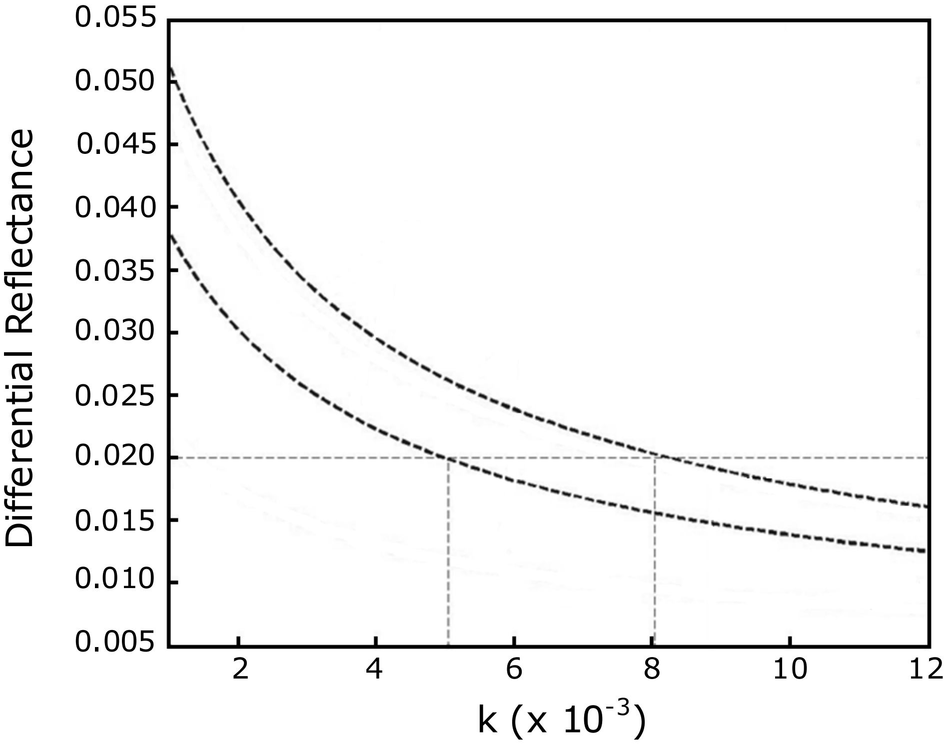

Figure 4.34. The procedure for estimating the extinction coefficient using the modified IRIA method for a PMMA-ITO nanocomposite filled with 0.83 vol.% ITO.[22,77]

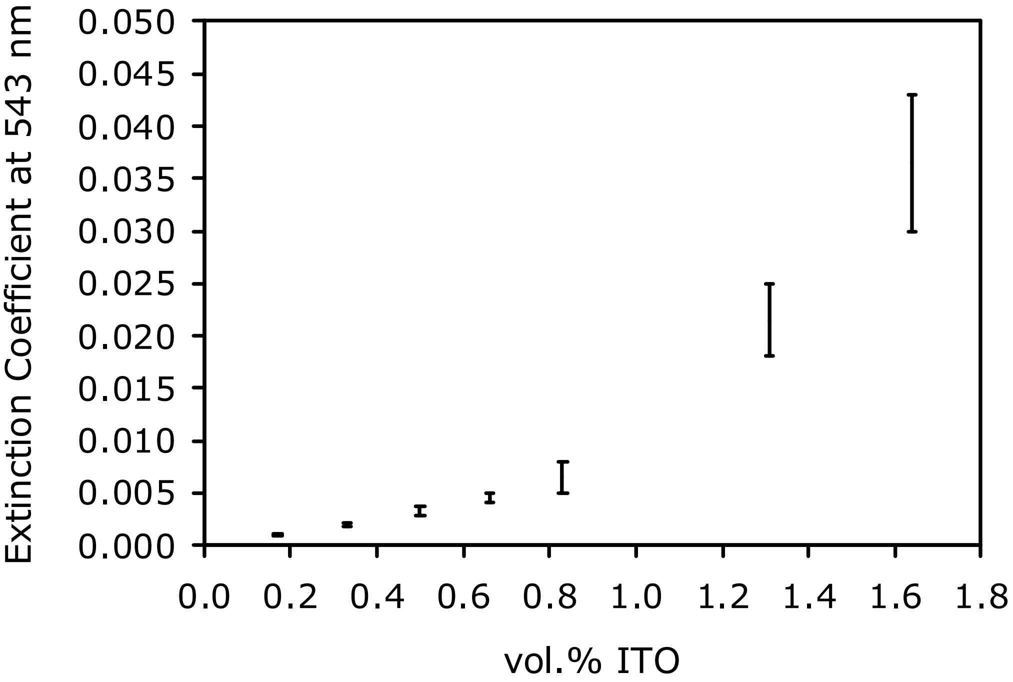

Figure 4.35. Estimated extinction coefficients for PMMA-ITO composites for 543 nm incident light as a function of ITO content, obtained by the modified IRIA method.[22,77]

4.4.2 Analysis and Discussion

4.4.2.1 Electrical Properties/Microstructure Analysis

The additional semicircles in the complex impedance plots (Fig. 4.30c) suggest that different processes are contributing to the electrical conductivity in the PMMA-ITO nanocomposites. Alternatively, the emergence of another semicircle for nanocomposites having higher conductivity suggests that the signal may be related to the change in the ITO concentration. It is doubtful that the additional semicircles are attributed to electrode contact resistance since they occur at frequencies higher than 1 MHz. Contact resistance is typically only observed at much lower frequencies and for materials with significantly higher conductivity.[80] The reason that the additional semicircles were not detected in the complex impedance plots in Set I (Fig. 4.16) is likely due to the lower conductivity of these samples, which is the same reason why they are not observed for the lower compositions in this set.

Figure 4.31 indicates that the percolation threshold occurs between 0.41 and 0.50 vol.% ITO for the PMMA-ITO nanocomposites in Set IV. Based on the observation of the microstructure, it is concluded that the ITO concentrated along the edges of the PMMA particles forms the initial continuous conducting chains (Fig. 4.29). The images of the microstructures of the nanocomposites indicate that the behavior of the ITO nanoparticles is consistent with the data obtained for Set II. Despite the change in pressure distribution due to the adjustment in sample thickness, the ITO nanoparticles do not accumulate onto the faces of the PMMA polyhedral particles until the percolation threshold concentration is well exceeded.

For composites with greater than 0.83 vol.% ITO, the percolation curve in Figure 4.31 shows a monotonic increase in conductivity. The value observed at 1.64 vol.% ITO is approximately two orders of magnitude higher than the conductivity of the nanocomposites in Set II with the same composition. This result is consistent with the conclusions drawn from the information obtained for the nanocomposites in Set III. Increasing the sample thickness results in higher conductivity because there is less penetration of the ITO nanoparticles into the PMMA surfaces. This prevents electrical isolation of the ITO particles, and promotes more continuous chains of ITO particles across the surfaces of the PMMA polyhedral grains, which causes the formation of ITO sheets.

Above f_c, the conductivity increases according to the power law $\sigma(\omega) \propto \omega^x$. Additional information about the microstructure of the PMMA-ITO nanocomposites may be derived upon examination of the ac conductivity (Fig. 4.32). It is presumed that the ITO nanoparticles exist in clusters of different sizes in the microstructure of the composites. For nanocomposites with ITO concentrations lower than the percolation threshold, the SEM images and transmission optical micrographs (Fig. 4.29) have already indicated that these clusters have a wire-like structure. When the first continuous ITO cluster forms and percolation occurs, the ac conductivity reveals both frequency-independent regions (related to direct physical contact) and frequency-dependent regions (related to tunneling/capacitive effects).[5, 95, 96]

In Figure 4.32, the composite with 0.50 vol.% ITO is the first composition to display a plateau representative of dc conductive behavior, although it is likely that the true percolation threshold lies somewhere between 0.41 vol.% ITO and 0.50 vol.% ITO. As the ITO concentration is increased above the percolation threshold, the dc conductive plateau region grows and the frequency dependent behavior becomes less significant, as indicated by the increase in critical frequency (i.e. shifting of the transition between frequency-independent and frequency-dependent regions). This suggests that more physical contacts between the ITO nanoparticles are created as more ITO is added to the matrix. For composites with 1.31 and 1.64 vol.% ITO, the critical frequency cannot be easily detected as both specimens exhibit high dc conductivity, and only show frequency dependence at the highest frequencies ($f_c > 100$ kHz).

Figure 4.36 displays f_c as a function of $|p-p_c|$ plotted in a log-scale for the PMMA-ITO nanocomposites. In this expression, the volume fraction of filler necessary to achieve percolation is $p_c=0.0050$ for this case (see Fig. 4.31). For the PMMA-ITO nanocomposites reported herein, a linear fit was obtained and a value of 1.9 was observed

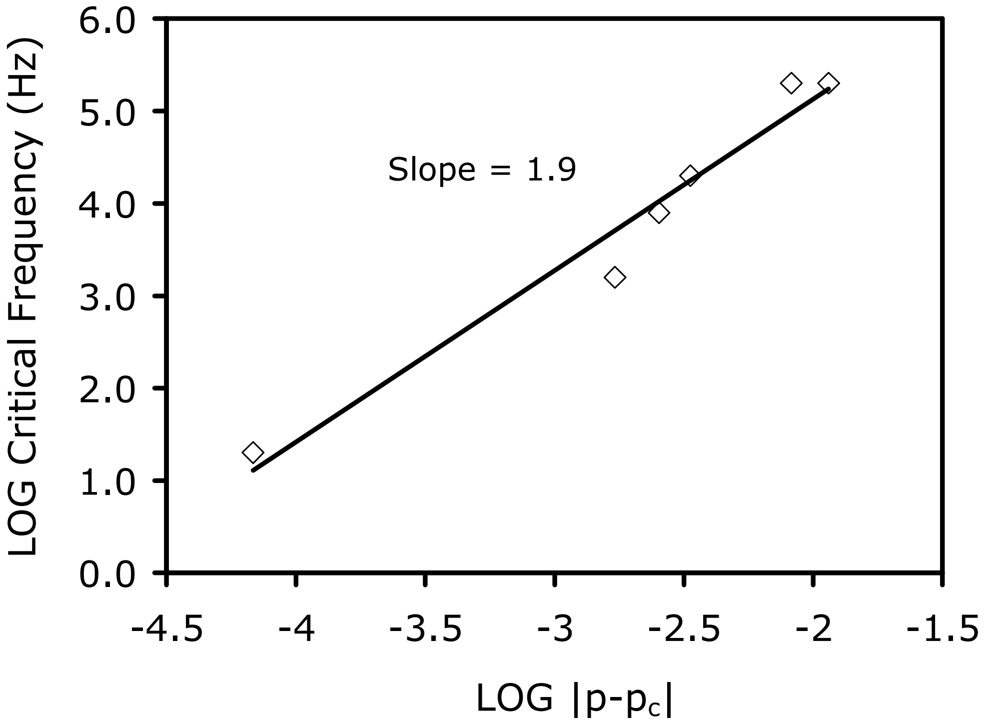

Figure 4.36. Critical frequency f_c as a function of $|p-p_c|$ for PMMA-ITO nanocomposites. ($p_c = 0.0050$)[22]

for the slope, hence, γ=1.9. Exponent values close to this have been obtained for PMMA-CB composites[5] and other materials.[97] As stated in Section 4.3, the meaning of this relationship (Equation 7) is not completely understood, although it has been proposed that this value is associated with the fractal dimension of the aggregates of the filler.[94] The large contrast in the γ values obtained in Figure 4.28a and Figure 4.36 may be attributed to the differences in the microstructures between the specimens, which may indicate that the meaning of γ is specific for different microstructures.

4.4.2.2 Optical Properties/Microstructure Analysis (from Li, M.S. Thesis, 2003)[77]

The overlapped refractive index values for the in-plane and through-plane directions (Fig. 4.33) indicate that the microstructure of the composites is isotropic. This is also consistent with the images of the microstructures presented in Fig. 4.29. However, the refractive index data does not overlap as well for the PMMA-ITO nanocomposite with 0.50 vol.% ITO as compared to the other compositions. It is interesting that a relatively larger standard deviation in the refractive index is observed for this particular composition since the electrical data indicated that this was the first composite sample to exhibit percolation (Fig. 4.31). This trend is consistent with the dc conductivity data, which also shows a larger standard deviation for compositions near the percolation threshold.

Optical constant measurements of polymer-matrix nanocomposites tends to be difficult because they often exhibit high absorbance due to scattering caused by aggregates and/or a refractive index mismatch between the filler and the matrix phase.[86] Consequently, conventional optical techniques (e.g., ellipsometry, reflectometry and prism waveguide coupling) require extremely low absorbance specimens. However, Liu *et al.* previously showed that optical constant measurements could be performed in the near infrared region for hydrogen chloride (HCl)-doped polyaniline films, which typically exhibit high absorbance of infrared light by using the internal reflection intensity analysis (IRIA) method.[76] Liu successfully obtained three-dimensional refractive index and extinction coefficient values for the films by extracting the data directly from the detected intensity. The results showed that by relying on the detected intensity instead of the local minima positions, highly absorbing samples can be analyzed without providing a mode pattern.

The basis of the IRIA method is the analysis of the intensities given by the reflectance-angle data, which permits information about the complex refractive index to be extracted. The details of this approach are described in more detail elsewhere.[76] A typical R vs. β plot obtained for the PMMA-ITO nanocomposites is shown in Figure 4.37a. Similar curves were obtained for all of the composites evaluated here. The effective index is defined as:

$$\beta(\theta) = n_p \sin(\theta_1) \qquad (8)$$

where n_p is the refractive index of the prism and θ is the angle of incident light. Initially, the IRIA equations[76] were attempted to fit the reflectance data. However, with the exception of the PMMA sample that contained no filler, the other curves could not be successfully fit to the model. Figure 4.37a shows that the curvature of the intensity exhibits a discontinuous break point (marked by the arrow), which causes difficulty in fitting the model.[77] The nature of the break point is likely due to light scattering caused by the arrangement of the ITO in the matrix, as depicted in Fig. 4.29.

Even though the data could not be fitted to the theoretical equations, the curve still contains important information about the complex refractive index. When the incident angle is bigger than the critical angle, the incident light is completely reflected, and only an evanescent field goes through the sample.[77] Light transmits through the sample when the incident angle is smaller than the critical angle. Since the scattering effect is different for transmitted light and for the evanescent field, the break point can indicate the critical angle which can be used to calculate the refractive index of the sample using Snell's law.[98]

The sharp change in curvature at the break point in the reflectance data is represented by a peak when the differential (slope of R) is taken. The critical angle was obtained from the peak position in the differential of the reflectance (Figure 4.37b). The

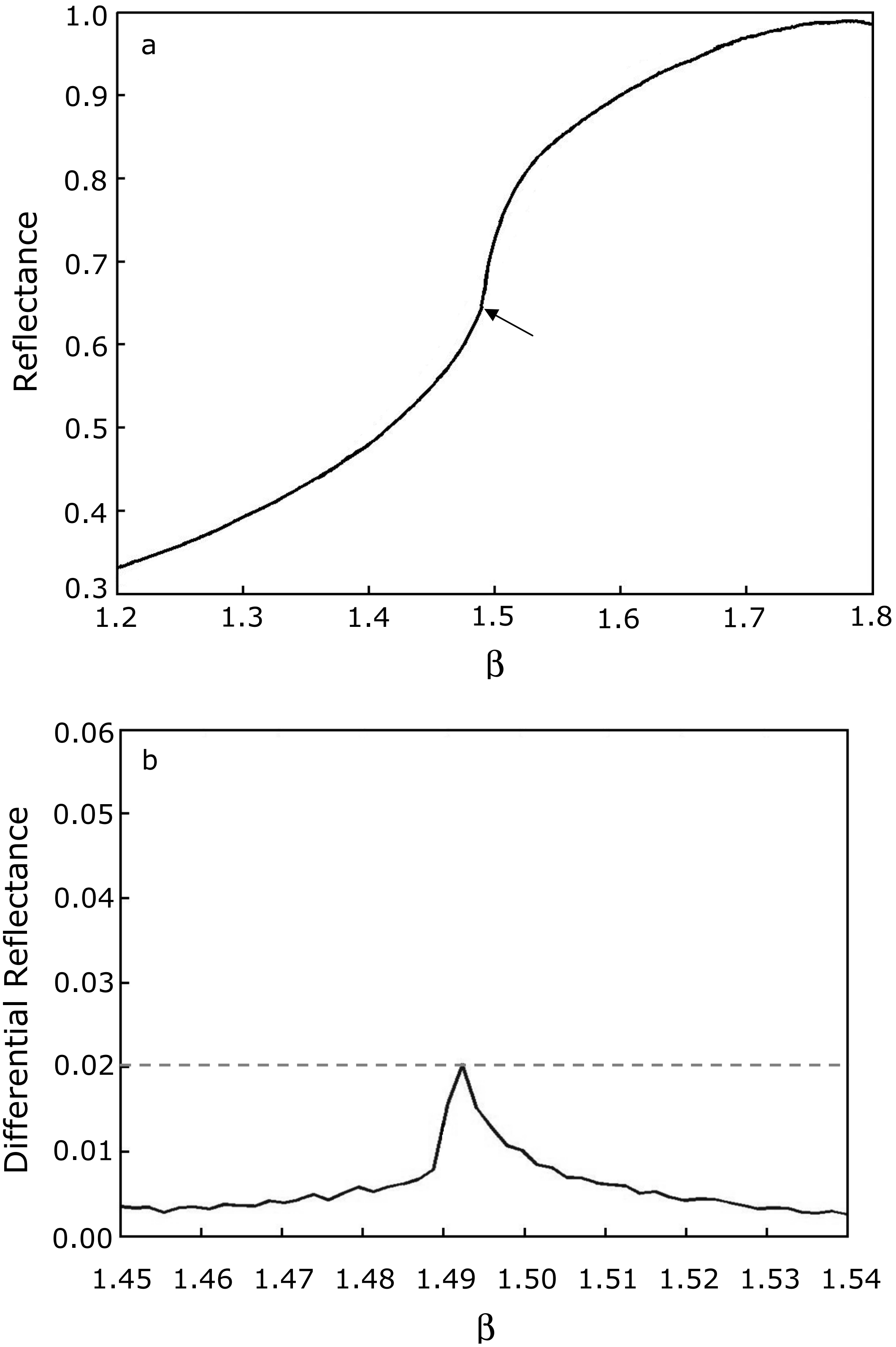

Figure 4.37. (a) In-plane reflectance vs. effective index; and (b) in-plane differential R vs. β for a PMMA-ITO composite filled with 0.83 vol.% ITO.[77]

differential reflectance, D(R), was calculated at each *i*th point by:[77]

$$D_i(R) = (R_{i+1} - R_i)/(\beta_{i+1} - \beta_i) \quad (9)$$

In the IRIA model, each reflectance curve includes three unknowns: the refractive index, the extinction coefficient, and the thickness of the air-gap between the prism and the sample. The reflectance, R, is equal to the $|r|^2$, where r is the reflection coefficient. In this case, the reflection coefficient is given by the following equation:

$$r = [r_{43} + r_{32}\exp(2i\gamma_3)] / [1 + r_{43}r_{32}\exp(2i\gamma_3)] \quad (10)$$

where r_{43} is the reflection coefficient at the interface between the prism and the air-gap, r_{32} is the reflection coefficient at the interface between the air-gap and the sample, and γ_3 is the phase change due to the light traveling across the thickness of the air-gap.[76] Information about the prism for r_{43} is already known, and the values that determine r_{32} are partially known. Since the refractive indices of each sample have already been determined from the peak positions (Fig. 4.37b), this only leaves the extinction coefficient to be calculated for r_{32}. However, in order to estimate the extinction coefficient values, this requires some assumptions about the air-gap for the γ_3 term. In this study, the air-gap thickness was assumed to be between 0.03-0.05 μm. This approximation was chosen mainly due to the good fit of the model to the reflectance-angle data obtained for the PMMA sample that contained no filler.

Additionally, in order to obtain the extinction coefficient from the reflectance-angle data, it was also assumed that the scattering effect is equivalent between the position just before the break point and at the break point. The purpose of this assumption is to cancel the scattering effect at the break point.[77] Therefore, the intensity slope of the PMMA-ITO nanocomposites at the break point will be equivalent to that of a uniform sample with the same refractive index and extinction coefficient. The equivalent sample obtained from making these assumptions can then be described by the model. The following steps were used to estimate the extinction coefficient for each PMMA-ITO nanocomposite:[77]

(i) Based on the IRIA equations, the differential R was generated as a function of the extinction coefficient, k, for the in-plane and through-plane directions. For each direction, a different curve was plotted for each air-gap value (in this case 0.03 μm and 0.05 μm).

(ii) For each polarization, the line tangent to the height of the peak given by the differential R vs. β plots (obtained experimentally) was drawn. An example of the tangent line that was drawn is shown in Fig. 4.37b.

(iii) The tangent lines from step (ii) were overlaid onto the graphs with plots of the differential R vs. k (Fig. 4.34).

The possible extinction coefficient values were extracted by identifying the intersections between the tangent lines and the theoretical plots. Since the refractive index measurements indicated that the microstructures were isotropic, it was appropriate to combine the k range for the in-plane and through-plane directions, and presume that the k limits for the specimens lied where the ranges overlap.

As expected, Fig. 4.34 shows that the extinction coefficient monotonically increases as the ITO concentration is increased in the nanocomposites. This effect is due the increase in scattering as additional contacts exist between the ITO nanoparticles. Although this method cannot give exact values of the extinction coefficient, it provides a novel approach to explore the extinction coefficient values for the nanocomposites described in this study.[77]

4.4.3 Conclusions

AC electrical measurements and optical characterization were performed on thick PMMA-ITO nanocomposites with optimized microstructures. SEM and optical transmission microscopy images of the microstructures revealed that the ITO nanoparticles collect along the edges of the PMMA phase to form a three-dimensional wire-like-network in the nanocomposites. This arrangement of the ITO nanoparticles occurs during the hot pressing of the precursor materials during composite fabrication. The aggregates, which have wire-like structures along the edges of the PMMA matrix particles, are responsible for the electrical percolation observed in the samples. The percolation threshold for the samples in Set IV was identified to be <0.50 vol.% ITO by impedance spectroscopy measurements.

Impedance spectroscopy also detected an additional high frequency process that is related to the electrical conductivity in the PMMA-ITO nanocomposites. These processes were not seen for other the PMMA-ITO nanocomposites in Sets II and III due to their much lower conductivity.

A modified version of the IRIA technique was used to determine the refractive index and extinction coefficient values of the nanocomposites. The values of refractive index obtained for the in-plane and through-plane directions indicated that the microstructure is isotropic. The increase in the estimated extinction coefficient values as the ITO concentration was increased indicates that there is an increase in optical scattering. This increase in scattering is consistent with the creation of additional inter-particle contacts, which occurs when more ITO nanoparticles are added to the PMMA matrix.

CHAPTER 5

PREDICTION OF THE PERCOLATION THRESHOLD

Many theoretical models have been proposed to predict the onset of percolation in two-phase composites. A comprehensive review of percolation models has been provided by Lux.[99] These models can be classified into statistical models,[100, 101] thermodynamic models,[102, 103] geometrical models,[10, 14] and structure-oriented models.[104, 105] The amount of filler needed to achieve percolation in the matrix phase can depend on many factors. Several properties of the component materials, such as the size and shape, chemical nature, and wetting behavior of the filler on the matrix phase, etc., can influence the process by which percolation occurs in the system.

This chapter pertains to the development of a geometrical model in order to address the prediction of percolation of the ITO phase in the PMMA-ITO nanocomposites, which have a phase-segregated microstructure containing faceted PMMA particles. In the first part of the chapter, a mathematical derivation is presented for the prediction of percolation of the ITO nanoparticles in the PMMA phase. The limitations of the expression are discussed, and percolation threshold values given by the model are also compared to percolation threshold values detected by electrical measurements for several composite systems. The polyhedral morphology of the PMMA particles, and the shape of the ITO nanoparticles were taken into account.

The second part of the chapter discusses prediction of percolation of the ITO nanoparticles based on experimental data taken for the PMMA-ITO nanocomposites. Specifically, ultra-small angle x-ray scattering (USAXS) and stereological measurements are used to estimate the diameter and length, respectively, of the ITO aggregate structures along the edges of the PMMA particles. The data was used to calculate the volume fraction of ITO nanoparticles that should be necessary to completely occupy the edges of the PMMA particles in the PMMA-ITO nanocomposites.

5.1. Geometrical Model Predicting the Percolation Threshold in PMMA-ITO Nanocomposites

Because the exponent *t* in the equation $\sigma_{dc}=\sigma_m|p - p_c|^t$ does not take certain factors into account (e.g. particle shape, chemical interaction between the filler and matrix, etc.,), the value of *t* is often not a constant and is specific for different composite systems.[89, 90] A geometrical model is proposed to attempt to predict the percolation threshold for nanocomposites that have phase-segregated microstructures with polyhedral-shaped matrix particles. The concept of the model is based on the original model proposed by De and co-workers,[10] but has been modified to account for the polyhedral morphology of the PMMA particles.

Based on the transmission optical micrographs and SEM images, the following is assumed:

1. *The initial sharp increase in the conductivity of the PMMA-ITO nanocomposites is due to the ITO nanoparticles accumulated along the edges of the PMMA particles.*

The relationship between the amount of ITO necessary to completely cover the surfaces of the PMMA particles and the amount of ITO required for percolation of the ITO nanoparticles is given by Equation 1.

$$X_{A,\ \mathrm{theoretical}} = P_C \cdot X_{B,\ \mathrm{surface}} \qquad (1)$$

where $X_{A,theoretical}$ corresponds to the volume fraction of ITO nanoparticles necessary for percolation in the specimens, $X_{B,surface}$ is the ITO volume fraction required to completely occupy the surfaces of each PMMA particle, and P_C is the critical percolation probability. For this case, P_C is the factor that relates $X_{A,theoretical}$ and $X_{B,surface}$ and represents the volume fraction necessary for the non-zero probability that the ITO nanoparticles are part of a percolating cluster. For the proposed model, a value of P_C=0.225 will be used, which is the critical probability estimated by Frary and Schuh for 3-dimensional percolation of cubic grain edges in truncated octahedral particles.[106] It should be clearly noted that this value of P_C applies to edge percolation of cubic grains within the polyhedral particles, and is not ideal for the model proposed here. However, this value will be used for the current case since it loosely considers the polyhedral morphology of the PMMA particles and the event of percolation occurring 3-dimensional space.

Based on the transmission optical micrographs and the SEM images which indicate that the PMMA particles form a space-filling microstructure, the second assumption for this model is as follows:

2. *The PMMA particle geometry is a truncated octahedron.*

Truncated octahedra are a type of space-filling polyhedra that consist of fourteen faces and thirty-six edges.[107] For this condition, the average volume and surface area (per unit edge length) of the matrix particles are calculated to be 11.3 and 26.8, respectively.[108] The equivalent volume and surface area in terms of the initial spherical size may be estimated as follows:

$$V_p = (4/3)\pi r_p^3 = 11.3 a_{vp}^3 \qquad (2)$$

which gives $0.68r_p = a_{vp}$ and

$$S_p = 4\pi r_p^2 = 26.8a_{sp}^2 \tag{3}$$

which gives $0.98r_p = a_{sp}$, where a_{vp} and a_{sp} are the edge length of the volume and surface area of each polyhedral matrix particle, respectively; and r_p is the radius of the initial spherical particle. These terms are also described in the microstructure schematics shown in Figure 5.1.

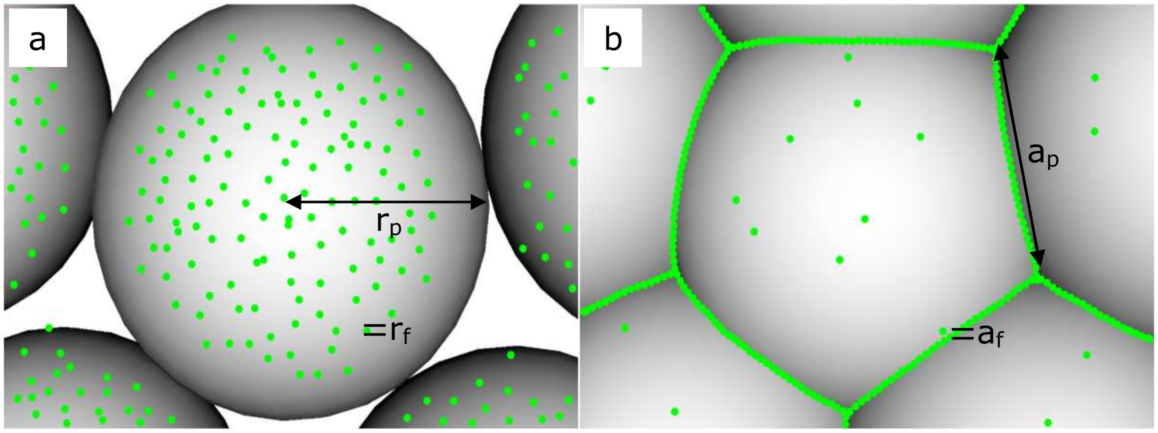

Figure 5.1. Illustrations of ITO-coated PMMA particles (a) before compression molding, and (b) after compression molding. The labels r_p and r_f are the radii of the initially spherical PMMA particles and the assumed spherically-shaped ITO nanoparticles, respectively. The labels a_p and a_f represent the edge length of the deformed PMMA particles and cubic ITO nanoparticles, respectively.

Based on the TEM image of the ITO nanoparticles presented in Fig. 4.4a (page 42), the shape of the ITO nanoparticles will be considered as geometric cubes for the model. However, since the average particle size is normally assumed as spherical shapes, the equivalent size of the nanoparticles in the nanocomposites will be determined as follows:

$$V_f = (4/3)\pi r_f^3 \approx a_f^3 \tag{4}$$

which gives $1.61r_f = a_f$, where r_f is the radius of the filler particle as a sphere, and a_f is the edge length of the particle as a cube.

The volume fraction of ITO nanoparticles necessary to cover the surface of the PMMA particles can be obtained from:

$$X_{B,surface} = nV_f/V_p = n\,(1.61r_f)^3 / 11.3a_{vp}^3 \qquad (5)$$

where V_f and V_p are the total volume of the filler and matrix particles, respectively; and n is the number of filler particles that are necessary to occupy the entire surface of each matrix particle. The number of particles, n, may be estimated from:

$$n = S_p / S_f = 26.8a_{sp}^2 / (1.61r_f)^2 \qquad (6)$$

where S_p and S_f are the total surface area of the matrix and filler particles, respectively. Combining Equations (5) and (6) and substituting the spherical radii of equivalent volume gives:

$$X_{B,surface} = [(1.61r_f)^3 \cdot 26.8(0.68r_p)^2] / [(11.3(0.72r_p)^3 \cdot (1.61r_f)^2] = 4.73\, r_f/r_p \qquad (7)$$

In order to check the validity of the proposed model, the percolation threshold values calculated with Equations 1 and 7 were compared to values determined by electrical measurements for the PMMA-ITO nanocomposites. Based on the average particle size of the ITO nanoparticles detected by the USAXS measurements (described in next section), and the size distribution of the PMMA particles shown in the SEM images, a value of 2500 was used for the r_p/r_f ratio for the PMMA-ITO nanocomposites (corresponding to r_p=37.5 μm/r_f=15 nm). The experimental percolation threshold values observed for PMMA-CB nanocomposites[5] and ABS-CB nanocomposites[16] that possessed similar microstructures, consisting of polyhedral-shaped matrix particles, were also compared to values predicted by the model for those composite systems. The results are displayed in Table 5.1.

The predicted values based on these r_p/r_f ratios are much lower than the values detected by the electrical measurements of the PMMA-ITO and PMMA-CB composite systems. In addition to the value P_C=0.225 being non-ideal for this problem, differences between the predicted and experimentally obtained values may also be attributed to the particle size distributions of the matrix and filler particles, and uneven distribution of the filler particles in the matrix.

Table 5.1. Comparison of predicted percolation thresholds with experimental values for polymer-matrix composites that have phase-segregated microstructures, with filler-coated faceted matrix particles.

Ref.	r_p/r_f	Composite System	Predicted Range for X_A	Experimental values of X_A
[22]	2500	PMMA-ITO	0.00043	0.0033-0.0050
[5]	[a]3571	PMMA-CB	0.00030	0.0013-0.0026
[16]	[b]1.45×10^5	ABS-CB	0.0000073	~0.000054

[a] Results for CB particle size, r_f = 10.5 nm; PMMA particle size, r_p = 37.5 μm

[b] Results for CB particle size, r_f = 12 nm; ABS particle size r_p = 1.75 mm (since the initial ABS particle shape was spheroidal, the average particle radius was used)

It should be noted that this model requires an appropriate critical percolation probability value that only applies to percolation of the perimeter particle edges. It is also necessary for the polyhedral-shaped matrix particles to have a well-defined geometry, so that the equivalent volume and surface areas can be accurately calculated from the initial spherical state of the matrix particles.

5.2. Experimental-Based Prediction of the Percolation Threshold in PMMA-ITO Nanocomposites

5.2.1 Determination of Diameter Distribution of ITO Aggregate Structures by USAXS

An experimental approach was also used in order to estimate the volume fraction of ITO nanoparticles necessary to fill the edges of the PMMA particles and achieve percolation. USAXS imaging has previously shown that percolation of carbon black (CB) nanoparticles in CB-PMMA nanocomposites occurs in a similar manner to what is proposed in the model.[20] Figure 5.2 shows USAXS images of CB-PMMA nanocomposites[5, 20] that have a very similar phase-segregated microstructure, and contain polyhedral-shaped PMMA matrix particles.[5, 23]

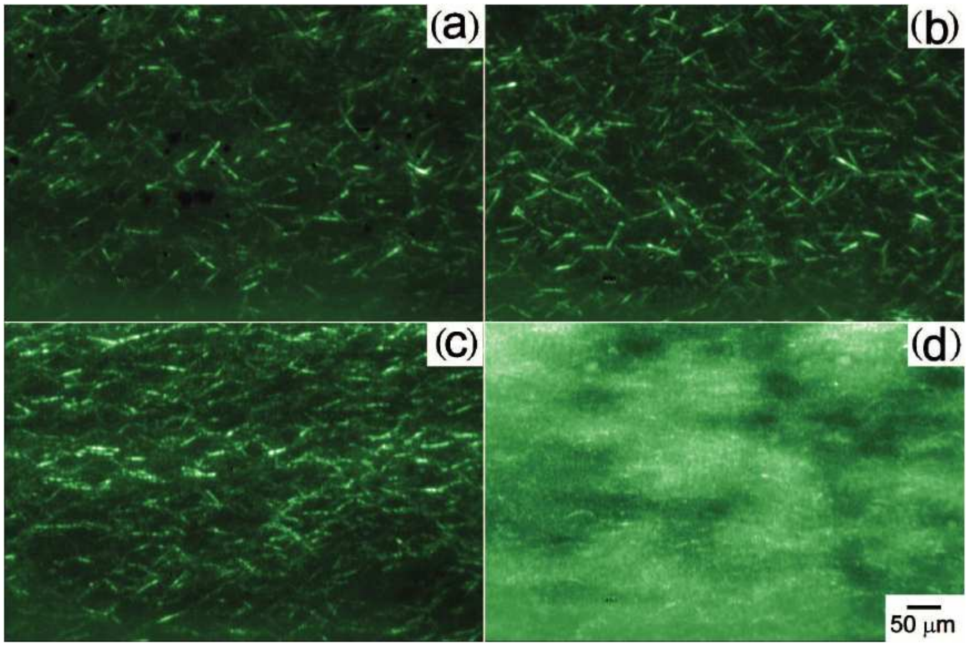

Figure 5.2. USAXS images CB-PMMA nanocomposites with (a) 0.4 wt.% CB; (b) 1.0 wt.% CB; (c) 4.8 wt.% CB; (d) 13.0 wt.% CB.[20]

In Figure 5.2, the bright objects are the result of scattering from CB nanoparticle aggregates. The USAXS images definitively show the distribution behavior of the CB nanoparticles in the microstructure of the CB-PMMA nanocomposites as the CB concentration is increased. At low concentrations (Fig. 5.2a-b), the CB nanoparticles form wire-like aggregates in the PMMA matrix.[20] This can be attributed to the CB nanoparticles collecting at the edges of the PMMA particles, which have a polyhedral geometry.[5] The transmission optical images in Figure 5.3[5] also display a CB distribution in the PMMA-CB nanocomposites that is similar to the ITO distribution shown by the transmission optical micrograph and SEM image in Figure 4.8a-b for the PMMA-ITO nanocomposites.

As the CB concentration increases in the CB-PMMA nanocomposites, the wire-like objects become distorted and scattering is detected over the entire region imaged by the USAXS beam (Fig. 5.2c-d). This is attributed to the CB distribution becoming displaced onto the faces of the faceted PMMA particles,[20] which is analogous to the behavior of the ITO distribution in Figure 4.14 as the ITO concentration is increased in the PMMA-ITO nanocomposites. Notably, electrical measurements indicated that percolation of the CB nanoparticles occurred at 0.4 wt.% CB (~0.26 vol.% CB) in the PMMA-CB nanocomposites. This composition is imaged in Figure 5.2b, where morphology of the aggregate structures of the CB nanoparticles still resembles wires.

Figure 5.4 shows USAXS data obtained for the PMMA-ITO nanocomposites. The measurements were taken in the scattering vector, Q, range between 10^{-4}-10^{-1} Å^{-1}, where λ is the incident wavelength and 2θ is the scattering angle (Equation 8). The USAXS intensities display two regions in Figure 5.4 for the nanocomposites.

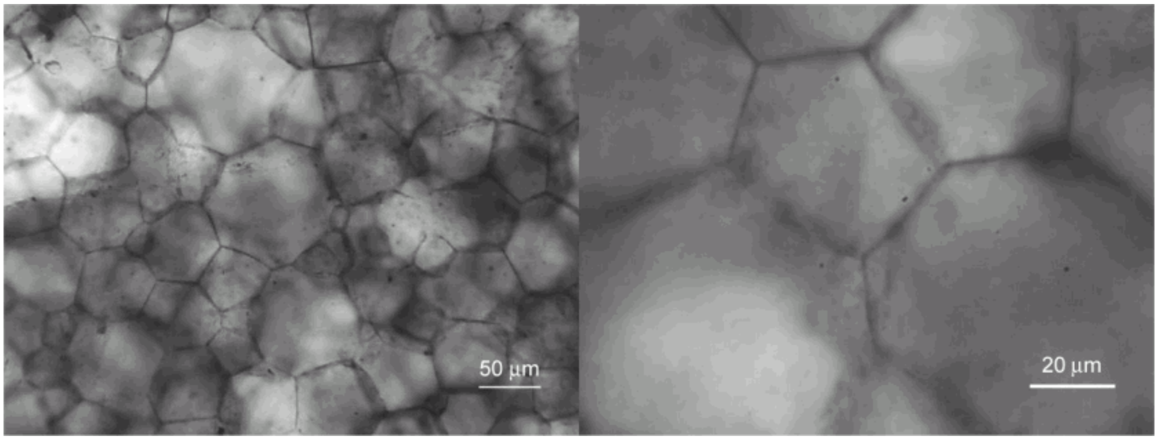

Figure 5.3. Transmission optical micrographs of a PMMA-CB nanocomposite containing 0.10 wt.% CB.[5]

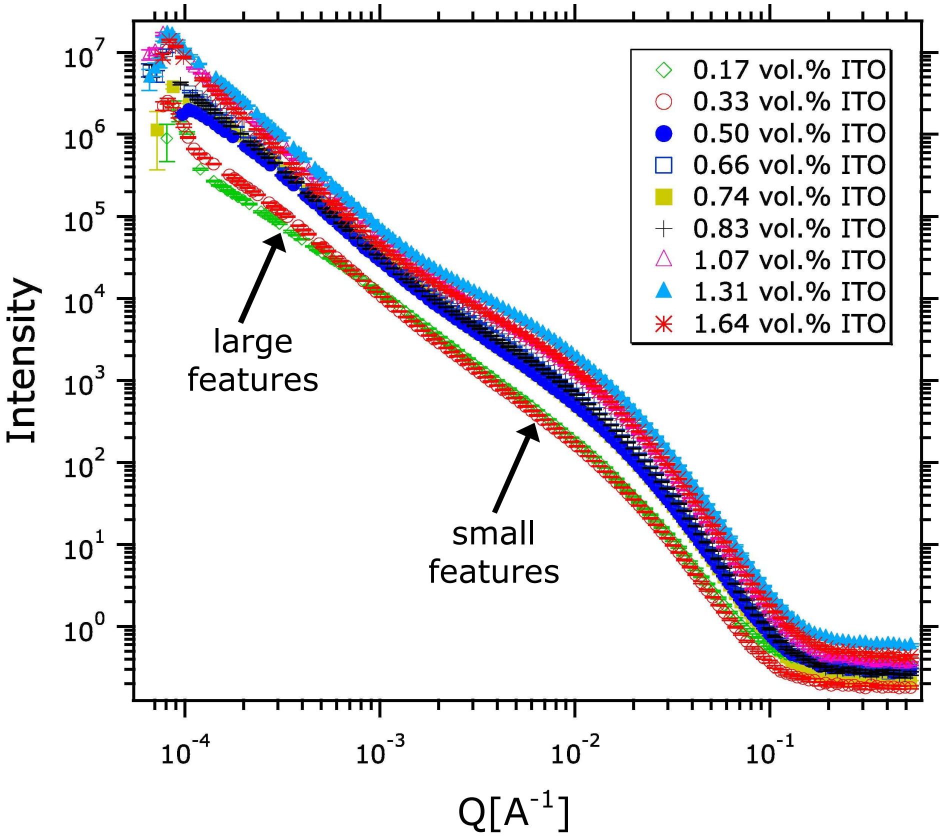

Figure 5.4. USAXS data for PMMA-ITO nanocomposites.

The scattering in the higher Q range corresponds to smaller objects (e.g., individual ITO nanoparticles); and the data taken in the lower region, Q <10^{-3} Å^{-1}, is related to larger features. It is proposed that the data acquired for Q >10^{-3} Å^{-1} describes the size of the growing ITO aggregates as the ITO concentration is increased in the nanocomposites.

$$Q = (4\pi/\lambda)\sin\theta, \tag{8}$$

Based on the transmission optical micrographs and SEM images of the microstructures of the PMMA-ITO nanocomposites (Fig. 4.8a-b, Fig. 4.14), the 'Unified Rod' form factor[110] was used to fit and model the USAXS data shown in Fig. 5.4. The formula for the Unified Rod model is displayed in Equation 9:

$$\begin{aligned} I(q) \approx G_1 \exp\left(\frac{-Q^2 r_{g1}^2}{3}\right) + B_1 \left[\frac{erf\,(Qr_{g2}/\sqrt{6}))^3}{Q}\right]^4 + \\ \exp\left(\frac{-Q^2 r_{g2}^2}{3}\right) + B_2 \left[\frac{erf\,(Qr_{g2}/\sqrt{6}))^3}{Q}\right] * \exp\left(\frac{-Q^2 r_{g1}^2}{3}\right) \end{aligned} \tag{9}$$

where $G_1 = \frac{2r}{(3L)}, r_{g1} = \frac{r\sqrt{3}}{2}, B_1 = \frac{4(L+r)}{(L^2 r^3)}, r_{g2} = \sqrt{\left(\frac{r^2}{2} + \frac{L^2}{12}\right)}, B_2 = \frac{\pi}{L},$ Q is the scattering vector, r is the radius of the scattering object, and L is the length of the object.[109] This is the same form factor that was used to fit the USAXS data previously obtained for PMMA-CB nanocomposites.[20]

This model was applied to specifically obtain the diameter of the ITO aggregate wire structures along the edges of the PMMA particles in the specimens. Since the Unified Rod model is meant for cases like dilute solutions of carbon nanotubes, information about the ITO volume fraction cannot be accurately extracted from the analysis. A value of 24 μm for the length of the ITO aggregates was input for the modeling because the program did not allow fitting of this dimension. This value was based on the stereology calculations described in Section 5.2.2. However, it was observed after varying the length value that it was inconsequential to the fitted results, due to the nature of the form factor in Equation 9.

Regions of the curve in Figure 5.4 were fitted separately in order to distinguish between scattering from the ITO nanoparticles or small ITO clusters, and the larger ITO aggregates that most likely contribute to percolation in the samples, described in Figure 5.1b. Figure 5.5a shows the diameter distribution extracted from the USAXS data between 10^{-3} $Å^{-1} > Q > 10^{-1}$ $Å^{-1}$ for the PMMA-ITO nanocomposites containing 0.17-0.50 vol.% ITO. Figure 5.5a shows a high relative volume fraction between 10-100 nm. This distribution shows good agreement with the initial particle size distribution of ITO Filler A (used for the PMMA-ITO nanocomposites in Sets II and IV) displayed in Figure 4.4a. As expected, the diameter distribution shifts toward increasing values as the ITO concentration is increased in the PMMA-ITO nanocomposites.

Figure 5.5b shows the diameter distribution extracted from the USAXS data between 10^{-4} $Å^{-1} > Q > 10^{-3}$ $Å^{-1}$ for PMMA-ITO nanocomposites with 0.17-0.50 vol.% ITO. In the lower Q range, the diameter appears to have a more clearly defined bimodal distribution, with peak positions around 500-1000 nm (0.5-1.0 μm) and 1,500-3,000 nm (1.5-3.0 μm). The increase in the ITO nanoparticle concentration in the composites provides the normal force required for the diameter of the ITO aggregates to grow. Therefore, a smaller fraction of the ITO nanoparticles are only able to join the "wire-network" initially responsible for percolation. Figure 5.5b indicates that as the ITO

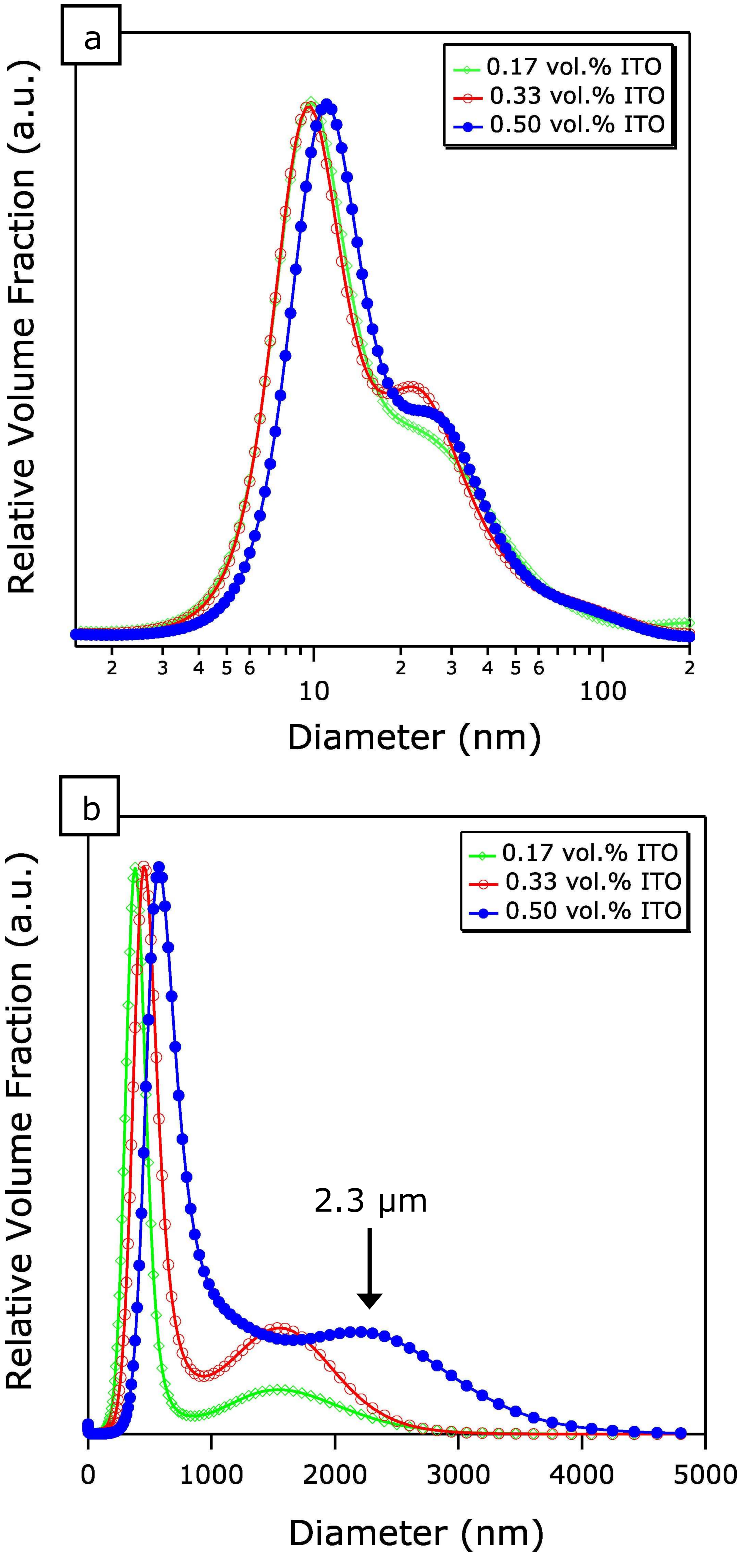

Figure 5.5. Diameter distribution of scattering objects extracted from USAXS data between (a) 10^{-3} $Å^{-1}$ > Q > 10^{-1} A^{-1} and (b) 10^{-4} $Å^{-1}$ > Q > 10^{-3} $Å^{-1}$ for PMMA-ITO nanocomposites containing 0.17-0.50 vol.% ITO.

concentration is increased from 0.33 vol.% ITO to 0.50 vol.% ITO, the diameter distributions at ~500 nm and 1-3 μm begin to overlap.

Based on the images of the microstructures (Fig. 4.14) and the electrical measurements displaying percolation of the ITO nanoparticles at 0.50 vol.% ITO in the PMMA-ITO nanocomposites (Fig. 4.17), it is proposed that the larger diameter distribution obtained for this composition represents the diameter of the ITO aggregates when the percolation threshold is reached. It is reasonable to use the peak value of the larger diameter distribution in Figure 5.5b for the PMMA-ITO nanocomposite with 0.50 vol.% ITO (marked by the arrow) because this value likely represents the diameter of the ITO aggregate wire structures shortly before they begin to occupy the faces of the PMMA particles, which is assumed to be the point where percolation occurs. The estimated diameter value, d=2.3μm, of the ITO aggregate wire structures associated with percolation in the specimens is also reasonable since the ITO aggregates are visible in optical images obtained at the micron scale (Fig. 4.13a-b).

5.2.2. Edge Length per Unit Volume

Stereological measurements were used to estimate the total edge length of the PMMA particles in the PMMA-ITO nanocomposites. The procedure was followed according to the description provided by Gokhale[110] and Smith and Guttman,[111] where the edge length per unit volume, L_v, is given by Equation 10:

$$L_v = 2\langle Q_A \rangle \qquad (10)$$

and Q_A represents the average number of triple points (for this case) per unit area. Since features, such as particle edges, in 3-D structures appear as points in 2-D sections, an unbiased counting frame was applied to several transmission optical micrographs similar to that shown in Figures 4.8a and 4.13a. By this method, the edge length per unit volume was calculated as L_v=7.98 x 10^{-4} μm/μm^3 for the samples. Figure 5.6 shows a schematic and the values determined from the experimental measurements for the dimensions of the ITO aggregate wire structures, where L_v has been normalized by the volume of a PMMA particle ($a_{p,stereology}$).

Using the equation for the volume of a cylinder, the formula displayed in Equation 11 was used to calculate the predicted percolation threshold for the PMMA-ITO nanocomposites:

$$X_{B,edges} = [\ \pi(d_{USAXS}/2)^2 \text{ x } (L_v \text{ x } V_{ref})\ ] / V_{ref} \tag{11}$$

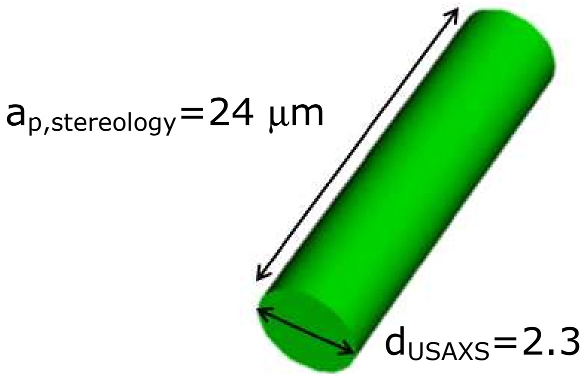

Figure 5.6. Schematic representing the values used to describe the dimensions of the ITO aggregate wire structures in the PMMA-ITO nanocomposites.

where $X_{B,edges}$ is the calculated volume fraction of ITO nanoparticles required to occupy all of the edges of the PMMA particles in the nanocomposites. Equation 11 gives a $X_{B,edges}$ value of 0.0033 ITO. This value is near the percolation threshold observed in the electrical measurements (Fig. 4.17). Reasons for the difference between the experimentally-based calculation and the values observed in the electrical measurements are:

1. Only a fraction of the ITO nanoparticles present in the PMMA-ITO nanocomposites are contributing to the 3-dimensional percolating network;
2. The wide size distribution of the ITO nanoparticles and PMMA particles;
3. Some of the ITO aggregates may not have been detected by the USAXS measurements due to insufficient scattering over the Q range currently available experimentally.

5.3 Conclusions

A geometrical model was proposed to predict the percolation threshold for the PMMA-ITO nanocomposites. The geometrical model took into account the polyhedral morphology of the PMMA matrix particles, and the shape of the ITO nanoparticles. However, the discrepancy between the theoretical model and the percolation threshold determined by electrical measurements of the specimens is attributed to a suitable critical percolation probability value, as it applies to this particular percolation problem, not being available in the current literature. Therefore, a different experimental approach was taken based on USAXS and stereology measurements in order to calculate the expected percolation threshold in the PMMA-ITO nanocomposites. For the new approach, the dimensions of the ITO aggregates along the edges of the polyhedral PMMA particles was taken into account, which had previously been determined to be cylindrically-shaped based on images of the microstructures of the specimens. Fair agreement between the experimental calculation of the percolation threshold and the percolation threshold detected by electrical measurements of the specimens strongly indicate that the ITO aggregate wire structures are responsible for percolation of the ITO nanoparticles in the PMMA-ITO nanocomposites described in this research.

CHAPTER 6

CONCLUSIONS AND FUTURE WORK

6.1 Conclusions

PMMA-ITO nanocomposites with unique phase-segregated microstructures were successfully fabricated via compression molding of ITO-coated PMMA particles. The microstructures consist of polyhedral-shaped PMMA particles, and ITO nanoparticles that self-assemble into wire structures below or near the percolation threshold concentration for the ITO nanoparticles in the nanocomposites. When the ITO concentration is increased above the percolation threshold, this results in the formation of sheets across the faces of the polyhedral PMMA particles. A combination of impedance spectroscopy, optical spectroscopy, conventional and scanning electron microscopy, and ultra-small angle x-ray scattering were used to establish correlations between the electrical and optical properties and the microstructures of the PMMA-ITO nanocomposites. Using these techniques, it was possible to establish that the ITO nanoparticles exist as wire-shaped aggregates when the ITO concentration reaches the percolation threshold in the PMMA matrix. It was further determined that the displacement of the ITO nanoparticles towards the edges of the polyhedral-shaped PMMA particles was responsible for percolation of the ITO nanoparticles in the system.

Impedance spectroscopy was the primary non-destructive technique used to investigate variations in the microstructures of the PMMA-ITO nanocomposites as a function of ITO concentration and the composite fabrication parameters. Upon examination of the critical frequency, the impedance measurements were able to detect when different degrees of segregation existed between ITO and PMMA phases in the specimens. A new relationship was introduced between the critical frequency and the dc conductivity, which clearly showed the dependence of the interconnectivity of the filler on the resultant microstructure. In general, it was determined that the PMMA-ITO nanocomposites exhibited the maximum electrical conductivity when the pressure distribution during the composite fabrication was low, and the PMMA and ITO particles remained segregated.

Ultra-small angle x-ray scattering and stereological measurements were used to estimate the dimensions of the wire-like ITO aggregates formed in the PMMA-ITO nanocomposites. The information collected by these techniques was used to predict the ITO concentration that should be necessary for percolation of the ITO nanoparticles to occur, based on the assumption that the wire-like ITO aggregates were responsible for percolation in the specimens. These results were compared to the percolation threshold detected by the electrical measurements, and it was determined that there was fair agreement amongst the data and that this assumption is reasonable. Additionally, a geometrical model based on volume-to-surface area ratios between the ITO and PMMA particles was also proposed in order to predict the percolation threshold. However, it was difficult to determine the accuracy of this model since a suitable critical percolation probability value is currently unavailable.

6.2 Suggestions for Future Work

1. In this research, it was demonstrated that percolation could be achieved with low volume fractions of the ITO nanoparticles when segregation is preserved between the PMMA and ITO particles in the composite. However, the particle size

distributions of the ITO and PMMA particles play a significant role in determining the percolation threshold and displacement of the ITO nanoparticles towards the edges and across the faces of the polyhedral PMMA particles. A better understanding of the behavior of the microstructure could be attained if similar experiments to those described in this research were repeated with filler and matrix particles that have narrower size distributions. This might reduce the standard deviations present in the electrical measurements, and aid in determining the accuracy of the models.

2. When the composite fabrication parameters were optimized and higher electrical conductivities were achieved in the PMMA-ITO nanocomposites, the complex-plane impedance plots revealed two super-imposed semi-circles. It would be useful if these features could be resolved and associated with a component of the microstructure or a specific electrical process. Applying ac/dc bias or performing the electrical measurements at higher temperatures may be helpful in identifying the source of these additional signals. Further understanding of the electrical response will provide a more accurate correlation between the electrical properties and microstructures of the PMMA-ITO nanocomposites.

3. It was shown that USAXS imaging and USAXS measurements are powerful tools in identifying the aggregate behavior of the filler particles in the matrix. It would be useful if USAXS measurements could be taken at lower Q values to verify that all of the significant details about the size distribution of the aggregates in the matrix were detected.

4. During the course of this research, it was discovered that ITO nanoparticles could be easily synthesized having a narrow size distribution and excellent dispersion properties in non-polar solvents. These materials hold the potential for many future research projects. Due to the dispersion properties, optical spectra obtained from an ITO nanoparticle suspension could be correlated with several other properties such as oxygen stoichiometry, carrier concentration, or electrical conductivity. Additionally, the nano-scale surface dimensions could lead to interesting application studies related to transparent-conducting inks or low temperature sintering for nanoparticle thin films.

APPENDIX A - Chemical Synthesis of ITO Filler C

ITO Filler C was synthesized by a colloidal chemistry route. The precursors and molar quantities used are given in Table A.2.

Table A.1. Molar quantities of precursors used to synthesize colloidal ITO nanoparticles.

$In(Ac)_3$	$Sn(Ac)_2$	ODA	MA
0.0009	0.0001	0.003	0.003

Indium acetate ($In(Ac)_3$, 99.99%), tin acetate ($Sn(Ac)_2$), myristic acid (99-100%), octadecanol (99%), and 1-octadecene (90%) were obtained from Sigma-Aldrich and stored in a nitrogen-filled glove box. Chloroform and acetone were obtained from VWR Scientific. The synthesis reaction was performed using a custom-made apparatus drawn in Figure A.1a. In order to initiate the reaction under inert conditions, a 2-neck flask (Part 2) was connected to two flow lines through a condenser coil (Part 4) and an airfree adapter with a T-bore stopcock (Part 5). One flow line delivered argon gas and the other line lead to a standard vacuum pump. The line leading to the argon gas source was also connected to an airfree bubbler containing mineral oil (Fig. A.1, Part 6) to confirm sufficient gas flow from the tank. The other neck attached to the flask was connected to a beaker filled with mineral oil (Part 7), to ensure that the argon gas was flowing out properly and that the reaction flask was experiencing positive pressure.

$In(Ac)_3$, $Sn(Ac)_2$, myristic acid, and octadecylamine were combined with 25 ml of octadecene in the 2-neck flask. The contents of the flask were degassed and heated to

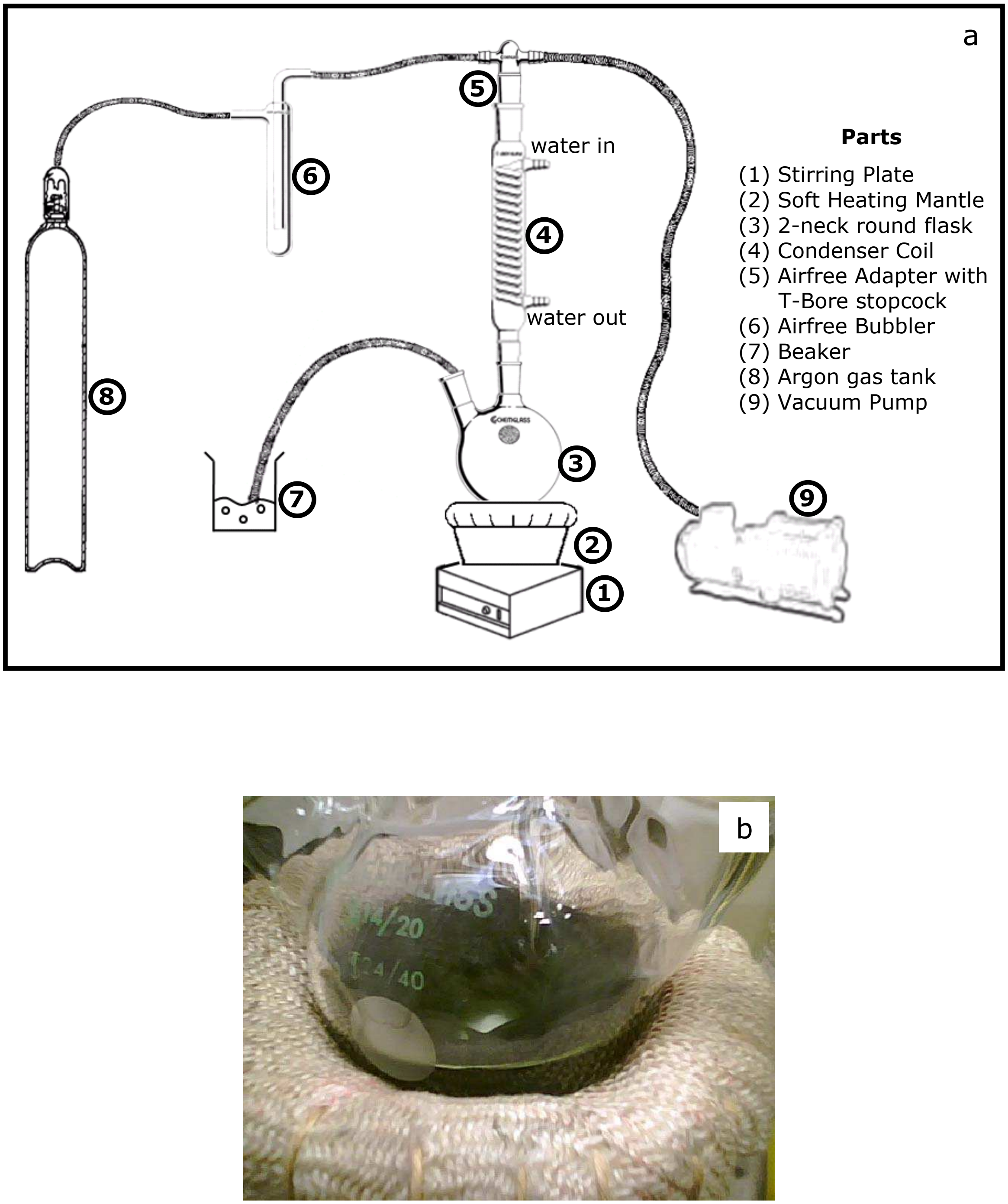

Figure A.1. (a) Schematic of custom-made apparatus designed for the synthesis of colloidal ITO nanoparticles; (b) Image of colloidal ITO nanoparticles synthesized in reaction flask over the heating mantle.

295°C. A stirring plate (Part 1) and a heating mantle (Part 2) were combined to heat the precursors while under constant stirring. After the precursors became dissolved and the solution turned clear below 200 °C, a color change to pale yellow was noticeable at 250°C. When the temperature reached 295°C, the solution became dark green with no sign of turbidity. Figure 3.1b shows an image of the solution at 295 °C in the reaction flask. Tap water was circulated through the condenser coil (Fig. A.1a, Part 5) for the duration of the synthesis process to prevent the loss of octadecene by evaporation.

The flask was gradually cooled to room temperature and chloroform was added to the solutions in order to keep any residual organics in a dissolved state and to facilitate the collection of the nanoparticles. The nanoparticles were isolated by standard polar/non-polar solvent techniques. This involved separating the solution into several centrifuge tubes, and adding acetone to each tube. The acetone causes the ligands on the surface of the nanoparticles to retract, which promotes agglomeration of the nanoparticles. This allowed a high-speed centrifuge to segregate the nanoparticles from the rest of the solution in the tubes. After the nanoparticles were forced to the bottom of the tubes and the supernatant was poured off, they were combined with chloroform and additional acetone. This process was repeated 2-3 times before the nanoparticles were finally re-dispersed in pure chloroform in sample tubes.

APPENDIX B – Non-destructive Testing of ITO Nanoparticles

A significant advantage of nanoparticles synthesized by colloidal chemistry methods is that the nanoparticles tend to have good dispersability in non-polar solvents. Since fatty acids or amines are typically used, their surfactant properties provide steric hindrance to attractive Van der Waals forces, which prevents agglomeration of the nanoparticles.[85] This trait allows the characterization of as-synthesized ITO nanoparticles without any additional sintering or film-forming steps.[67] Property information can be extracted from colloidal ITO nanoparticles suspensions by non-destructive optical spectroscopy techniques. Figures B.1 and B.2 display Tauc plots and photoluminescence (PL) maps, respectively, for colloidal ITO nanoparticles suspended in chloroform after being precipitated under aerated and argon environments.

As a result of synthesizing the ITO nanoparticles under an oxygen-deficient atmosphere, the oxygen vacancies acted as donors and increased the optical band gap energy in the nanoparticles.[55] The Tauc plot (Fig. B.1) indicates that the Burstein-Moss effect could be detected in the ITO nanoparticles from the absorbance/transmittance spectra.[67]

Changes in the band structure of the colloidal ITO nanoparticles, as a result of precipitation under aerated and inert conditions, were also detected by PL measurements (Fig. B.2). The emissions may be related to excitons created from oxygen vacancies.[64, 112-115] The blue shift observed in the features displayed in the PL map of the ITO synthesized under argon, compared to the ITO synthesized under aerated conditions, is attributed to the higher number of oxygen vacancies present in the nanoparticles. Please refer to Reference 67 for further details about this work.

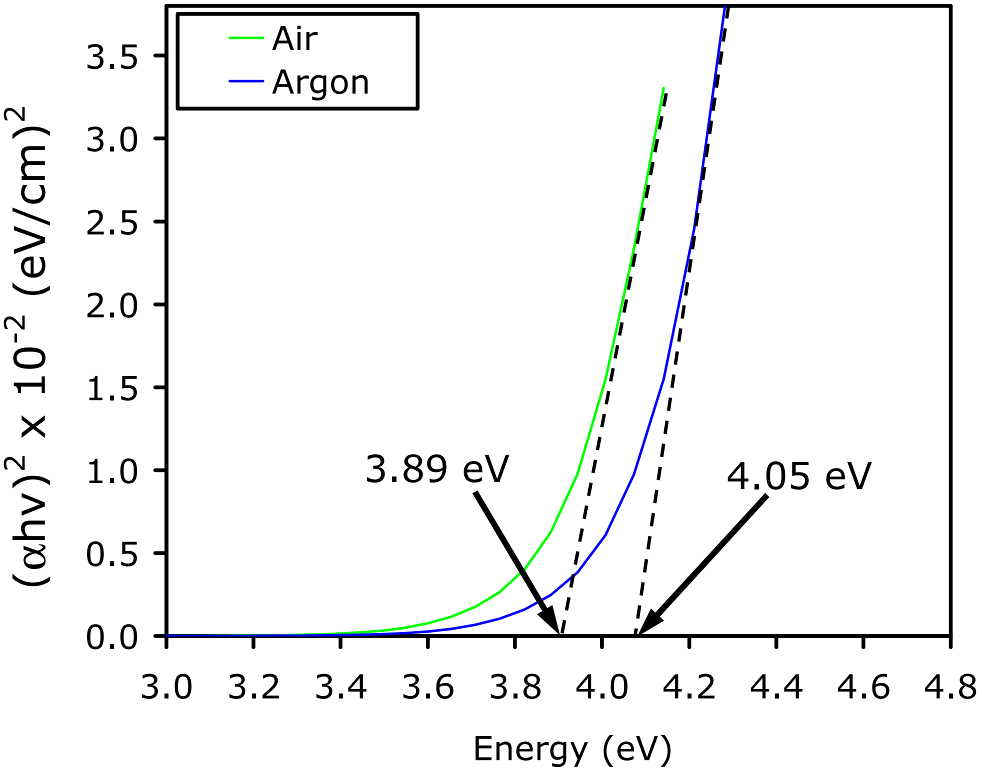

Figure B.1. Plot of $(\alpha h\nu)^2$ vs. photon energy for colloidal ITO in chloroform synthesized under air and argon.[67]

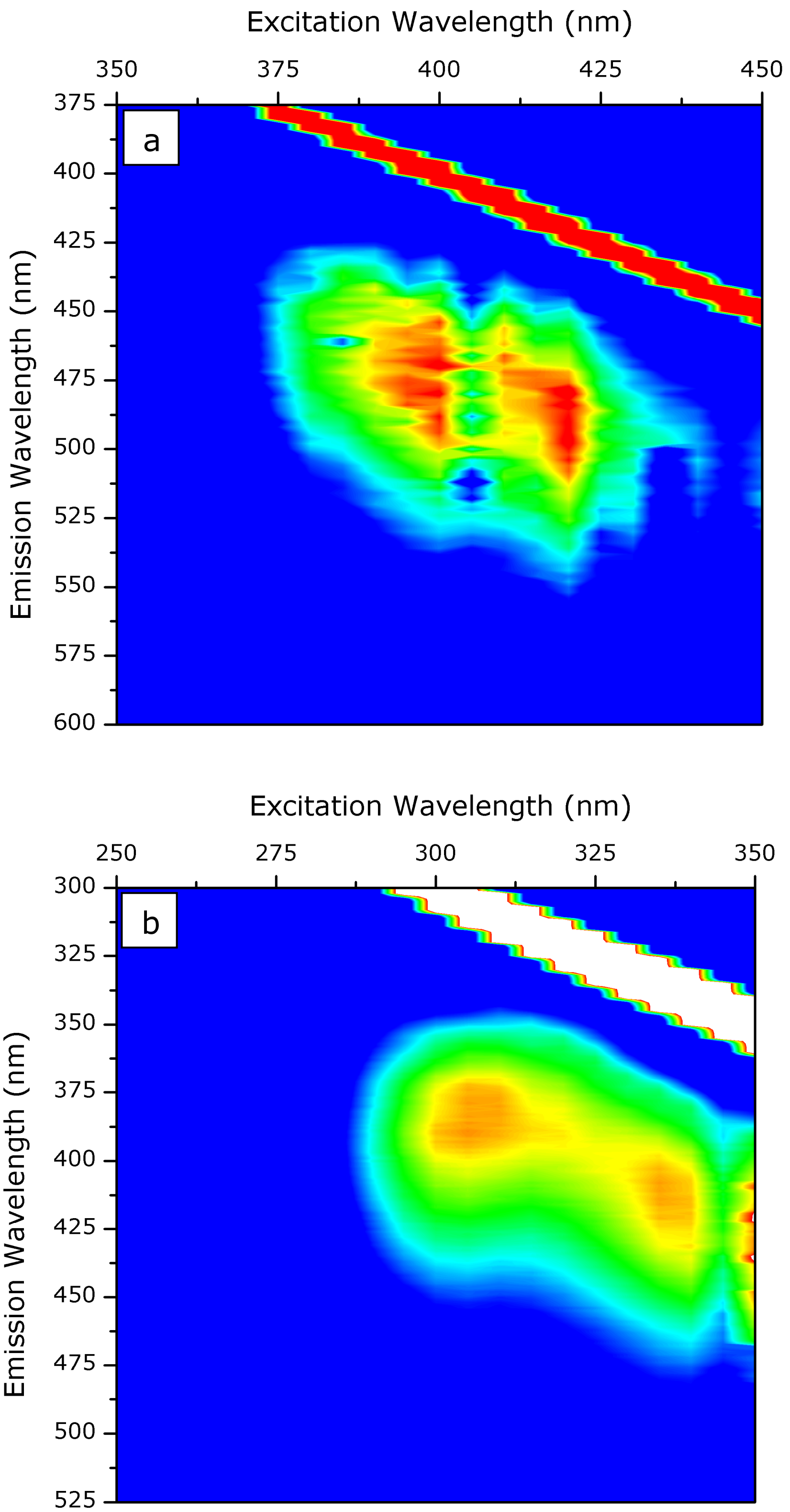

Figure B.2. PL map of colloidal ITO nanoparticles in chloroform synthesized under a) air and b) argon.[67]

REFERENCES

[1] M. Zhang, W. Jia, and C. X., "Influence of Crystallization Histories on PTC/NTC Effects of PVDF/CB Composites," *J. Appl. Polym. Sci.*, vol. 62, 1996.

[2] H. Tang, J. H. Piao, X. F. Chen, Y. X. Luo, and S. H. Li, "The Positive Temperature-Coefficient Phenomenon of Vinyl Polymer CB Composites," *Journal of Applied Polymer Science*, vol. 48, pp. 1795-1800, 1993.

[3] C. Calberg, S. Blacher, F. Gubbels, F. Brouers, R. Deltour, and R. Jerome, "Electrical and dielectric properties of carbon black filled co-continuous two-phase polymer blends," *Journal of Physics D-Applied Physics*, vol. 32, pp. 1517-1525, 1999.

[4] F. Gubbels, R. Jerome, P. Teyssie, E. Vanlathem, R. Deltour, A. Calderone, V. Parente, and J. L. Bredas, "Selective Localization of Carbon Black in Immiscible Polymer Blends: A Useful Tool To Design Electrical Conductive Composites," *Macromolecules*, vol. 27, pp. 1972-1974, 1994.

[5] R. Q. Ou, S. Gupta, C. A. Parker, and R. A. Gerhardt, "Fabrication and electrical conductivity of poly(methyl methacrylate) (PMMA)/Carbon black (CB) composites: Comparison between an ordered carbon black nanowire-like segregated structure and a randomly dispersed carbon black nanostructure," *Journal of Physical Chemistry B*, vol. 110, pp. 22365-22373, 2006.

[6] A. Malliaris and D. T. Turner, "Influence of Particle Size on Electrical Resistivity of Compacted Mixtures of Polymeric and Metallic Powders," *Journal of Applied Physics*, vol. 42, pp. 614-618, 1971.

[7] R. P. Kusy and D. T. Turner, "Electrical Conductivity of a Polyurethane Elastomer Containing Segregated Particles of Nickel," *Journal of Applied Polymer Science*, vol. 17, pp. 1631-1633, 1973.

[8] R. P. Kusy and D. T. Turner, "Electrical Resistivity of a Polymeric Insulator containing Segregated Metallic Particles," *Nature Physical Science*, vol. 229, pp. 58-59 1971.

[9] R. Mukhopadhyay, S. K. De, and S. Basu, "Effect of Metal Concentration on Electrical-Conductivity and Some Mechanical-Properties of Poly(Methyl Methacrylate)-Copper Composites," *Journal of Applied Polymer Science*, vol. 20, pp. 2575-2580, 1976.

[10] S. K. Bhattacharya, S. Basu, and S. K. De, "Effect of Size, Shape and Oxide Content of Metal Particles on Formation of Segregated Networks in PVC Composites," *Composites*, vol. 9, pp. 177-183, 1978.

[11] G. Pinto and A. K. Maaroufi, "Conducting polymer composites of zinc-filled urea-formaldehyde," *Journal of Applied Polymer Science,* vol. 96, pp. 2011-2015, 2005.

[12] C. M. Chan, C. L. Cheng, and M. M. F. Yuen, "Electrical properties of polymer composites prepared by sintering a mixture of carbon black and ultra-high molecular weight polyethylene powder," *Polymer Engineering and Science,* vol. 37, pp. 1127-1136, 1997.

[13] J. Bouchet, C. Carrot, J. Guillet, G. Boiteux, G. Seytre, and M. Pineri, "Conductive composites of UHMWPE and ceramics based on the segregated network concept," *Polymer Engineering and Science,* vol. 40, pp. 36-45, 2000.

[14] R. P. Kusy, "Influence of Particle-Size Ratio on Continuity of Aggregates," *Journal of Applied Physics,* vol. 48, pp. 5301-5305, 1977.

[15] C. J. Capozzi, S. Shackelford, R. Ou, and R. A. Gerhardt, "Study of Percolation in PMMA/Indium Tin Oxide Composites," *Materials Research Symposium Proceedings,* vol. 819, pp. 303-308, 2004.

[16] S. Gupta, R. Q. Ou, and R. A. Gerhardt, "Effect of the fabrication method on the electrical properties of poly(acrylonitrile-co-butadiene-co-styrene)/carbon black composites," *Journal of Electronic Materials,* vol. 35, pp. 224-229, 2006.

[17] C. J. Capozzi and R. A. Gerhardt, "Novel Percolation Mechanism in PMMA matrix Composites containing Segregated ITO Nanowire Networks," *Advanced Functional Materials,* vol. 17, pp. 2515-2521, 2007.

[18] R. A. Gerhardt, R. Ou, Z. Li, R. J. Samuels, and C. J. Capozzi, "Composite materials having low filler percolation thresholds and methods of controlling filler interconnectivity," in *US 2006186384 A1 20060824* 2006.

[19] S. K. Bhattacharya and A. C. D. Chaklader, "Review on Metal-Filled Plastics. Part 1. Electrical Conductivity," *Polymer Plastics Technology Engineering,* vol. 19, pp. 21-51, 1982.

[20] L. E. Levine, G. G. Long, J. Ilavsky, R. A. Gerhardt, R. Ou, and C. A. Parker, "Self-assembly of carbon black into nanowires that form a conductive three dimensional micronetwork," *Applied Physics Letters,* vol. 90, p. 014101, 2007.

[21] C. J. Capozzi and R. A. Gerhardt, "Correlation of the ac Electrical Conductivity and the Microstructure of PMMA/ITO Nanocomposites That Possess Phase-Segregated Microstructures," *Journal of Physical Chemistry C,* vol. 112, pp. 19372-19382, 2008.

[22] C. J. Capozzi, Z. Li, R. J. Samuels, and R. A. Gerhardt, "Impedance spectroscopy and optical characterization of polymethyl methacrylate/indium tin oxide nanocomposites with three-dimensional Voronoi microstructures," *Journal of Applied Physics,* vol. 104, p. 114902, 2008.

[23] R. Ou, S. Gupta, C. A. Parker, and R. A. Gerhardt, "Low Percolation Threshold Composites Consisting of PMMA and Carbon Black," *TMS Letters,* vol. 2, pp. 117-118, 2005.

[24] C. Klason and J. Kubat, "Anomalous Behavior of Electrical-Conductivity and Thermal Noise in Carbon Black-Containing Polymers at Tg and Tm," *Journal of Applied Polymer Science,* vol. 19, pp. 831-845, 1975.

[25] H. Takele, U. Schurmann, H. Greve, D. Paretkar, V. Zaporojtchenko, and F. Faupel, "Controlled growth of Au nanoparticles in co-evaporated metal/polymer composite films and their optical and electrical properties," *European Physical Journal-Applied Physics,* vol. 33, pp. 83-89, 2006.

[26] R. Haggenmueller, H. H. Gommans, A. G. Rinzler, J. E. Fischer, and K. I. Winey, "Aligned single-wall carbon nanotubes in composites by melt processing methods," *Chemical Physics Letters,* vol. 330, pp. 219-225, 2000.

[27] O. Breuer and U. Sundararaj, "Big returns from small fibers: A review of polymer/carbon nanotube composites," *Polymer Composites,* vol. 25, pp. 630-645, 2004.

[28] J. Dealy and K. Wissbrun, *Melt Rheology and Its Role in Plastics Processing*. New York: VNR, 1990.

[29] J. S. Reed, *Principles of Ceramic Processing*, 2nd ed. New York: John Wiley & Sons, 1995.

[30] J. Gurland, "The measurement of distribution, spacing, contact, and continuity of particles in a matrix," in *Plansee Proceedings, S*, F. Benesovky, Ed. Vienna: Springer-Verlag, 1961, pp. 507-517.

[31] J. Gurland, "An Estimate of Contact and Continuity of Dispersions in Opaque Samples," *Transactions of the Metallurgical Society of AIME,* vol. 236, pp. 642-646, 1966.

[32] R. Schueler, J. Petermann, K. Schulte, and H. P. Wentzel, "Agglomeration and electrical percolation behavior of carbon black dispersed in epoxy resin," *Journal of Applied Polymer Science,* vol. 63, pp. 1741-1746, 1997.

[33] Q. Z. Xue, "The influence of particle shape and size on electric conductivity of metal-polymer composites," *European Polymer Journal*, vol. 40, pp. 323-327, 2004.

[34] J. P. Schaffer, A. Saxena, S. D. Antolovich, T. H. Sanders, Jr., and S. B. Warner, *The Science and Design of Engineering Materials*, 2nd ed. New York: McGraw-Hill Companies, Inc., 1999.

[35] W. Callister, Jr., *Materials Science and Engieering: An Introduction*, 5th ed. New York: John Wiley & Sons, 2000.

[36] A. T. Ponomarenko, V. G. Shevchenko, and N. S. Enikolopyan, "Formation Processes and Properties of Conducting Polymer Composites," *Advances in Polymer Science*, vol. 96, pp. 125-147, 1990.

[37] J. P. Jog, "Solid-State Processing of Polymers - a Review," *Advances in Polymer Technology*, vol. 12, pp. 281-289, 1993.

[38] A. Greco and A. Maffezzoli, "Polymer melting and polymer powder sintering by thermal analysis," *Journal of Thermal Analysis and Calorimetry*, vol. 72, pp. 1167-1174, 2003.

[39] F. Hochberg, in *U.S. Patent 2,721,357*, 1955.

[40] Y. S. Kim, K. S. Liao, C. J. Jan, D. E. Bergbreiter, and J. C. Grunlan, "Conductive thin films on functionalized polyethylene particles," *Chemistry of Materials*, vol. 18, pp. 2997-3004, 2006.

[41] R. J. Andrews and E. A. Grulke, *Polymer Handbook*, 4th ed. New York: Wiley, 1999.

[42] P. Ehrenfest, "Phase conversions in a general and enhanced sense, classified according to the specific singularities of the thermodynamic potential," *Proceedings of the Koninklijke Akademie Van Wetenschappen Te Amsterdam*, vol. 36, pp. 153-157, 1933.

[43] S. Saito and T. Nakajima, "Glass Transition in Polymers," *Journal of Applied Polymer Science*, vol. 2, pp. 93-99, 1959.

[44] W. Kauzmann, "The Nature of the Glassy State and the Behavior of Liquids at Low Temperatures," *Chemical Reviews*, vol. 43, pp. 219-256, 1948.

[45] G. C. Kuczynsk, B. Neuville, and H. P. Toner, "Study of Sintering of Poly(Methyl Methacrylate)," *Journal of Applied Polymer Science*, vol. 14, pp. 2069-2077, 1970.

[46] M. Narkis, "Sintering Behavior of Poly(Methyl Methacrylate) Particles," *Polymer Engineering and Science,* vol. 19, pp. 889-892, 1979.

[47] B. G. Lewis and D. C. Paine, "Applications and processing of transparent conducting oxides," *MRS Bulletin,* vol. 25, pp. 22-27, 2000.

[48] R. G. Gordon, "Criteria for choosing transparent conductors," *MRS Bulletin,* vol. 25, pp. 52-57, 2000.

[49] J. U. Brehm, M. Winterer, H. Hahn, G. Michael, and A. Gutsch, "Indium Tin Oxide Nanoparticles Prepared by Chemical Vapor Synthesis," *Materials Research Symposium Proceedings,* vol. 704, p. 61, 2001.

[50] W. D. Kingery, H. K. Bowen, and D. R. Uhlmann, *Introduction to Ceramics*. New York: John Wiley & Sons, 1976.

[51] K. L. Chopra, S. Major, and D. K. Pandya, "Transparent Conductors - a Status Review," *Thin Solid Films,* vol. 102, pp. 1-46, 1983.

[52] Y. Z. You, Y. Kim, D. H. Choi, H. S. Jang, J. H. Lee, and D. Kim, "Electrical and optical study of ITO films on glass and polymer substrates prepared by DC magnetron sputtering type negative metal ion beam deposition," *Materials Chemistry and Physics,* vol. 107, pp. 444-448, 2008.

[53] Q. Qiao, J. Beck, R. Lumpkin, J. Pretko, and J. T. McLeskey, "A comparison of fluorine tin oxide and indium tin oxide as the transparent electrode for P3OT/TiO_2 solar cells," *Solar Energy Materials and Solar Cells,* vol. 90, pp. 1034-1040, 2006.

[54] T. J. Coutts, D. L. Young, and X. N. Li, "Characterization of transparent conducting oxides," *Mrs Bulletin,* vol. 25, pp. 58-65, 2000.

[55] I. Hamberg, C. G. Granqvist, K. F. Berggren, B. E. Sernelius, and L. Engstrom, "Band-Gap Widening in Heavily Sn-Doped In_2O_3," *Physical Review B,* vol. 30, pp. 3240-3249, 1984.

[56] S. Homma, A. Miyamoto, S. Sakamoto, K. Kishi, N. Motoi, and K. Yoshimura, "Pulmonary fibrosis in an individual occupationally exposed to inhaled indium-tin oxide," *European Respiratory Journal*, vol. 25, pp. 200-204, 2005.

[57] T. Homma, T. Ueno, K. Sekizawa, A. Tanaka, and M. Hirata, "Interstitial pneumonia developed in a worker dealing with particles containing indium-tin oxide," *Journal of Occupational Health,* vol. 45, pp. 137-139, 2003.

[58] J. R. Bellingham, W. A. Phillips, and C. J. Adkins, "Electrical and Optical-Properties of Amorphous Indium Oxide," *Journal of Physics-Condensed Matter,* vol. 2, pp. 6207-6221, 1990.

[59] T. Karasawa and Y. Miyata, "Electrical and Optical-Properties of Indium Tin Oxide Thin-Films Deposited on Unheated Substrates by Dc Reactive Sputtering," *Thin Solid Films,* vol. 223, pp. 135-139, 1993.

[60] C. P. Udawatte and K. Yanagisawa, "Sintering of additive free hydrothermally derived indium tin oxide powders in air," *Journal of Solid State Chemistry,* vol. 154, pp. 444-450, 2000.

[61] P. K. Biswas, A. De, K. Ortner, and S. Korder, "Study of sol-gel-derived high tin content indium tin oxide (ITO) films on silica-coated soda lime silica glass," *Materials Letters,* vol. 58, pp. 1540-1545, 2004.

[62] T. Furusaki, J. Takahashi, and K. Kodaira, "Preparation of ITO Thin-Films by Sol-Gel Method," *Nippon Seramikkusu Kyokai Gakujutsu Ronbunshi-Journal of the Ceramic Society of Japan,* vol. 102, pp. 200-205, 1994.

[63] S. S. Kim, S. Y. Choi, C. G. Park, and H. W. Jin, "Transparent conductive ITO thin films through the sol-gel process using metal salts," *Thin Solid Films,* vol. 347, pp. 155-160, 1999.

[64] S. Kundu and P. K. Biswas, "Synthesis and photoluminescence property of nanostructured sol-gel indium tin oxide film on glass," *Chemical Physics Letters,* vol. 414, pp. 107-110, 2005.

[65] J. Zhang, K. H. Au, and S. Y. Chang, "Investigation of sol-gel derived Indium tin oxide thin films with poly(ethylene glycol) as an additive," *Journal of Ceramic Processing Research,* vol. 5, pp. 208-213, 2004.

[66] C. J. Capozzi, R. A. Gilstrap, C. J. Summers, and R. A. Gerhardt, "The Role of Nanotechnology in the Applications of IndiumTin Oxide Nanoparticles," Oak Ridge, TN: 2007 Oak Ridge National Laboratory Users Meeting, October 2007.

[67] C. J. Capozzi, I. N. Ivanov, S. Joshi, and R. A. Gerhardt, "Effect of Atmosphere on the Optical Properties of As-Synthesized Colloidal ITO," *Nanotechnology,* vol. 20, p. 145701, 2009.

[68] S. I. Choi, K. M. Nam, B. K. Park, W. S. Seo, and J. T. Park, "Preparation and optical properties of colloidal, monodisperse, and highly crystalline ITO nanoparticles," *Chemistry of Materials,* vol. 20, pp. 2609-2611, 2008.

[69] R. A. Gilstrap, C. J. Capozzi, C. G. Carson, A. Y. Borisevich, R. A. Gerhardt, and C. J. Summers, "Synthesis of a Nonagglomerated Indium Tin Oxide Nanoparticle Dispersion," *Advanced Materials*, vol. 20, pp. 4163-4166, 2008.

[70] X. Peng, Y. Chen, N. Jana, and A. Narayanaswamy, "Synthetic Control of Metal Oxide Nanocrystal Sizes and Shapes," in *US 2006021152A1*, 2006.

[71] G. Bühler, D. Tholmann, and C. Feldmann, "One-pot synthesis of highly conductive indium tin oxide nanocrystals," *Advanced Materials,* vol. 19, pp. 2224-2227, 2007.

[72] G. Carotenuto, M. Valente, G. Sciume, T. Valente, G. Pepe, A. Ruotolo, and L. Nicolais, "Preparation and characterization of transparent/conductive nano-composites films," *Journal of Materials Science,* vol. 41, pp. 5587-5592, 2006.

[73] H. Miyazaki, T. Ota, and I. Yasui, "Design of ITO/transparent resin optically selective transparent composite," *Solar Energy Materials and Solar Cells,* vol. 79, pp. 51-55, 2003.

[74] Z. Li, C. J. Capozzi, R. A. Gerhardt, and R. J. Samuels, "Characterization of the Optical Properties of PMMA/NANO-ITO Composites," Atlanta, GA: 2003 Southern Regional Meeting of the American Chemical Society.

[75] T. Liu and R. Samuels, "The influence of hydrogen chloride doping level on the complex refractive indices of anisotropic polyaniline film: Application of a new internal reflection waveguide coupling technique," *Journal of Polymer Science Part B-Polymer Physics,* vol. 39, pp. 2481-2490, 2001.

[76] T. Liu, C. L. Henderson, and R. Samuels, "Quantitative characterization of the optical properties of absorbing polymer films: Comparative investigation of the internal reflection intensity analysis method," *Journal of Polymer Science Part B-Polymer Physics,* vol. 41, pp. 842-855, 2003.

[77] Z. Li, M.S. Thesis, "Three-dimensional optical characterization of heterogeneous polymer systems," Atlanta, GA: Georgia Institute of Technology, 2004.

[78] http://usaxs.xor.aps.anl.gov/staff/ilavsky/indra_2.html, accessed 3/2009.

[79] http://usaxs.xor.aps.anl.gov/staff/ilavsky/irena.html, accessed 3/2009.

[80] R. A. Gerhardt, "Impedance Spectroscopy and Mobility Spectra," in *Encyclopedia of Condensed Matter Physics*: Elsevier Press, 2005, pp. 350-363.

[81] Y. F. Li, B. Zhang, and X. B. Pan, "Preparation and characterization of PMMA-kaolinite intercalation composites," *Composites Science and Technology,* vol. 68, pp. 1954-1961, 2008.

[82] B. D. Cullity, *Elements of X-ray Diffraction*. Reading: Addison-Wesley, 1978.

[83] V. Krishnamurthy and I. L. Kamel, "Cold Compaction and Sintering of Ultrahigh-Molecular-Weight Polyethylene Containing a Segregated Iron Network," *Polymer Engineering and Science,* vol. 29, pp. 564-572, 1989.

[84] H. F. Fischmeister and E. Arzt, "Densification of Powders by Particle Deformation," *Powder Metallurgy,* vol. 26, pp. 82-88, 1983.

[85] M. L. Steigerwald, A. P. Alivisatos, J. M. Gibson, T. D. Harris, R. Kortan, A. J. Muller, A. M. Thayer, T. M. Duncan, D. C. Douglass, and L. E. Brus, "Surface Derivatization and Isolation of Semiconductor Cluster Molecules," *Journal of the American Chemical Society,* vol. 110, pp. 3046-3050, 1988.

[86] B. Abramoff and J. Covino, "Transmittance and Mechanical-Properties of PMMA-Fumed Silica Composites," *Journal of Applied Polymer Science,* vol. 46, pp. 1785-1791, 1992.

[87] D. Sun, N. Miyatake, and H. J. Sue, "Transparent PMMA/ZnO nanocomposite films based on colloidal ZnO quantum dots," *Nanotechnology,* vol. 18, 2007.

[88] J. E. Song, Y. H. Kim, and Y. S. Kang, "Preparation of indium tin oxide nanoparticles and their application to near IR-reflective film," 2006, pp. 791-795.

[89] J. P. Clerc, G. Giraud, J. M. Laugier, and J. M. Luck, "The Ac Electrical-Conductivity of Binary Disordered-Systems, Percolation Clusters, Fractals and Related Models," *Advances in Physics,* vol. 39, pp. 191-308, 1990.

[90] D. Stauffer and A. Aharony, *Introduction to Percolation Theory,* 2nd ed. Philadelphia: Taylor and Francis, Inc., 1991.

[91] R. M. German, *Powder Metallurgy Science*. Princeton: Metal Powder Industries Federation, 1984.

[92] K. D. Murphy, G. W. Hunt, and D. P. Almond, "Evidence of emergent scaling in mechanical systems," *Philosophical Magazine,* pp. 3325-3338, 2006.

[93] M. Creyssels, E. Falcon, and B. Castaing, "Scaling of ac electrical conductivity of powders under compression," *Physical Review B,* vol. 77, 2008.

[94] M. T. Connor, S. Roy, T. A. Ezquerra, and F. J. B. Calleja, "Broadband ac conductivity of conductor-polymer composites," *Physical Review B,* vol. 57, pp. 2286-2294, 1998.

[95] C. R. Bowen and D. P. Almond, "Modelling the 'universal' dielectric response in heterogeneous materials using microstructural electrical networks," *Materials Science and Technology,* vol. 22, pp. 719-724, 2006.

[96] D. S. Mebane and R. A. Gerhardt, "Interpreting impedance response of silicon carbide whisker/alumina composites through microstructural simulation," *Journal of the American Ceramic Society,* vol. 89, pp. 538-543, 2006.

[97] I. Balberg, D. Azulay, D. Toker, and O. Millo, "Percolation and tunneling in composite materials," *International Journal of Modern Physics B,* vol. 18, pp. 2091-2121, 2004.

[98] E. Hecht, *Optics,* 3rd ed. Reading: Addison-Wesley, 1998.

[99] F. Lux, "Models Proposed to Explain the Electrical-Conductivity of Mixtures Made of Conductive and Insulating Materials," *Journal of Materials Science,* vol. 28, pp. 285-301, 1993.

[100] S. Kirkpatrick, "Percolation and Conduction," *Reviews of Modern Physics,* vol. 45, pp. 574-588, 1973.

[101] H. Scher and R. Zallen, "Critical Density in Percolation Processes," *Journal of Chemical Physics,* vol. 53, pp. 3759-&, 1970.

[102] K. Miyasaka, K. Watanabe, E. Jojima, H. Aida, M. Sumita, and K. Ishikawa, "Electrical-Conductivity of Carbon Polymer Composites as a Function of Carbon Content," *Journal of Materials Science,* vol. 17, pp. 1610-1616, 1982.

[103] M. Sumita, H. Abe, H. Kayaki, and K. Miyasaka, "Effect of Melt Viscosity and Surface-Tension of Polymers on the Percolation-Threshold of Conductive-Particle-Filled Polymeric Composites," *Journal of Macromolecular Science-Physics,* vol. B25, pp. 171-184, 1986.

[104] R. L. McCullough, "Generalized Combining Rules for Predicting Transport-Properties of Composite-Materials," *Composites Science and Technology,* vol. 22, pp. 3-21, 1985.

[105] G. Ondracek, "The Quantitative Microstructure-Field-Property Correlation of Multiphase Materials," *Metall,* vol. 36, pp. 523-531, 1982.

[106] M. Frary and C. A. Schuh, "Connectivity and percolation behaviour of grain boundary networks in three dimensions," *Philosophical Magazine,* vol. 85, pp. 1123-1143, 2005.

[107] G. Voronoi, "New parametric applications concerning the theory of quadratic forms - Second announcement," *Journal Fur Die Reine Und Angewandte Mathematik*, vol. 134, pp. 198-287, 1908.

[108] R. Williams, *The Geometrical Foundation of Natural Structure: A Source Book of Design*. New York: Dover, 1979.

[109] J. Ilavsky, "Form Factors & Structure Factors included in the Irene package " in *Igor Pro Help file*, 2008.

[110] A. M. Gokhale, "Unbiased Estimation of Curve Length in 3-D Using Vertical Slices," *Journal of Microscopy-Oxford*, vol. 159, pp. 133-141, 1990.

[111] C. S. Smith and L. Guttman, "Measurement of Internal Boundaries in 3-Dimensional Structures by Random Sectioning," *Transactions of the American Institute of Mining and Metallurgical Engineers*, vol. 197, pp. 81-87, 1953.

[112] N. G. Deshpande, Y. G. Gudage, A. Ghosh, J. C. Vyas, F. Singh, A. Tripathi, and R. Sharma, "Studies on high electronic energy deposition in transparent conducting indium tin oxide thin films," *Journal of Physics D-Applied Physics*, vol. 41, 2008.

[113] S. Maensiri, P. Laokul, J. Klinkaewnarong, S. Phokha, V. Promarak, and S. Seraphin, "Indium oxide (In_2O_3) nanoparticles using Aloe vera plant extract: Synthesis and optical properties," *Optoelectronics and Advanced Materials-Rapid Communications*, vol. 2, pp. 161-165, 2008.

[114] A. V. Mudryi, A. V. Ivaniukovich, and A. G. Ulyashin, "Deposition by magnetron sputtering and characterization of indium tin oxide thin films," *Thin Solid Films*, vol. 515, pp. 6489-6492, 2007.

[115] Y. B. Zhao, Z. J. Zhang, Z. S. Wu, and H. X. Dang, "Synthesis and characterization of single-crystalline In_2O_3 nanocrystals via solution dispersion," *Langmuir*, vol. 20, pp. 27-29, 2004.

VITA

The author was born on March 22, 1981 and grew up in Hackensack, New Jersey. His innovative attitude, close attention to detail, and curiosity lead him to continue his education in the field of engineering. In Fall 1999, he began his undergraduate studies at the School of Engineering at Rutgers, The State University New Jersey – New Brunswick/Piscataway Campus. In Spring 2001, he joined the small research group of Dr. Jun John Xu, who was interested in the synthesis and applications of amorphous transition-metal oxides for cathodes in rechargeable lithium batteries. During his time there, the author developed a strong interest for research and development, which peaked his motivation to pursue graduate studies. In Fall 2003 he graduated with a Bachelor of Science in Ceramic Engineering at Rutgers. In Fall 2004, he began his graduate studies in the Ph.D program at the School of Materials Science and Engineering at the Georgia Institute of Technology. He joined Dr. Rosario A. Gerhardt’s research group, where his doctoral research focused on non-destructive testing and property-microstructure correlations in polymer-matrix nanocomposites, and inorganic chemistry synthesis. The author graduated with his Ph.D in Materials Science and Engineering in May 2009.